Copyright is owned by the Author of the thesis. Permission is given for a copy to be downloaded by an individual for the purpose of research and private study only. The thesis may not be reproduced elsewhere without the permission of the Author.

Analyzing seismic signals to understand volcanic mass flow emplacement

A thesis in partial fulfillment of the requirements for the degree of

Doctor of Philosophy in Earth Sciences

At Massey University, Palmerston North, Manawatu, Aotearoa New Zealand





Braden Michael Larson Walsh

2017

Abstract

Natural hazards are one of the greatest threats to life, industry, and infrastructure. It has been estimated that around a half billion people worldwide are in direct proximity to the danger of volcanic hazards. For volcanic mass flows, such as pyroclastic density currents and lahars, extreme runout distances are common. The close proximity of large population centers to volcanoes requires the implementation of early warning and real-time monitoring systems. A large portion of the progress towards real-time monitoring is through the use of geophysical instrumentation and techniques. This research looks into emerging geophysical methods and tries to better constrain and apply them for volcanic purposes. Specifically, multiple types of amplitude source location techniques are described and used for locating and estimating the dynamics of volcanic mass flows and eruptions. Other methods, such as semblance and back projection, are also employed. Applying the active seismic source method to a lahar that occurred on October 13th 2012 at Te Maari, New Zealand, locations and estimations of lahar energy were calculated in an increased noise environment. Additionally, the first ever calibration of the amplitude source location (ASL) method was conducted using active seismic sources. The calibration proved to decrease true error distances by over 50%. More calibration on the ASL method was accomplished by using all three components of the broadband seismometer. Initial results showed that using all three components reduced extreme errors and increase the overall precision of the locations. Finally, multiple geophysical methods (ASL, semblance, back projection, waveform migration, acoustic-seismic ratios) were used to show

that a combination of instrumentation could produce more reliable results. This research has filled gaps in the preexisting knowledge for hazards. With these results, more effective hazard warnings can be produced, and systems for real time estimations of locations and dynamics of volcanic events could be developed.

Dedication

While writing this thesis I was pondering whom I should dedicate this brilliant piece of work to. I dedicated my poorly wrote with lots of spelling errors Masters thesis to my family, and in some ways that is very fitting. Families are like that, they are not perfect, there is always someone messed up or something wrong going on, but in the end you hold them dearly and could not live with out them. I am not strictly applying this metaphor solely on my maters thesis, but rather to education in general. I believe education is the most valuable thing someone can have and even if it is not appealing they should not waste one moment of it. Trying to improve the future or society in anyway should be the ultimate goal for every person, because what better way is there to live life than trying to advance our species. In saying this, should I dedicate my thesis to the future? That seems really cheesy, so no, and if I really think about it, did I change society in any way or advance science in any way by completing this? No, not really, so did I just waste three years of my life? Well it depends on the person you ask. Should I then dedicate this to myself, because after all I am awesome? Maybe not, because that might be too much of an awesome move and put me into a legendary status. So then who or what gets the credit for my motivation for these last three years? At the end of the day when everything is said, all wrote up, and done, all I can do is dedicate this thesis to YOU, you the poor soul who reads this, you the poor soul who gets this thesis dropped in your lap and is forced to read this, you the poor soul who after forced reading this thinks my work is crap and thinks you can do better than me (and to you, I bet you can and please try your best), and finally to

you the sorry soul who if force to read this and gets any kind of useful information out of it to make your PhD, Masters, or educational path just that little bit easier, I dedicate this thesis.

Acknowledgements

First off I would like to thank and acknowledge the hard working people at GeoNet for installing and taking care of all the seismometers around New Zealand. If it were not for you all, I would have not had anywhere to steal my earthquake/volcanic data from. This also relates to the great job done by the people at the Earthquake Commission (EQC) and the Department of Conservation (DoC). Closely related to this would be my advisor from GNS, Dr. Jolly, which I would like to thank for all your contributions (i.e. projects, data, skills) especially all the things you have taught me, and all the things I have learned from you. The best thing you ever did for me was not giving me anything, you made me learn on my own and write all my programs, meanwhile most of the time correcting me and holding back telling me how not smart I was. Dr. Jolly I will always remember our lunches in that we always ended up talking about US sports, which gave me a feeling of home. Dr. Procter what can I say, you are my homeboy, the supreme pro, super-duper, big cheese, papa smurf, grey fox advisor. I would like to thank you for all your helpful nudges and humor that was meant to make me work harder. Also all the times we had together in the field or on trips in which we had great conversations and discussions. Oh and how could I forget all those awesomely amazing maps and points that took you all day to make, they were excellent, I guess. Last but not least, I would like to acknowledge my dearest friends and flatemates. How could I have ever survived without you? Actually, probably would be healthier, but defiantly lonelier. You all know who you are, and I thank you for the memories and the encouragement over my time in good ol' Palmy.

Table of Contents

Abstract……i
Dedication……iii
Acknowledgments……v
Table of Contents……vi
List of Figures……ix
List of Tables……xvi
Chapter 1 Introduction……1
1.1 The Problem……2
1.2 Research Questions……3
1.3 Thesis Outline and Structure……5
1.4 Literature Review……7
1.4.1 Lahars and their triggering mechanisms……7
1.4.2 Seismic monitoring and classifications of mass flow behavior……9
1.4.2.1 Debris flows……13
1.4.2.2 Hyperconcentrated flows……21
1.4.2.3 Snow avalanches……27
1.4.2.4 Granular flows……32
1.4.3 Geophysical techniques for determining dynamics and locations of seismic phenomena……39
1.4.3.1 Phase arrival time……39
1.4.3.2 Coherence……40
1.4.3.2.1 Semblance……40
1.4.3.2.2 Back projection……42
1.4.3.3 Amplitude source location……43
1.4.3.3.1 Amplification factors……45
1.4.3.4 Active source matching……46

Chapter 2 Seismic analysis of the 13 October 2012 Te Maari, New Zealand, lake breakout lahar: Insights into flow dynamics and the implications on mass flow monitoring……49
2.1 Introduction……51
2.2 Data……56
2.2.1 Volcanic mass flow background……56
2.2.2 Active source data……59
2.2.3 Natural data……60
2.3 Methods……65
2.3.1 Processing of natural and active source data……65
2.3.2 Correlation between natural data and active source data……66
2.3.3 Estimating energy of natural data from active source data……67
2.3.4 Noise characterization……68
2.4 Results……71
2.5 Discussion……80
2.6 Conclusions……85

Chapter 3 Calibrating the amplitude source location (ASL) method by using active seismic sources: An example from Te Maari Volcano, Tongariro National Park, New Zealand.....88
3.1 Introduction.....90
3.2 Data.....94
3.2.1 Methods.....96
3.2.2 Amplification factors.....97
3.2.3 Grid search.....98
3.3 Results.....99
3.4 Discussion.....104
3.5 Conclusions.....107

Chapter 4 Geophysical examination of the 27 April 2016 Whakaari/White Island, New Zealand eruption and its implications for vent physiognomies and eruptive dynamics.....109
4.1 Introduction.....111
4.2 Data.....117
4.2.1 Eruption history and background.....117
4.3 Locating eruption sources using the amplitude source location method.....118
4.4 Insights into eruption dynamics using infrasound.....128
4.4.1 Source migration analysis.....129
4.5 Analyzing the very long-period earthquake.....135
4.6 Determining eruption pulse characteristics using the volcanic acoustic-seismic ratio.....139
4.7 Discussions.....144
4.8 Conclusions.....148

Chapter 5 Improving seismic source locations through the amplitude source location (ASL) method using 3-compont analysis? An example from Te Maari Volcano, Tongariro National Park, New Zealand.....151
5.1 Introduction.....152
5.2 Data.....154
5.3 Methods.....157
5.3.1 Amplification factors.....158
5.3.2 Grid search.....161
5.4 Results.....161
5.5 Component analysis.....168
5.6 Discussions.....173
5.6.1 Estimating locations for 3-componetn ASL using H/V ratios to correct site response.....176
5.7 Conclusions.....183

Chapter 6 Synthesis and conclusions.....185
6.1 Synthesis.....186
6.2 Specific findings.....198
6.2.1 Using active sources to determine dynamics and locations....198
6.2.2 Using active sources to calibrate the ASL method.....199
6.2.3 Using multiple location techniques to understand volcanic eruptions.....199
6.3 Conclusions.....201
6.3.1 Evaluating the research objectives.....201
6.4 Future recommandations.....203

Appendix A.....207
A.1 Back projection.....208

Appendix B.....211
B.1 Chapter 2 supplementary material.....212
B.1.1 Programs.....212
B.2 Chapter 3 supplementary material.....213
B.2.1 Programs.....213
B.3 Chapter 4 supplementary material.....214
B.3.1 Programs.....214
B.4 Chapter 5 supplementary material.....215
B.4.1 Programs.....215
B.5 Additional programs.....215

Appendix C.....216
Bibliography.....218
Vita auctoris.....239

List of figures

Figure 1.1: E-W component seismogram of a debris avalanche at La Sionne Switzerland, B) spectrogram, C) total spectrum (Surinach et al., 2005)……..……12

Figure 1.2 Seismic signals from three different debris flows in the Moscardo Torrent, Italy (Arattano, 1999)……..15

Figure 1.3 Vertical seismic signal recording debris flow at Ai-Yu-Zi Creek, Nan-Tou, Taiwan (Huang et al., 2007)……16

Figure 1.4 Seismogram of a debris flow in the Himalayan Mountains, Nepal (Burtin et al., 2009)……17

Figure 1.5 Vertical continuous seismogram of a debris flow on Izu-Oshima Island, Japan, 16 October 2013, letters represent debris flow events (Ogiso and Yomogida, 2015)……..18

Figure 1.6 Seismic signal (a), spectrogram (b) and running average spectra (c) of the snow-slurry hyperconcentrated flow on Ruapehu, NZ, September, 2007 (Cole et al., 2009)……..23

Figure 1.7 Seismic signal (a), spectrogram (b) and RSEM (c) of the 15 September 2012 lahar on Colima, Mexico (Vazquez et al., 2013)……..24

Figure 1.8 Seismogram (a) and spectrogram (b) of a lahar flowing down Cotopaxi, Ecuador (Kumagai et al., 2009)……..25

Figure 1.9 Seismic waveforms for four Iliamna, Alaska avalanches (Caplan-Auerbach et al., 2005)……..29

Figure 1.10 Three-component seismogram of the 1997 Pointe des Tsarmettes avalanche, Spain (Surinach et al., 2000)……..30

Figure 1.11 Seismic recording of an avalanche on Bridger Range, Montana, USA (Lawrence and Williams, 1976)……31

Figure 1.12 All three components of a rockfall that occurred in 2007 at Montserrat, Catalonia (Vilajosana et al., 2008)……..33

Figure 1.13 Vertical seismograms (top) with spectrograms (bottom) from multiple rockfall events that occurred in the French Alps. The first solid line shows time of P-wave during rupture, while the second indicates the theoretical impact time after the fall (Deparis et al., 2008)……..34

Figure 1.14 Seismic signals of pyroclastic flows produced by the partial collapse of the lava dome on Colima, Mexico (Zobin et al., 2009)……36

Figure 1.15 Seismogram (a) and spectrogram (b) of a pyroclastic flow on Soufriere Hills Volcano, Montserrat (Levy et al., 2015)……37

Figure 1.16 Seismogram (A) and spectrogram (B) of the August 1999 Soufriere Hills Volcano, Montserrat (Jolly et al., 2002)……38

Figure 2.1: Hillshade DEM map of the Tongariro massif. Insert shows location of the map area of the North Island of New Zealand. (Note, seismic station TON2 was destroyed by the 6 August 2012 eruption and was not used). The Upper Mangatipua Stream is the location of the volcanic mass flow channel……54

Figure 2.2: A) Map of the volcanic mass flow channel and Mangatipua stream with the runout extent of the 6 August debris flow (red) and the 13 October lahar (yellow). The debris flow scarp, chasm, and the eruption vent are shown in orange. B) Map of the locations of the active source drops along with the 13 October lahar source (yellow), and the ephemeral lake (blue) created by the debris flow dam. Note subsequent figures will utilize the same shapes and colors as the active source drops shown in figure 2B……58

Figure 2.3: A) Graph showing the ephemeral lake level (left y-axis) and hourly rainfall (green circles) in millimeters (right y-axis). The lake level (blue line) steadily increases until the point of the dam breach at 11:20 UTC on 13 October (red star). B) Unfiltered seismogram of lahar from station KRVZ Z-component starting 10 minutes prior and 20 minutes after the lahar onset indicated in 3A by the red double arrow……62

Figure 2.4: Pictures of the A) Mass flow channel looking up towards the Te Maari vent, B) The debris flow dam and breach, C) Lahar flow, D) Lahar deposits, and E) Stratigraphy of lahar deposits……63

Figure 2.5: Amplitude spectra for 8 active source drops and 14 station components used in this analysis. The spectra include a frequency range between 0-12 Hz. Note TON7 has no East component due to corrupt data……64

Figure 2.6: Amplitude spectra for the natural data recorded on 14 station components used for this analysis. The spectra include a frequency range between 0-12 Hz. Each spectrogram contains the spectra of the lahar (blue) and an overlay of noise 10 minutes before the lahar (red). Note TON7 has no East component due to corrupt data……69

Figure 2.7: Amplitude spectra for the natural data for the maximum correlated time window on 14 station components. The spectra include a frequency range between 0-12 Hz. Each spectrogram consists of the spectra of one time window of the lahar (blue) and an overlay of the averaged 10 minutes pre-lahar (red)……70

Figure 2.8: Signal-to-noise charts depicting different SNR thresholds at a frequency band of 3-10 Hz for the 9 station components used for the final results for this study, A) 1.5, B) 2.0, C) 2.5, D) 3.0, E) 3.5, F) 4.0. The SNR threshold for time windows below the SNR limit (blue) or above the SNR limit (green)……74

Figure 2.9: Correlation processing and energy release through time for the 13 October 2012 lahar using multiple frequency ranges. Each point correlates to a 10.24 s non-overlapping time window. The points are color coded to match drop locations and grey dots are data that fell below the SNR limit. Further analysis was limited to the 3-10 Hz frequency range (C)……75

Figure 2.10: Correlation processing for the 13 October 2012 lahar and pre-lahar period. The lahar data were compared to each of the 8 active source drop positions by computing the cross-correlation for a uniform set of 3 stations (9 components) and selecting the best seismic amplitude distribution in a non-overlapping moving time window of 10.24 s each for analysis. Panel A shows the energy release through time with each time window color-coded to the drop location where colors are shown in the legend. Grey dots are "ghost points" or data that fell below the 2.0 SNR limit. Panel B shows the correlation coefficient for the best drop location to the lahar data. Panel C shows the lahar seismogram from the station KRVZ Z-component……76

Figure 2.11: Graphs showing three specific time windows (11:31- red, 11:46- magenta, 11:51-green UTC) at various positions in the lahar's progress. Values correspond to the correlation of each time window with each drop location (A) maximum value, B) minimum value) after 500 iterations of Jackknife error analysis. Color on lines correspond to best correlated drop location……79

Figure 2.12: Final energy estimates for the 13 October 2012 Te Maari lahar in the 3-10 Hz band displaying two signal to noise results. A) Results with a SNR limit of 2.0, B) results with a SNR limit of 1.5. The use of 10.24s time windows is used along with each time window is color coded to the drop location of best correlation, colors of drops are shown in the legend. Grey dots are time windows that fall below the listed SNR limit……83

Figure 3.1: Earthquake locations used in the coda wave normalization method to calculate amplification factors (AFs). The red square in the center is the ASL grid area. Active seismic sources are yellow circles and seismic stations are green triangles……..93

Figure 3.2: Example waveforms for the active source event 1 (A) and event 7 (B) for each of the seismic stations used in the ASL analysis, shown by distance away from source……95

Figure 3.3: A) Location of active source events used in this study (yellow circles) and surface wave ASL locations with corrections for AFs (green) and without (red). B-C) location results for events 1 and 7 with variable attenuation and velocity. Stars represent the base value of an attenuation of Q=60 and a surface wave velocity of β=1500 m/s, while the attenuation is represented as squares and velocity as circles……100

Figure 3.4: Analysis of the location effects for A) the body wave (orange) and surface wave (green) geometrical spreading. Sensitivity tests (B) relating to non-uniform station sets for event 1 (blue circles) and event 7 (purple circles) and the distribution of standard errors associated with AFs for Event 1 (cyan diamonds) and Event 7 (orange diamonds). Stars represent locations based on the mean AFs. (C) ASL results for AFs computed from the aggregate active source data (purple) compared to standard AF locations (green)……106

Figure 4.1: Map of Whakaari Island, New Zealand depicting the locations of seismometers (green triangles), acoustic sensors (magenta triangles), and active source drops (yellow crosses)……114

Figure 4.2: Seismic waveforms from station WIZ of the April 27th 2016 Whakaari eruption. Subfigures represent each of the eruptive pulses during the event……115

Figure 4.3: Acoustic waveform data from station WIZ (A) and WSRZ (B) of the April 27th 2016 Whakaari eruption. Subfigures represent each of the eruptive pulses during the event……116

Figure 4.4: Seismic spectrogram for the eruption event (station WIZ) along with amplitude spectra for each of the seismic stations. The eruption spectra (black) are overlain by pre-event noise (blue) for background noise comparison……..119

Figure 4.5: Minimal residual amplitude source location results (stars) using the base input values of β=1300 m/s and an attenuation value of Q=10……120

Figure 4.6: Amplitude source location results for each of the eruptive pulses with variable attenuation and velocity. The stars represent the base values of an attenuation of Q=10 and a body wave velocity of β=1300 m/s, while the attenuation is represented as squares and the velocity as circles……126

Figure 4.7: Calibrated amplitude source location results for each eruption pulse. Input values of an attenuation of Q=3 and a body wave velocity of β=1300 m/s were used to determine the locations of non-corrected results (pink stars) and active source corrected locations (green stars)……127

Figure 4.8: Acoustic signals for each eruptive pulse. Both WIZ (blue) and WSRZ (red) sensors are stacked and overlain at the same timing……131

Figure 4.9: Source migration analysis figures (A) no filter, (B) 0.1-0.2 Hz, and (C) 0.2-2.0 Hz for the acoustic signals of both stations WIZ (blue) and WSRZ (red) for each eruptive pulse. Each subfigure contains the acoustigram, phase lag, peak frequency, and correlation coefficient values between the two stations……132

Figure 4.10: Map of particle motions based on waveform semblance for the VLP event during the eruption sequence, a blue star represents the best-fit location..138

Figure 4.11: Energy partitioning between stations WIZ and WSRZ for acoustic data (A) and seismic data (B). The colors of the points represent the different eruptive pulses……141

Figure 4.12: VASRs between stations WIZ and WSRZ for all six eruptive pulses for acoustic data (A) and seismic data (B)……142

Figure 4.13: Eruption waveforms for all recording stations for both seismic (black) and acoustic (blue) data depicting the VLP event and the fourth eruptive pulse. Notice the differences in onsets (~50 s) of the VLP on the seismic waveform compared to the eruption onset on the acoustic waveform……145

Figure 4.14: Post eruption imagery from Whakaari crater area. Green stars represent ASL locations for the six pulses, yellow star represents location of the VLP, and the purple circle represents the theorized April 27th eruption vent area……149

Figure 5.1: Location of study area, northern section of the Tongariro National Park, New Zealand. Yellow circles represent the active source event locations along the Te Maari debris flow channel……155

Figure 5.2: Seismic spectra for all of the active source drops for each station component……160

Figure 5.3: ASL minimal residual location results for the vertical component (blue), 3-component amplification factor method 1 (teal), and 3-componet method 2 (magenta)……162

Figure 5.4: ASL minimal residual location results for the vertical component (blue), 3-component amplification factor method 1 (teal), East component (pink), and North component (green)……164

Figure 5.5: Analysis of the location effects for amplification factors of standard errors for comparing the vertical component and 3-component distribution for event 1 (A) and event 7 (B)……165

Figure 5.6: Analysis of the location effects for station distribution effects for comparing the vertical component and 3-component for event 1 (A) and event 7 (B)……169

Figure 5.7: Analysis of the location effects for amplification factors for the distribution of standard errors for comparing each of the seismic components for event 1 (A) and event 7 (B)……170

Figure 5.8: Analysis of the location effects for station distribution effects for comparing each of the seismic components for event 1 (A) and event 7 (B)……172

Figure 5.9: ASL minimal residual location results for the CWN vertical component (blue), and 3-component (teal), as well as, the H/V 3-componet (red) and vertical component (purple) results……178

Figure 5.10: Analysis of the location effects for amplification factors of standard errors for comparing the CWN and H/V method 3-component distribution for event 1 (A) and event 7 (B)……182

Figure 6.1: ASL and AS results for the August 6th 2012 Te Maari, New Zealand eruption sequence. A) ASL results for surface waves, B) ASL results for body waves, C) Active source results. Color of dots represent the estimated nearest active source location (for drop locations refer to figure 4.1)……188

Figure 6.2: ASL depth location results for the August 6th 2012 Te Maari, New Zealand eruption sequence. A) ASL surface wave results, B) ASL body wave results. Dot colors represent the nearest AS drop from the estimated ASL results (for drop locations refer to figure 2.2)……190

Figure 6.3: ASL and AS results for the October 13th 2012 Te Maari, New Zealand lake breakout lahar. A) ASL results with no site and path effect corrections, B) Calibrated ASL results, C) Active source proxy results. Color of dots represent the estimated nearest active source location
(for drop locations refer to figure 2.2)……194

Figure 6.4: Map showing ASL results for the October 13th 2012 Te Maari, New Zealand lake breakout lahar. Red stars represent ASL locations with no site and path effect corrections and blue stars represent AS calibrated ASL locations. Color is coded to time, which represents early (lighter) to later in the lahar (darker). Each star represents a 10 sec non-overlapping time window……195

Figure 6.5: ASL and AS results for the April 27th 2016 White Island, New Zealand eruption sequence. A) Active source results, B) Calibrated ASL results. Color of dots represent the estimated nearest active source location
(for drop locations refer to figure 4.1)……197

Figure A.1: Back projection results for the six eruptive pulses during the April 27th 2016 eruption on White Island. Color grid represents level of coherence where blue is low and red is highly coherent between the stations. Green stars represent location of largest coherence……210

List of tables

Table 3.1: Amplification Factors……..99

Table 4.1: Station corrections determined from active sources for 13 broadband seismometers that were installed during the active source experiment……..125

Table 4.2: Summary of semblance location for VLP event 2016-04-27 09:53:30 UTC filtered between 0.02 to 0.125 Hz. The location is in meters based on New Zealand Map Grid coordinates in meters. The lateral and depth (er_l (z)) error estimates are in meters based on 2% error limit from the maximum semblance……..137

Table 5.1: Amplification Factors……159

Table 5.2: Root mean squared errors……167

Table 5.3: H/V site corrections……177

Table 5.4: Summary of results……181

CHAPTER 1: INTRODUCTION

Chapter Contents

Chapter 1: Introduction……1
1.1 The problem……2
1.2 Research questions……3
1.3 Thesis outline and structure……5
1.4 Literature review……7
1.4.1 Lahars and their triggering mechanisms……7
1.4.2 Seismic monitoring and classifications of mass flow behavior……9
1.4.2.1 Debris flows……13
1.4.2.2 Hyperconcentrated flows……21
1.4.2.3 Snow avalanches……27
1.4.2.4 Granular flows……32
1.4.3 Geophysical techniques for determining dynamics and locations of seismic phenomena……39
1.4.3.1 Phase arrival time……39
1.4.3.2 Coherence……40
1.4.3.2.1 Semblance……40
1.4.3.2.2 Back projection……42
1.4.3.3 Amplitude source location……43
1.4.3.3.1 Amplification factors……45
1.4.3.4 Active source matching……46

CHAPTER 1: INTRODUCTION

1.1 The problem

There are many risks associated with volcanic environments. People, industry, and agriculture are all affected by the hazards of not only volcanic eruptions, but also to volcanic processes such as debris flows, debris avalanches, pyroclastic density currents, and lahars. Volcanic flows or mass flows can destroy and damage many different things, such as structures, including entire cities, and lives. In fact over a half a billion people worldwide are currently living under the direct threat of deadly volcanic mass flows and historically people have wrongly felt safe even at great distances due to the lack of efficient warning systems (Cashman and Sparks, 2013). Being able to predict initiation and locate volcanic mass flows could be significant in helping to save lives. Research conducted in this area of volcanology requires the collection of geophysical as well as seismological data in real-time from mass flow events (e.g. Coviello et al., 2017). These data enable analysis of the dynamics of mass flows and information about their location, informing monitoring strategies.

Another reason for using seismological techniques is due to the danger that comes with researching volcanic mass flows. Physical hands-on methods such as bedload traps, dip buckets, etc. all put the operator near or in a potentially dangerous flow path. Seismometers on the other hand can be placed at a distance away from mass flow channels and still record data day or night and in any

weather conditions. The installation distance provides safety to researchers and also prevents the very expensive equipment from being destroyed by the flows.

This thesis aims to investigate different seismological and geophysical techniques to further understand volcanic processes on multiple volcanoes, and add to the existing knowledge on warning and risk management for not only volcanic mass flows but volcanic eruptions in general.

Two emerging seismological techniques have recently been used in volcanology for determining location and dynamics of volcanic events. The active seismic source method, made popular by Jolly et al. (2012) where large bags of sand were dropped from a helicopter onto White Island, and Te Maari (Jolly et al., 2014C), New Zealand to create active sources for comparison with natural volcanic events. The second method is the amplitude source location (ASL) method, which was first used in volcanic studies by Yamasato (1997) to locate pyroclastic flows on Unzen Volcano, Japan. Both of these methods, along with other seismological techniques (i.e. phase arrival, coherence, etc.), will be further examined and extended in this thesis for the determination of the dynamics and locations of volcanic processes and phenomena.

1.2 Research questions

The research questions in this thesis focus on the determination of the location and dynamics of multiple volcanic events and how to improve the methods by minimizing the error in the calculation of the results.

I. *Can active seismic sources be used to not only determine the dynamics of a lahar, but also give an estimation on flow location?* Using active seismic sources in determination of properties for mass flows is a relatively new idea. Being able to cross correlate active seismic sources with natural data has been shown to work on debris avalanches (Jolly et al., 2014C), but has not been demonstrated in high unwanted noise situations, such as a lahar.

II. *Can active seismic sources be used to calibrate the amplitude source location method?* This question dives into what true distance errors are "acceptable" and whether using active seismic sources can improve ASL results to decrease the true error distance from source?

III. *What are the eruption characteristics of the April 2016 White Island, New Zealand eruption?* Using multiple geophysical methods, can an eruption history be constructed by determining the timing and location of eruption signals from eruption source onset to surface eruption vent?

IV. *Does using all three components of a broadband seismometer improve location determinations for the amplitude source location method?* Here, active seismic sources are located using both the vertical component and all

three components of seismic data. We then compare the results to determine if one statistically improves location results over the other.

1.3 Thesis outline and structure

This thesis is composed of six chapters, along with appendices containing extra information, including datasets and programs used for the determination of results. The thesis starts with the introduction, which has included so far, "The Problem" (Chapter 1.1) and the research questions (1.2). Next, in the introduction will be the literature review (1.4), which will include descriptions of different types of volcanic mass flows as well as summaries of multiple seismic methods for determining dynamics and locations. Chapters 2-4 are international peer-reviewed journal articles, or work that has been submitted to peer-reviewed journals for publication. Chapter 5 is a comprehensive extension of an element of Chapter 3, focusing on research question (IV). Finally, the synthesis (Chapter 6) includes discussions, future work (6.4), and the conclusions of this thesis (6.3).

Chapter 2 is based on research question (I) and contains a full-length published research article that deals with using active seismic sources for correlation with natural lahar data to determine the dynamics and location, with time, of the lahar. The main conclusions from Chapter 2 include that active sources can be effectively applied to determining the properties of lahars, highlighting that the method still works under extreme background noise infringement, and that the lahar flowed in multiple stages due to multiple breakaways of the debris flow dam and refilling of the ephemeral lake.

Chapter 3 contains the full-length published research article based on research question (II) looking deeper into the ASL method to examine what factors affect the results, and whether active sources can be used to calibrate the ASL method. Sensitivity results from Chapter 3 show that input parameters for attenuation and velocity have a moderate influence on location, and amplification factors, as well as station geometry have a strong influence on location results. Furthermore, active sources are shown to be able to calibrate ASL by decreasing the true error location estimate of an event.

Chapter 4 contains the full-length submitted research article based on research question (III), determining the eruption characteristics of the April 27th White Island, New Zealand eruption. The main conclusions from Chapter 4 include the observations of six eruptive pulses in both the acoustic and seismic data. The eruptive vent locations for the pulses were located through seismic analysis with ASL and through acoustic data by using a source migration analysis. Additionally, an eruption history was theorized by the location and timing between a very long-period event at depth and eruption onsets on the surface.

Chapter 5 contains extended research into the amplitude source location method and explores using all three components of a broadband seismometer to locate the active source events. Chapter 5 concludes by comparing and contrasting the differences between using just the vertical component and using all three components to determine if the accuracy of the source determination increases.

Chapter 6 is the last chapter in the thesis and contains the synthesis, and in-depth discussion on possible future work and studies, as well as current projects. Finally, Chapter 6 ends with the conclusion where the research questions are reviewed, and the main points are reexamined.

The Appendices are divided into three parts: Appendix A, B, and C. Appendix A is based on extended work from Chapter 4 and contains the theory and process of the back projection technique used with acoustic signals. The back projection method is used to determine the location of eruptive vents on White Island, New Zealand. Appendix B contains descriptions of all the codes that were used in this thesis to process data and obtain results. Furthermore, Appendix B contains information on where to find the raw data used for the thesis. Finally, Appendix C has the statements of contribution for the published journal articles that are contained within this thesis.

1.4 Literature review

1.4.1 Lahars and their trigger mechanisms

Lahar is an Indonesian term that describes a mass flow that contains blocks and sediment from volcanic material (Van Bemmelen, 1949). Smith (1986) states: "Lahar as a term offers nothing in a descriptive sense that the less ambiguous terms debris flow or hyperconcentrated flow does not already provide, other than the composition of the clasts, which does not affect the depositional process." Following from this, lahars can have depositional characteristics of either a debris

flow or a hyperconcentrated flow, but the term “lahar” is still used in the literature to describe the flowing process (e.g. Pierson, 2005).

In terms of a flow process, a lahar can be defined as a rapidly flowing mixture of poorly sorted rock, water, sediment, and mud flowing downhill from a volcanic region (Pierson, 1985; Calvari et al., 1998). The flows carry sediment in suspension and are non-Newtonian with a finite yield strength (Pierson, 1985). Most lahars start out as floods and, as they flow downhill, they pick up sediment eventually transforming into either a debris flow or hyperconcentrated flow (Pierson and Scott, 1985; Lavigne et al., 2000). A lahar can transform back and forth between a debris flow and hyperconcentrated flow at any time during the flows duration depending on the location and conditions of the area.

There are many different mechanisms of triggering a lahar; some are large scale like a volcanic collapse and some are small, as in small scale rainfall-triggered lahars. A lahar could be generated from breakouts of water from lakes, release of glacial reservoirs, heavy intense rainfall, melting of snow or ice during an eruption, hot gasses or debris avalanches melting snow or ice transforming into lahars, pyroclastic flows melting snow or ice, saturated debris ejected from an eruption, landslides that are water rich, and partial collapses of a volcano (Pierson, 1985; Lecointre et al., 2004).

One type of triggering mechanism to look at in more detail is rain-induced lahars, because of their occurrence and frequency impacting populated areas. Rain triggered lahars are the most common type of lahar and have been the most

studied (e.g. Tungol and Regalado (1996); Lavigne et al., 2000; Coveillo et al., 2017). There are two types of rain-triggered lahars, hot and cold. Hot lahars are generated when an eruption has occurred, and cold lahars form from remobilization of older deposited sediments, which make them more common (Lavigne et al., 2000). Rain distribution, intensity, duration, geomorphology of the channel, and the sedimentology of the channel all contribute to determine if a cold lahar will be triggered by rain (Lavigne et al., 2000). Both Lavigne et al. (2000) and Zobin et al., (2009) found that 20mm/hr of rain at Merapi and 20mm/hr of rain at Pinatubo, triggered lahars; Tungol and Regalado (1996) reported that 18-24 mm/hr of rain at Pinatubo, Umbal, and Rodolfo was sufficient to trigger lahars; and Capra et al. (2010) at Colima found that 20mm/hr in the rainy season and 70 mm/hr in the dry season was able to trigger lahars. The frequency of lahars from rain mostly depends on the amount of precipitation, and the amount of loose material on the volcanic slope. The problem with developing warning systems based on estimating rainfall amounts is the uniqueness of every event and location. Every volcano and channel has different characteristics and the cited rainfall amounts are not always the amount needed to trigger a lahar.

1.4.2 Seismic monitoring and classifications of mass flow behavior

Seismic monitoring of mass flows can and will vastly improve warning systems in highly active regions, along with advancing the knowledge and research of mass flows. Seismic methods are one of the best techniques for monitoring mass flows because they are reliable, easily installable, and are safe. Old monitoring

methods such as current meters, tripwires, etc. can be dangerous, expensive, and unreliable. Seismometers and other ground sensors, such as geophones, acoustic flow monitors (AMFs) (Hadley and LaHusen 1995), and accelerometers can be placed at safe distances away from the flow channel; they can be used in any weather, also in day or night as no visibility is needed and are relatively easy to use, install, and process the data. Furthermore, the data can be telemetered to allow for real-time monitoring. Using seismometers to collect data from mass flows can allow and provide a useful low cost solution to the monitoring of mass flows (Jolly et al., 2014C). However ground vibration instruments also have problems when detecting mass flows. The biggest issue with detecting mass flows using seismometers is that there are numerous events taking place along side the flow, creating unwanted noise (e.g. eruption, human, weather) that will hide or impede the flow signal from accurate detection and interpretation (Arattano and Marchi, 2005; Jolly et al., 2014C; Chapter 2). Assessing the level and amount of non-mass flow background noise is of great importance when trying to detect, process, and eventually warn populations about flows (Burtin et al., 2008).

Most flows can be characterized the same way through seismic interpretations, but, like flow characteristics, the seismic signal of each type of flow has its own unique signature. Detection of a mass flow and how far away the flow is detectable depend on the flow type, size of flow, and coupling with the ground (Cole et al., 2009). Most mass flows form a triangular shaped wave in the seismogram and spectrogram (Figure 1.1) when approaching a seismometer; this is due to the head of the flow approaching the seismometers and the distance

between the flow and seismometer decreasing (Surinach et al., 2005). Attenuation plays a large role in the spectral signature of the flow as well. The further away the flow is the more attenuated the signal will become, and as the flow moves closer to the seismometer, the energy given off by the flow will have less attenuational effects, especially in the higher frequencies (Aki, 1980).

Not all ground vibration sensors are treated the same. The 3-component seismometer is the best and most ideal instrument to use for mass flow detection. Three component seismometers can record ground vibrations in all three directions, which is very important in mass flow research. Furthermore, broadband sensors can record signals in a wide frequency range, whereas single component instruments like geophones can only record in a limited frequency band. Also, in some cases, not all three components have the same recorded amplitudes, for example, snow avalanches (Surinach et al., 2005), snow-slurry lahars (Cole et al., 2009), debris flows (Jolly et al., 2014C), and hyperconcentrated flows (Chapter 2). This is why recording mass flows with just geophones or 1-component sensors can be misleading. Most of the time 1-component sensors only record the vertical or "Z" component of ground vibration, but a mass flow's energy can be the strongest in one of the two other components and this occurrence may result in poor data or even worse a delay in the detection time, which creates a delay in the flow warning time (Surinach et al., 2000; Keys and Green, 2008).

Figure 1.1 A) E-W component seismogram of a debris avalanche at La Sionne Switzerland, B) spectrogram, C) total spectrum (Surinach et al., 2005).

1.4.2.1 Debris flows

Debris flows are hazardous and dangerous because they are poorly sorted water saturated flows that move at high velocities (Lowe, 1979; Smith, 1986) and conceptually can be considered as a large waveform with a steep front consisting of many different sized sediments from grains to large boulders, followed by superimposed smaller waves (Arattano, 1999). Before the main body or front of the debris flow starts there are precursory water rich flows (Arattano et al., 2012). The tails of debris flows consist of more fluid than the front or main body, but still carry pebble sized sediment and can be considered as a hyperconcentrated flow phase (Arattano and Marchi, 2005; Navratil et al., 2013).

Most debris flows have a similar shape and distinct look to them in a seismogram (Figure 1.2-1.5). Debris flows are characterized by a triangular shaped signature on seismograms, due to the passing of the main flow front and body (Arattano et al., 2012). The seismic signature can have a steep front followed by a gradual decrease in amplitude behind the head of the flow, forming the triangular shape (Arattano, 1999). The triangular shape of the debris flow seismic signal can change in appearance depending on the geological structure, types of rocks in the flow, rheology of the channel bed, and the geometry of the channel (Huang et al., 2007). For example, the ground vibration intensity is stronger for boulder-rich flows with a steep and narrow channel (Suwa et al., 2003). The seismic signals created by debris flows are caused by inter-flow collisions and flow-channel bed interactions. Most of the vibrations are created from the collisions of

the large boulders and rocks within the flow, mostly at the flow front (Suwa et al., 2000; Huang et al., 2007). Due to debris flows occurring on the surface of the Earth and the fact that most of the seismic energy produced by debris flows is from the interactions and collisions of the large clasts within the flows, most of the radiated seismic energy is released as surface waves, primary Rayleigh waves (Huang et al., 2007). Thus the Rayleigh wave is used when estimating the dynamics and properties of debris flows.

Debris flows are non-Newtonian flows that have been observed to have distinct pulses or waves in their flow behavior (Calvari et al., 1998; Kazakov and Minervin, 2000). The debris flow waves travel both downhill in series, or one after the other, and in superimposed small waves within the larger pulses (Davies, 1990; Arattano and Moia, 1999). The series of pulses or surges are described usually with deceasing amplitude over time. The superimposed waves travel at higher velocities than the flow surges and also the mean flow velocity of the entire debris flow (Arattano and Moia, 1999). The cause of the debris flow pulses is not well known, but there are a number of possible explanations for the multiple surges. Lavigne and Suwa (2004) proposed that these surges might be due to inherent flow instability, transient damming and rapid release of fluid and material, variations in rainfall intensities/amounts, and/or variable distributions of rainfall over the entire drainage basin at which the debris flow occurs.

Figure 3.2 Seismic signals from three different debris flows in the Moscardo Torrent, Italy (Arattano, 1999).

Figure 1.4 Vertical seismic signal recoring debris flow at Ai-Yu-Zi Creek, Nan-Tou, Taiwan (Huang et al., 2007).

Figure 1.5 Seismogram of a debris flow in the Himalayan Mountains, Nepal (Burtin et al., 2009).

Figure 1.6 Vertical continuous seismogram of a debris flow on Izu-Oshima Island, Japan, 16 October 2013, letters represent debris flow events (Ogiso and Yomogida, 2015).

Debris flow sediment concentrations and deposits are one of the best ways to define a debris flow. The flows need to have sediment concentrations between 50-70% vol (Pierson, 1985; Pierson, 2005) and reach velocities greater than 10 m/s (Iverson et al., 2010). Debris flows are also mostly clay poor, but even clay contents as low as 3% can vastly increase the strength of the debris flow (Smith, 1986). Debris flows dramatically alter the landscape, with large amounts of sediment being remobilized and deposited (Arattano, 1999; Capra et al., 2002). This is because in debris flows the sediment is carrying and transporting the liquid or water (Pierson, 1995). The deposits of debris flows contain multiple textures and materials, which are deposited randomly and in small to massive quantities (Smith, 1986). They lack stratification, show reverse to normal grading, and are typically matrix supported (Smith, 1986; Calvari et al., 1998).

Many properties of debris flows can be calculated by the seismic signals created from the ground vibrations. Some properties that can be calculated from the seismicity of debris flows include frequency, velocity, amplitude, attenuation, discharge and volume. One of the most important properties to calculate is the frequency range of the flow. Finding the typical frequency range of debris flows in a particular region or channel can have a large impact on warning systems and risk management. Knowing the frequency range of flows in a certain channel can be used by automated warning systems to detect if a signal is a potential flow or not. Larger boulders create lower frequencies than smaller boulders (Burtin et al., 2009). Non-flow properties affect the frequency range as well. The density of the channel geology can also determine and affect the frequency range.

The denser the ground is, the narrower the frequency range will be for the debris flow (Huang et al., 2007). Debris flows can have a wide range of frequencies from less than 1.0 Hz to sometimes greater than 100 Hz. For instance 2-22 Hz in the Himalayas (Burtin et al., 2009), 3-12 Hz on Tongariro, NZ (Jolly et al., 2014C), 2-10 Hz on Izu-Oshima, Japan (Ogiso and Yomogida, 2015), and 50-100 Hz at Nan-Toum, Taiwan (Huang et al., 2007).

Being able to record the frequency range of a debris flow allows there to be an estimation of the attenuation. The attenuation of the flow depends on the frequency, which in turn corresponds to the decay rate. High frequencies correspond to the seismic signal decaying faster (Huang et al., 2007). Recording the seismic amplitude of the debris flow is also helpful in estimating properties. For instance the amplitude of the seismic signal is proportional to the discharge of the debris flow (Suwa et al., 2000; Huang et al., 2007). The maximum seismic amplitude can also be used to estimate the mean frontal velocity. Furthermore, with the use of two or more sensors, a running velocity can be calculated from the seismic amplitude and the distance between stations, and thus a volume can be estimated if the cross-sectional area of the channel is known (Galgaro et al., 2005).

The velocity of a debris flow is very important for warning applications. With debris flows, many different types of velocities can be measured and calculated, but there are only two velocities that are present throughout the entirety of the debris flow. The two velocities are the average velocity of the entire debris flow, and the propagation velocity of the seismic waves created by the

debris flow (Arattano, 1999). The most common velocity measurement of a debris flow is the mean frontal velocity because measuring a velocity with time is very difficult (Arattano et al., 1999), but can be estimated when using multiple sensors next to the debris flow channel and knowing the distance between stations (Arattano and Marchi, 2005; Galgaro et al., 2005). The seismic wave velocity is calculated using simple seismological determinations and for practical purposes can be viewed as Rayleigh waves travelling through the geological medium from the debris flow to the station (Huang et al., 2007). Following calculations of velocities, other properties such as discharge, total discharge volume, acceleration, and energy of the debris flow can be estimated (Arattano et al 1999; Suwa et al., 2000; Galgaro et al., 2005).

1.4.2.2 Hyperconcentrated flows

Hyperconcentrated flows deposits are distinguished from debris flow deposits due to their depositional cross-bedded nature, and on a flow since are considered on a water to sediment ratio spectrum to be between debris flows and normal fluvial flows (Smith, 1986). Hyperconcentrated flows are non-Newtonian flows that are not fully turbulent, but sediment particles have greater freedom of motion due to the large quantities of liquid (Pierson, 1985; Calvari et al., 1998). A hyperconcentrated flow is defined as having a very high sediment concentration between 20-60% by volume and 40-80% by weight with a wide range of grain sizes (Smith, 1986; Calvari et al., 1998). Also the flow needs to have at least a minimum yield strength of 60 Pa (Pierson, 2005).

A debris flow transforms into a hyperconcentrated flow when large amounts of fine-grained sediment are added bulking the flow. This usually occurs in areas where there is an abundance of fine sediment, steep slopes and deep flow channels, for example on volcanoes (Pierson, 2005). The sediment in hyperconcentrated flows can be any size, but are separated into two different categories (Smith, 1986). Fine particles are all the fine grained particles or sand sized grains that are being transported and rarely contact the bed (Pierson, 2005). The coarse particles are everything else in the flow, ranging in size from small cobbles to large boulders that can be deposited instantly or be carried with the flow for many kilometers (Cronin et al., 1999; Pierson, 2005).

The depositional characteristics of hyperconcentrated flows are similar to deposits that are rapidly deposited from suspension and contain a great amount of sediment. Deposits are poorly sorted, but clast supported and often contain normal grading with minor bedding in the finer material (Smith, 1986; Calvari et al., 1998). When a hyperconcentrated flow flows downhill, they either erode older flow deposits or create new deposits when the flow has reached a steady state. In this steady state, the flows go through constant deposition and erosion (Procter et al., 2010; Vazquez et al., 2013). Erosion most likely occurs in times of peak flow, and deposition occurs in areas where the flow might slow down due to slope decreases, bends, or an increase of channel width (Procter et al., 2010). This constant erosion and deposition creates new deposits that conceal or destroy older deposits (Vazquez et al., 2013).

Figure 1.7 Seismic signal (a), spectrogram (b) and running average spectra (c) of the snow-slurry hyperconcentrated flow on Ruapehu, NZ, September, 2007 (Cole et al., 2009).

Figure 1.8 Seismic signal (a), spectrogram (b) and RSEM (c) of the 15 September 2012 lahar on Colima, Mexico (Vazquez et al., 2013).

Figure 1.9 Seismogram (a) and spectrogram (b) of a lahar flowing down Cotopaxi, Ecuador (Kumagai et al., 2009).

Like debris flows, hyperconcentrated flows also flow downslope in waves or pulses. Many have noted this characteristic of hyperconcentrated flows: Pierson and Scott (1985) at Mount St. Helens, Hodgson and Manville (1999) at Ruapehu and Walsh et al, (2016) at Tongariro. This pulse-like behavior may be due to how the flow was initiated or the amount of water introduced from rain or other sources (see Chapter 2.2.3). Bow waves can also form in front of a lahar if the channel is narrow enough and the body of the lahar is generated very quickly (Lube et al., 2012). These high velocities usually come from flows that have higher water concentration, because the fastest portions of the flow are the areas with the most water content (Doyle et al., 2010).

Hyperconcentrated flows, like debris flows, show a triangular shaped seismic trace (Figure 1.6-1.8). Again this is attributed to the passing of the flow front by the sensor (Cole et al., 2009) and by the attenuational effects of the geological medium on the flow signal. However, not all hyperconcentrated flows are similar and each event usually has a uniquely different seismic signature. Changes in the properties of the flow such as the amount of liquid, ice or snow, and the amount and size of the grains and clasts produce different frequency responses (Doyle et al., 2010). High sediment hyperconcentrated flows produce lower frequencies, whereas snow slurry flows have the lowest frequency range because they have fewer interflow collisions due to the amount of snow (Lavigne et al., 2000; Cole et al., 2009; Doyle et al., 2010). Like debris flows, hyperconcentrated flows have a wide range of frequencies that can be anywhere between 1-100 Hz. For example frequencies ranging between 3-10 Hz at Tongariro, New Zealand

(Chapter 2), 1-10 Hz at Cotopaxi, Ecuador (Kumagai et al., 2009), 5-40 Hz at Colima, Mexico (Vazquez et al., 2013), and 5-20 on Mt. Ruapehu, New Zealand for a snow-slurry flow (Cole et al., 2009).

With the wide range of hyperconcentrated flow types, the properties of each flow can be very different. Flows with more water content will have greater cross-channel energy (Lavigne et al., 2000; Cole et al., 2009). Furthermore, Cole et al. (2009) discovered that snow-slurry flows have stronger seismic signals in the flow parallel direction than normal hyperconcentrated flows. The increased amplitude in the flow parallel direction is caused by the greater water content preventing large boulders from colliding with each other or with the channel bed.

1.4.2.3 Snow avalanches

The seismic properties of snow avalanches are unique compared to other types of mass flows. Snow avalanches are the only mass flows that have been proven to show precursory seismic signals before the event occurs. Caplan-Auerbach et al. (2005) proposed that the reason snow avalanches show precursory seismic signals is due to the snow calving and that the initial failure takes place on ice or snow rather than rock (Figure 1.9). Besides the precursory seismic signals, snow avalanches are very similar to other mass flows (Figure 1.10-1.11). The seismograms signals and the spectrogram frequency decay of snow avalanches show the same stereotypical cigar or triangle shape due to the building up and eventual passing of the front by a seismic sensor (Surinach et al., 2005). Most snow avalanches are composed of three layers. At the

bottom of the flow there is dense flowing snow topped by a light flowing snow, which is covered by a snow cloud (Kishimura and Izumi, 1997). The bottom dense layer is where rocks and snow blocks flow and interact with the channel bed to create vibrations detectable by seismic sensors. Seismic signals can also depend on other factors within the flow. Some of these factors include the amount of snow, type of snow or ice, channel geometry, and distance from the sensor (Leprettre et al., 1996; Surinach et al., 2000).

Like all studies involving seismicity there are problems with unwanted noise. In snow avalanche signals, only about 10% of the recorded event is actually the avalanche; the rest is noise (Lawrence and Williams, 1976; Leprettre et al., 1996). Most of the unwanted noise that is recorded during a snow avalanche is from sources like earthquakes, vehicles, weather, animals, and human activity (Leprettre et al., 1996). Along with the above listed external unwanted noise causes, the avalanche itself can create unwanted noise. When an avalanche encounters obstacles such as trees, buildings, etc. down the mountainside, these objects change the seismic signal and frequency response of the avalanche (Surinach et al., 2000). Obstacles are not always a large problem, because they can be seen in the seismic trace and observations and conclusions about the location of the avalanche can be inferred.

Figure 1.10 Seismic waveforms for four Iliamna, Alaska avalanches (Caplan-Auerbach et al., 2005).

Figure 1.11 Three-component seismogram of the 1997 Pointe des Tsarmettes avalanche, Spain (Surinach et al., 2000).

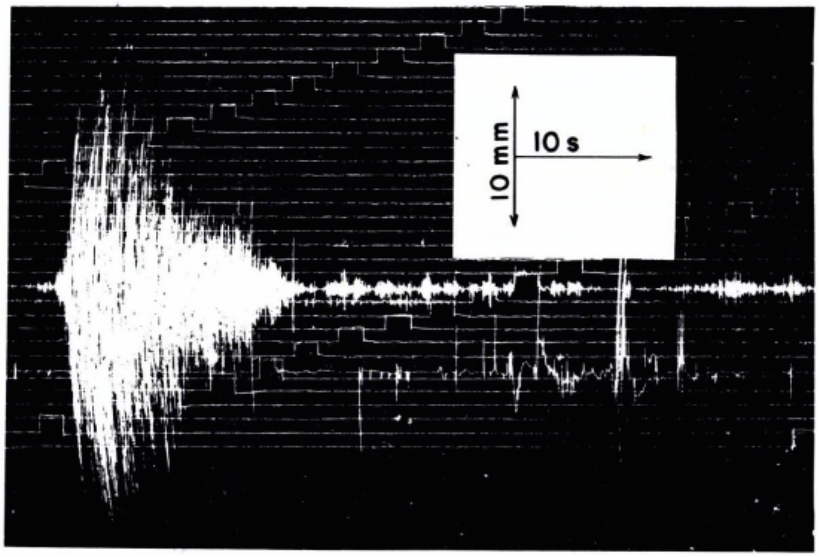


Figure 1.12 Seismic recording of an avalanche on Bridger Range, Montana, USA (Lawrence and Williams, 1976).

1.4.2.4 Granular flows

Rock falls

Rock falls are another type of mass flow that can produce seismic vibrations and has been studied through the use of seismometers (Figure 1.12; 1.13). A rock fall happens when rocks or a block of hard material detaches from a steep slope, but not through shear movement (Deparis et al., 2008). Rock falls are identifiable on seismic traces by a spindle or cigar like shape and an elongated coda or tail along with ambiguous phases or pulses throughout (Norris, 1994; Caplan-Auerbach et al., 2005). The multiple pulses in rock falls most likely coincide with how rock falls form. Different seismic signals will be recorded from the initial detachment from the slope, the rocks impacting the ground after free-fall, the mass propagation down slope, and the interactions of the boulders within the flow (Norris, 1994; Deparis et al., 2008). Rock falls are also distinguishable by their differing amplitudes in each component. Rock falls tend to have higher amplitudes in the horizontal components than in the vertical component (Vilajosana et al., 2008). This is most likely due to the collisions of large boulders in the flow, and might also explain why, along with the three stages of a rock fall event, the spectrograms of rock falls differ from other mass flows. Unlike other mass flows that produce a pronounced tailing off of the triangular shaped signal in their frequency content, rock falls produce spectrograms with wide frequency ranges that attenuate quickly (Deparis et al., 2008; Vilajosana et al., 2008).

Figure 1.13 All three components of a rockfall that occurred in 2007 at Montserrat, Catalonia (Vilajosana et al., 2008).

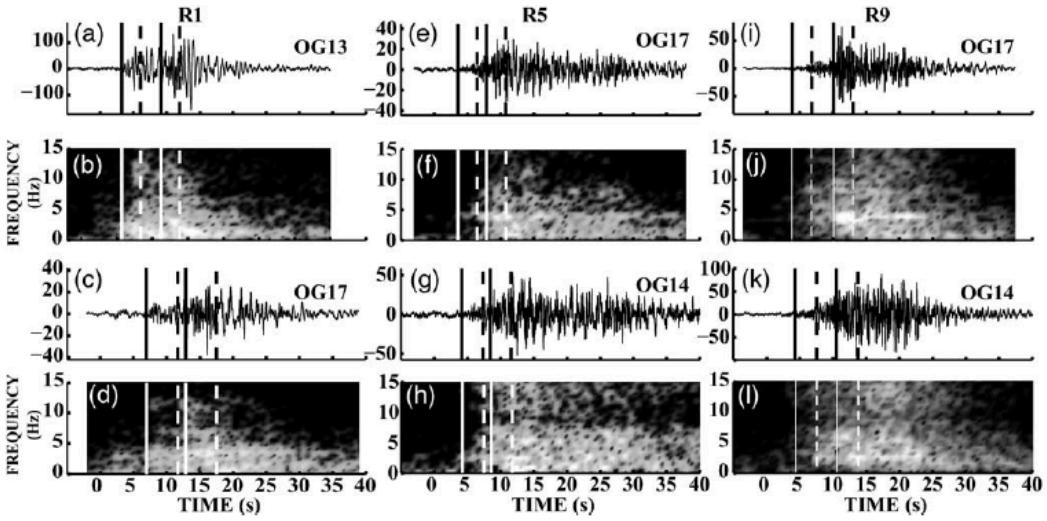


Figure 1.13 Vertical seismograms (top) with spectrograms (bottom) from multiple rockfall events that occurred in the French Alps. The first solid line shows time of P-wave during rupture, while the second indicates the theoretical impact time after the fall (Deparis et al., 2008).

Pyroclastic density currents

Pyroclastic density currents (PDCs) have similar seismic signatures to rock falls, with a cigar shape in the low frequency range (Figures 1.14-1.16), but large wave pulses are introduced when viewing the signal at higher frequencies (Zobin et al., 2009; Levy et al., 2015). The difference PDCs exhibit is that they usually have shorter flow duration times and lower peak frequencies (Zobin et al., 2009). Furthermore these factors are exaggerated due to the tendency for PDCs to escape flow channels or not flow in a channel at all, allowing them to increase coverage by spreading out with time (Levy et al., 2015). Like many other mass flows PDCs also show energy partitioning between seismic components. PDCs show the strongest evidence for distributing the energy of the flow in multiple seismic components. Many have shown that PDCs show higher spectral and seismic energy in the radial components (e.g. Uhira et al., 1994; Levy et al., 2015).

The characteristics of PDCs are hard to estimate because of the lack of an initial propagation phase or lack of small excitations preceding the main flow on the seismogram (Uhira et al., 1994; Levy et al., 2015). For these reasons most PDCs studies contain joint analysis with video observations (e.g. Uhira et al., 1994; Yamasato, 1997; Jolly et al., 2002). Nevertheless, in most cases the volume of the PDC is proportional to the amplitudes on the vertical component of the seismic record (Uhira et al., 1994) and even an estimated value of energy release can be found (Yamasato, 1997; Levy et al., 2015).

Figure 1.14 Seismic signals of pyroclastic flows produced by the partial collapse of the lava dome on Colima, Mexico (Zobin et al., 2009).

Figure 1.15 Seismogram (a) and spectrogram (b) of a pyroclastic flow on Soufriere Hills Volcano, Montserrat (Levy et al., 2015).

Figure 1.16 Seismogram (A) and spectrogram (B) of the August 1999 Soufriere Hills Volcano, Montserrat (Jolly et al., 2002).

1.4.3 Geophysical techniques for determining dynamics and locations of seismic phenomena

1.4.3.1 Phase arrival time

To locate a source of an event using the phase arrival time method is relatively easy due to the simple mathematics involved. Phase arrival uses a velocity model along with P- and S-wave arrival times to calculate a distance from source. To get an accurate location estimation at least three seismograms are needed and adding more sensors will increase the precision of the result. Modern phase arrival techniques use a flat homogeneous multi-layered velocity model, with velocity increasing with depth. The source travel time is estimated from the difference between the P- and S-wave arrival times and then Geiger's method can be used to minimize the root mean squared (RMS) travel time residuals (Lahr, 1989).

The arrival time method works very well for large sources like teleseismic earthquakes, but falters when used to locate local sources (i.e. volcanoes). Many have tried using the method for volcanoes with some success (e.g. Lahr et al., 1994; Aspinall et al., 1998), but had to use many assumptions and corrections. Lahr (1994) found that each type of volcanic event had differing problems. For instance deeper sources had fewer problems than shallower events, and long-period (LP) earthquakes, made S-arrivals difficult to find, due to being overwhelmed by late arrivals. On the other hand the P- and S- arrivals of volcano-tectonic (VT) earthquakes have higher amplitudes then LP events, which make the

phases slightly easier distinguish. The overall problem that arises in volcanic settings is the heterogeneities of the geological structure (Jolly et al., 2014B). Non linear, poorly known velocity models can cause arrival determinations to be difficult due to weak or emergent arrival times especially in the S-phase (Lahr et al., 1994). Other factors that may affect the precision of a location estimate are sparse station distributions, long lasting events (tremor), source depth, and increased unwanted noise (e.g. weather, active volcano) (Almedros and Chouet, 2003). To resolve all of these problems, corrections and assumptions must be made in order to obtain reliable results. Velocity models are assumed to best match with travel times, and each seismic station is given a weighting factor or correction to compensate for differing path and site effects (e.g. resonance, attenuation, elevation) (Aspinall et al., 1998).

1.4.3.2 Coherence

1.4.3.2.1 Semblance

Semblance is a method to locate a source from a signal through finding coherency. Recently semblance has been a reliable tool to locate sources from acoustic data (e.g. Ripepe and Marchettii, 2002; Garces et al., 2003; Johnson et al., 2006), but can just as easily be used for seismic data (e.g. Kawakatsu et al., 2000; Nishimura et al., 2000; Almendros and Chouet, 2003). Semblance was first introduced by Taner and Koehler (1969), but was not fully developed until Neidell and Taner (1971) used the technique as a test against other coherence methods. The semblance method is a form of coherence method based on

normalizing the ratio of the sum of the traces by each individual trace, then cross correlating them (Neidell and Taner, 1971). Once coherency is found, the results can be used in many different ways. The main use of semblance in volcanic research is for locating sources of different volcanic events such as LP events (Chouet et al, 1999), very long period (VLP) events (Kawakatsu et al., 2000; Nishimura et al., 2000; Jolly et al., 2017), volcanic lightning (Johnson et al., 2006), and volcanic tremor (Garces et al., 2003). To locate events, the semblance results are combined with a grid search method to find where the largest coherency is located (e.g. the predicted source location).

Semblance compared to other techniques performs better in terms of the resolution of the properties of the signals. This is due to the fact that semblance uses normalization, whereas simple cross correlation or stacking does not. Normalization of the signals allows for the distinguishing between multiple high signals and prevents unwanted noise from becoming a large determining factor in source location (Neidell and Taner, 1971). Unnormalized methods can be heavily influenced by unwanted noise and produce poor location results (Johnson et al., 2011). However, the semblance method does have problems. The method contains biases in coherence due to producing results that do not contain cross correlation information (Neidell and Taner, 1971). Additionally, semblance often fails for high frequency signals that are complicated by heterogeneities in the geological medium (Alemendros and Chouet, 2003). Moreover, the semblance technique cannot be used for signals with small wavelength to station separation distance, because only with long wavelength to station distance ratios the signals

will always be in phase regardless of the variations in the back azimuth, creating ideal coherency (Johnson et al., 2011).

1.4.3.2.2 Back projection

The back projection technique is a practical and useful method for determining locations and properties of sources. The advantage of back projection comes from the simplicity in computing the calculations due to not needing any *a priori* information about the event or requiring any extensive assumptions on the wave propagation (Ishii et al., 2007). Modern back projection was first used by Ishii et al. (2005) and is based on the reverse-time migration technique used for reflection seismology.

As a wavefront arrives, the sensor records information about the source energy through the amplitude of the recording (Ishii et al., 2007). Due to the information contained in the recording, back projection can take advantage of waveform similarities across multiple stations by normalizing and stacking the waveforms (Ishii et al., 2005; Ishii et al., 2011). By combining the staking process with a grid search technique, properties of the source may be estimated. Next, an energy estimate is calculated for each grid point. Then, by "back projecting" or time shifting each waveform stack at each grid point, the energy release at each point can be determined (Ishii et al., 2007). Summing all grid points can lead to an estimate of the special and temporal source radiation or finding the grid point with the maximum energy output gives the best estimated source location (Ishii et al., 2005).

Back projection has been mainly used to calculate seismic energy release as a function of time and space for large earthquakes (e.g. Ishii et al., 2005; Walker et al., 2005; Kiser and Ishii, 2011), but others have recently successfully applied the method to acoustic source locations (Jolly et al., 2014B). Back projection can be used with multiple sources of data because of its easiness to use and the fact that the technique can be applied to sources at practically any frequency range (Ishii et al, 2007). Although back projection has many advantages, it also has some weaknesses. Firstly, back projection only works if there is a dense array of sensors to record source excitations uniformly as the wavefront propagates through (Jolly et al., 2014B). Another disadvantage of back projection is it requires the energy release of the source to be time independent. If the release of energy is highly time dependent, it can create artifacts from higher energies overpowering the lower energy signals (Ishii et al., 2011). Finally finding source locations at depth is a must when locating events that originate at depth (e.g. large earthquakes, magma movement, volcanic eruptions, etc.), but depending on the type of source and which wave phase is used for back projection, source depths may be poorly constrained and will only be able to locate sources on the surface (Walker et al., 2005).

1.4.3.3 Amplitude source location

The amplitude source location (ASL) method (i.e. Kanamori, 1993) was first used in volcanic settings by Yamasato (1997) and since has been demonstrated to be a useful tool in locating sources. ASL became popular due to the fact that it can

obtain size and location estimates for source events that cannot be located by more traditional methods (e.g. phase-arrival, coherence). ASL uses an assumed velocity and attenuation structure to calculate the amplitude decay and geometrical spreading from a source event (Chapter 2). This combined with a grid search technique can estimate residual errors and by finding the minimum error, a source location can be estimated.

Since ASL uses seismic decay as its core principle, ASL is very successful for large emergent earthquakes (Battaglia and Aki, 2003) and migrating tremor sources (Taisne et al., 2011; Ogiso and Yomogita, 2012). Many others have also been able to use ASL in determining source locations for lahars (Kumagai et al., 2009), debris flows (Ogiso and Yomogita, 2015), rockfalls (Aki and Ferrazzini, 2000), pyroclastic flows (Yamasato, 1997; Jolly et al., 2002), volcano-tectonic (VT) earthquakes (Kumagai et al., 2013), LP events (Bataglia and Aki, 2003), explosion events (Kumagai et al., 2011), seismic tremor (Ogiso et al., 2015), and magma intrusions (Taisne et al., 2011).

The ASL approach does have drawbacks, most notably the necessity of multiple input factors and assumptions that must be used. *A priori* details from attenuation and velocity models must be known or assumed, and can be difficult to determine in heterogeneous areas such as in volcanic terrains. Furthermore, due to local and path effects, seismic stations must be corrected using amplification factors. Amplification factors are needed because seismic amplitudes recorded at the stations in a network are individually affected by local site conditions

(Kumagai et al., 2009). Although these corrections are needed, they are not always helpful. At some locations, such as Tungurahua, Ecuador (Kumagai et al., 2010) or Te Maari in New Zealand (Chapter 3) amplification factors actually make the ASL results worse than not using corrections at all due to radiation pattern effects. Overall the ASL method suffers from uncertainties in amplitude decay and source directivity characteristics along the source to station distance (Chapter 2). More detailed information on particular problems with the ASL method can be found in Chapter 3.

1.4.3.3.1 Amplification factors

Coda wave normalization

In geologically complex regions, for example in volcanic areas, site amplification can greatly differ from station to station because of the many changes in the geological subsurface (Phillips and Aki, 1986; Mayeda et al., 1991). To combat this problem, amplification factors are used to correct path and station effects. The main way to calculate amplification factors is through a process called coda wave normalization. Aki and Chouet (1975) first worked on the idea of using coda waves to calculate amplification factors. Since the first use, many have expanded on the idea of the coda wave normalization method (e.g. Phillips and Aki, 1986; Mayeda et al, 1991).

Using coda waves for calculating amplification factors for ASL is ideal due to the fact that the coda wave normalization technique needs no prior knowledge of ground properties. Coda waves are an averaging of the subsurface through which

they travel, removing all source, path, and site effects from which they come (Aki and Chouet, 1975; Phillips and Aki, 1986). For amplification factors, coda waves are extracted from several regional earthquakes with good signal-to-noise ratios that are well spatially distributed. The starting time for the coda wave has been defined as twice the difference between the origin time and the S-wave arrival time (Aki and Ferrazzini, 2000). To calculate amplification factors, multiple overlapping time windows are cut from the extracted coda wave and root mean squared (RMS) amplitudes are obtained. In order to acquire better quality amplification factors a signal-to-noise ratio (SNR) is introduced in processing and time windows that fall under the SNR limit are removed from the process. Next the remaining time windows from each station are divided by the time windows from a pre-determined reference station. The reference station can be any station in the network, but is usually the station with the highest SNR (Aki and Ferrazzini, 2000). After the time windows have been normalized by the reference station for each earthquake, all the earthquakes are averaged together, along with each time window, creating one amplification factor for each station. For more information and an example of practical use, see Chapter 3.

1.4.3.4 Active source matching

The active seismic source method is a very useful technique for both determining location and energy of an event with relative ease. Active seismic data can come from many different sources, including explosions, large vibration machinery, large drops, etc. The idea to use active sources to determine properties

in volcanic environments first came from Jolly et al. (2012) on White island, New Zealand where they dropped large bags of sand out of a helicopter to determine the velocity and attenuation structure of the island. Later Jolly et al. (2014C) expanded on the drop idea and used active sources on Te Maari, New Zealand to determine properties of the 2012 Upper Te Maari eruption and debris avalanche. In this thesis, the active source method is used to determine locations and dynamics of lahars (Chapter 2) and calibrate the ASL method (Chapter 3).

The active seismic source method needs no amplification correction and no assumptions about path decay effects due to the fact that active source data contains all the site and path information within the recorded seismic signals (Jolly et al., 2014C). While the technique can estimate properties at depth, it is best used for surface events that create surface excitations, such as mass flows (Jolly et al., 2014C). The advantage of the surface excitations is the ability to estimate the energy of an event with time by comparing the energy of the active sources with the event along a path (see Chapter 2.3.3). Although the active seismic source method has many advantages over other location methods, there are still a few downsides. The technique can only be used in locations where active source data are available, as well as, close enough to the natural event. Furthermore, results can only be as precise as the number of active sources used, the resolution of sources, and the same frequency range of the active sources (Jolly et al., 2014C).

CHAPTER 2: SEISMIC ANALYSIS OF THE 13 OCTOBER 2012 TE MAARI, NEW ZEALAND, LAKE BREAKOUT LAHAR: INSIGHTS INTO FLOW DYNAMICS AND THE IMPLICATIONS ON MASS FLOW MONITORING

Chapter Contents

2.1 Introduction……51
2.2 Data……56
2.2.1 Volcanic mass flow background……56
2.2.2 Active source data……59
2.2.3 Natural data……60
2.3 Methods……65
2.3.1 Processing of natural and active source data……65
2.3.2 Correlation between natural data and active source data……66
2.3.3 Estimating energy of natural data from active source data……67
2.3.4 Noise characterization……68
2.4 Results……71
2.5 Discussion……80
2.6 Conclusions……85

This chapter is based on a paper submitted to the *Journal of Volcanology and Geothermal Research.*

Participating Authors:

Braden Walsh (Data processing, data analysis, manuscript development, manuscript writing and editing).

Arthur Jolly (Data analysis, manuscript editing and discussion)

Jon Procter (Map creation, manuscript editing and discussion)

CHAPTER 2: SEISMIC ANALYSIS OF THE 13 OCTOBER 2012 TE MAARI, NEW ZEALAND, LAKE BREAKOUT LAHAR: INSIGHTS INTO FLOW DYNAMICS AND THE IMPLICATIONS ON MASS FLOW MONITORING

2.1 Introduction

Volcanic mass flows are amongst the most destructive naturally occurring events and can affect populated areas, destroying infrastructure and settlements (Angeli et al., 2000). The most common type of mass flow is the debris flow, which can occur on any steep mountain regardless of the occurrence of volcanism (Comiti et al., 2010). If there is volcanic material present, then its remobilization by water may produce a lahar composed of rapidly moving fluidized sediment (Pierson, 1985; Smith, 1986). The term lahar encompasses a wide spectrum of differing concentrations of sediment/rock and water. These non-Newtonian flows also exhibit a range of rheologies, and within a single event can transition between different rheologies (Pierson, 1985). During an event most lahars or volcanic mass flows start as a debris avalanche or a debris flow and as they travel down slope can entrain material or sediment and transform into hyperconcentrated flows (Pierson, 1985, Capra et al., 2002; Pierson, 2005). The quantitative identification and characterization of mass flows may contribute to better predictions and warnings allowing their destructive effects to be mitigated.

The northern Tongariro volcanic complex in New Zealand (Figure 2.1) has presented a range of volcanic phenomena over its 275 ka history including debris flows and lahars (Hobden, 1997). The Upper Te Maari crater is a seismically

conventional volcanic vent located in the northern section of the Tongariro complex (Topping, 1974). Lahars and other volcanic mass flows are prominent in the area and pose a significant risk to the 72,000 people per year that hike along the Tongariro Crossing (Jolly et al., 2014A). On 13 October 2012 the Te Maari lake breakout lahar occurred from a natural dam formed during the 6 August 2012 Te Maari eruption (Jolly et al, 2015A). This lahar was preceded by several weeks of basin rainwater infilling followed by a rapid rainfall event that caused the dam breakout.

Due to the fact that mass flows, including lahars are energetic and thus create seismic energy as they flow, seismometers and seismological techniques can be used to determine important characteristics including their location and energy release (as an indication of event size). Significantly, the seismic energy release is conducive to rapid characterization creating effective monitoring approaches. The characterization of mass flows through seismometers has evolved in recent years through attempts to classify seismic signals and identify specific frequency ranges related to differing mass flow rheologies. Recent work has also focused on how seismic signals change throughout the duration of the flow e.g. debris flows (Arattano, 1999), landslides (Yamada et al., 2013), pyroclastic flows (Zobin et al., 2009), avalanches (Caplan-Auerbach et al., 2005; Bessanson et al., 2007), and lahars (Vazquez et al., 2013; Vazquez et al., 2016). Additionally seismic instruments for monitoring mass flows called acoustic flow monitors (AFM) (Hadley and LaHusen, 1995; Tungol and Regalado, 1996; Galgaro et al., 2005) have been developed purely for hazard monitoring purposes. AFMs are used to capture

ground vibrations from mass flows by only recording in a specific frequency band that correlates to a particular type of mass flow, but suffer greatly from only being able to record in one direction and in a limited frequency range. All of these monitoring and characterization studies using different seismic techniques lead to the next step of locating and tracking a mass flow.

There are two main approaches that can be used to determine the location of a seismic event. These include phase arrival time methods (e.g., Lahr 1989; Lahr et al., 1994), and Amplitude Source Location (ASL) methods (Yamasato, 1997; Battaglia and Aki, 2003; Kumagai et al., 2009). Arrival time methods exploit the earthquake phase arrival time within a known or assumed velocity structure, while the amplitude-based approaches exploit the amplitude decay from the source region within an assumed or estimated attenuation structure. The phase arrival technique is very useful in earthquake seismology, but in volcanic areas it can fail due to weak or emergent phase arrival times, continuous excitations (tremor) from the source, or from the generally higher noise levels. The amount of noise greatly affects the determination of arrival times in the seismograms and may create large errors in location estimates (Almendros and Chouet, 2003). Also, due to the large amount of heterogeneity in volcanic areas, assuming a velocity structure can be very difficult (Jolly et al., 2014B).

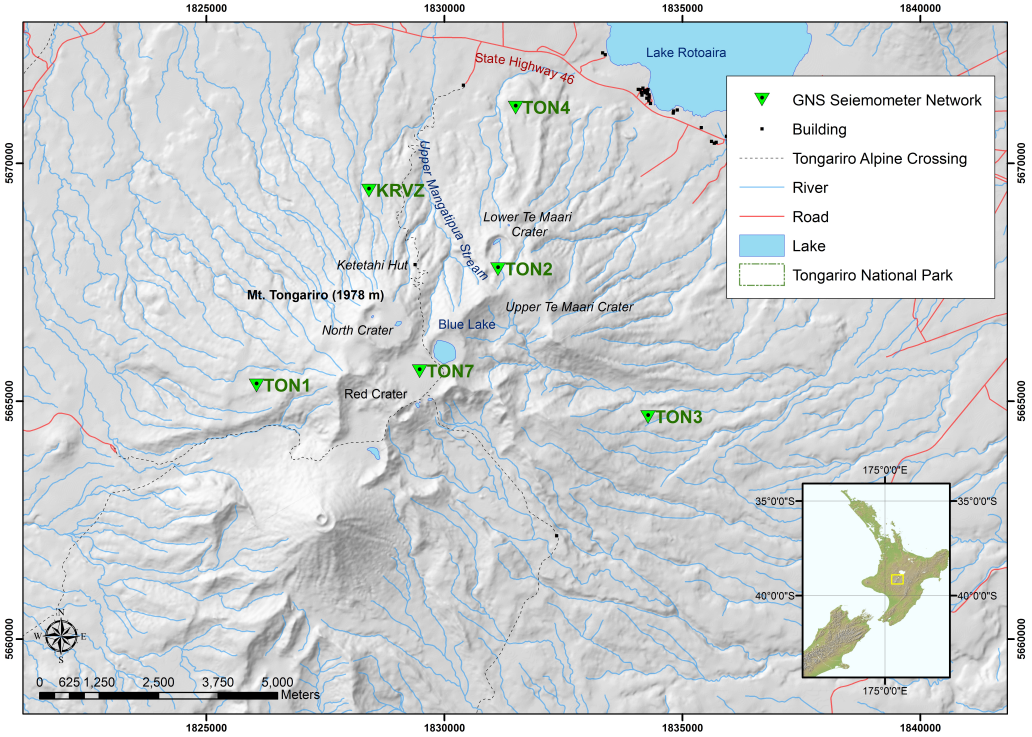


Figure 2.1 Hillshade DEM map of the Tongariro massif. Insert shows location of the map area of the North Island of New Zealand. (Note, seismic station TON2 was destroyed by the 6 August 2012 eruption and was not used). The Upper Mangatipua Stream is the location of the volcanic mass flow channel.

Many studies have used ASL approaches to determine the location of seismicity from lahars (Kumagai et al., 2009), pyroclastic flows (Yamasato, 1997; Jolly et al., 2002), debris flows (Ogiso and Yomogida, 2015), rockfalls (Aki and Ferrazzini, 2000), seismic tremor (Ogiso and Yomogida, 2012), and LP seismicity (Battaglia and Aki, 2003). The method can suffer from many uncertainties however, including variations in source directivity, amplitude decay characteristics along the path from source to station and site amplification effects.

An alternative to the classical ASL approach was recently demonstrated by Jolly et al. (2014C) for a debris avalanche associated with the 2012 Te Maari eruption. In this case, a series of active seismic sources were generated along the Mangatipua drainage channel and recorded on the surrounding seismic network. The amplitude decay characteristics for each active source were compared to the debris flow recorded on the same subset of seismic stations. In this case the decay characteristics of the active source data matched well with the decay characteristics of the debris flow, validating the general approach. The active source approach required no assumptions about path effect decays or site amplification factors because the active source data contain all the site and path information within the recorded waveforms. In this chapter we determine the location, progression, and energy of the 13 October 2012 Te Maari lahar through the same active source comparison. This work will further our understanding of the dynamics of lahar propagation and energy release which will in turn support efforts to distinguish and characterize lahars using remote seismic monitoring approaches. This work extends beyond the earlier work by examining specifically

the seismic noise characteristics from rainfall and wind prior to a lahar breakout event: This condition is common to lahar events, especially in tropical and mountain environments.

2.2 Data

The data for the 13 October 2012 Te Maari lahar were acquired from five seismic stations (KRVZ, TON1, TON3, TON4, TON7) (Figure 2.1) on and around the Tongariro massif. A sixth station, TON2, survived the onset of the 6 August 2012 debris avalanche (Jolly et al. 2014B) but was destroyed by the ensuing eruption, and thus was not available for this study. All the seismic stations used 24-bit digitizers with 100Hz sampling and local GPS time stamps. Stations included Guralp 6T sensors except for station KRVZ that had a short period Sercel L4C3D sensor.

2.2.1 Volcanic Mass Flow Background

The 13 October 2012 lahar was preceded by the 6 August 2012 eruption and debris flow. The 6 August 2012 event began with a short-lived hydrothermal eruption from the Upper Te Maari vent, which triggered a landslide on the western flank of the crater (Jolly et al., 2014A). The resulting landslide produced a debris flow that was bounded by the upper Mangatipua Stream channel, which eroded older debris flow deposits, local vegetation and soil (Procter et al., 2014). The debris flow had a volume of 7.0×10^5 m^3 and affected a total area of 151,000 m^2 within a 2.0 km stretch of the Mangatipua stream (Procter et al., 2014). After the debris flow, a localized basin formed about 1.0 km down slope from the Upper

Te Maari crater impeding the natural drainage system and allowing an ephemeral lake to develop (Jolly et al., 2014A) (Figure 2.2). After the debris flow, the newly formed lake filled with water at a rate of about 3000 m^3/day for the first fourteen days (Jolly et al., 2014A). By 13 October 2012, heavy precipitation caused the lake volume to reach ~50,000 m^3 and the inflow/outflow ratio was approximately 5:1 (Figure 2.3). At this point, the debris flow dam could not restrain the water any longer (Procter et al., 2014) and the dam breached at approximately 11:30 UTC. The event lasted approximately 30 minutes releasing around 80% of the water in the lake and creating a 29 x 12 m opening (Jolly et al., 2014A). Hence, the ultimate cause of the lahar was the 6 August 2012 eruption and debris avalanche, while the proximate cause was the lake filling and breaching of the dam.

The release of water remobilized the older debris flow sediments to form a lahar (Figure 2.4) containing 57,000 m^3 of sediment (Procter et al., 2014). Due to the water to rock ratio of the flow being greater than 50% sediment by volume, hyperconcentrated flow conditions dominated impacting areas farther down the Mangatipua stream than the 6 August debris flow. The lahar had a depth of 1.2 m at its deepest point and moved boulders up to 2.0 m in size (Jolly et al., 2014A). The lahar runout carried mud and sand beyond State Highway 46 (Figure 2.2A), and propagated about 4.5 km from its source region (Procter et al., 2014).

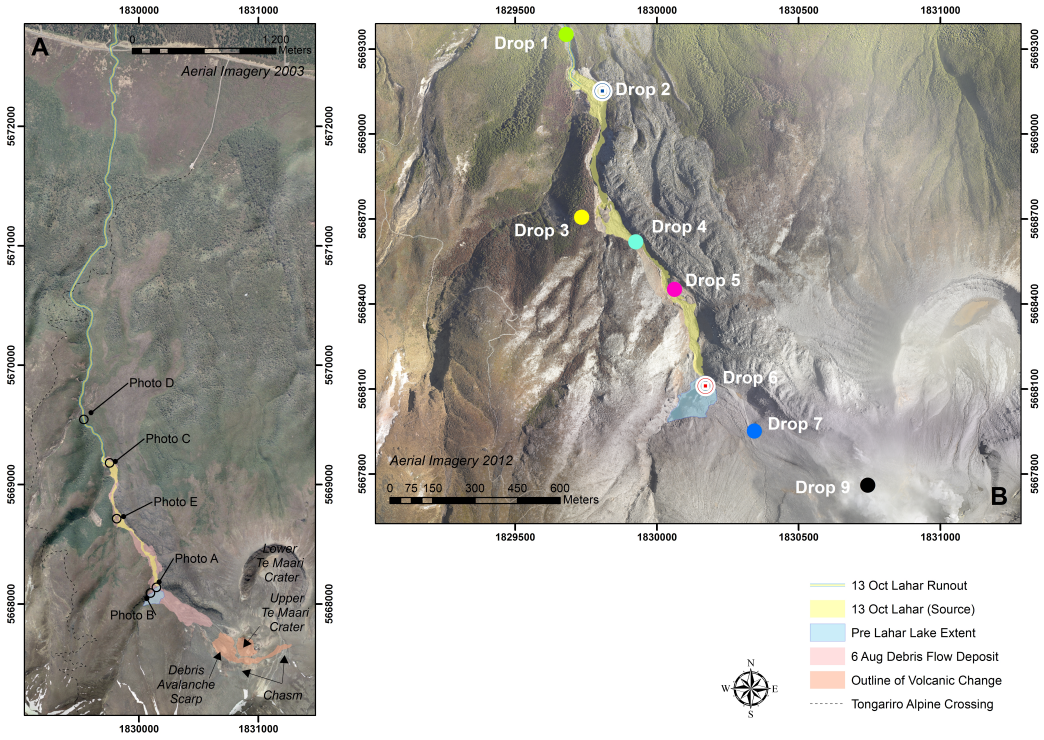


Figure 2.2 A) Map of the volcanic mass flow channel and Mangatipua stream with the runout extent of the 6 August debris flow (red) and the 13 October lahar (yellow). The debris flow scarp, chasm, and the eruption vent are shown in orange. B) Map of the locations of the active source drops along with the 13 October lahar source (yellow), and the ephemeral lake (blue) created by the debris flow dam. Note subsequent figures will utilize the same shapes and colors as the active source drops shown in figure 2.2B.

2.2.2 Active Source Data

Jolly et al. (2014C) collected active source seismic data near the Upper Te Maari crater to determine the properties of the 6 August 2012 eruptions and mass flows. While the 13 October 2012 lahar had very different origins and dynamics, it was constrained within the same channel as the earlier debris flow; hence it is appropriate to use the same analytical approach and active source data as applied in the earlier Jolly et al. (2014C) study. Since the channel and drop locations are the same, the only projected differences between the debris flow and the lahar are the size, magnitude, and the associated uncertainties in the dynamics of the source processes. The 13 October lahar had less volume than the 6 August debris flow and had lower energy and a longer duration. It also suffered from increased background noise due to rainfall runoff and wind noise. These issues were reflected in the seismograms of the 13 October lahar, which included strong noise contributions.

The active source data for the 2012 Te Maari events consisted of eleven drops that were distributed at approximately 500 m intervals along the debris flow channel (Figure 2.2B). To generate seismic impulses, 1000 kg bags of sand or 200-300 kg bags of boulders were lifted by helicopter approximately 1000 m above the surface and dropped (Jolly et al., 2014C). The choice of masses and drop heights was dictated partially by a previous active source experiment at White Island, New Zealand (Jolly et al., 2012), which found that strong seismic wave attenuation limited the wave propagation distance. Of the eleven drops attempted, only eight

produced useable seismic data. For initial analysis of the active source data, arrival times were selected and spectra were computed. A total of 112 spectra were computed for the eight-drop locations recorded at each seismometer (Figure 2.5). The spectra for the active source data are very similar to each other but some patterns can be distinguished: 1) more distant stations (e.g., TON, 1 and TON3) have lower amplitudes than closer stations (KRVZ and TON4), 2) the drops have peak frequencies from about 5-10 Hz at all stations, and 3) drops located closer to the eruption vent have generally lower amplitudes than drops from further down channel. The first observation indicates that amplitude decay with distance is a dominant feature of the data. The second suggests that the impact source process is focused at 5-10 Hz and propagates to distances beyond 5.0 km from the source region. The third observation suggests that either the drops near the volcano are more weakly coupled to the ground on impact, or that the near vent environment is more attenuating than the down channel active sources.

2.2.3 Natural Data

The 13 October lahar seismic data (hereafter referred to as natural data) are distinguished by a cigar shaped waveform envelope (Figure 2.3B) beginning about ~11:30 UTC and persisting for over 30 minutes. Within this tremor envelope, individual pulses are observed and high amplitude noise occurs prior to the dam breakout and lahar onset. Significant wind and rain induced runoff and persistent noise from the active vent, caused strong background noise before and during the period of the lahar. The tremor onset coincides with the start of the decreasing lake

level in figure 2.3A. From the seismic recordings and through spectral analysis it is estimated that the lahar started at ~11:30 UTC and continued for about 30 minutes. During the lahar, there are distinct pulses within the seismograms; these pulses are consistent with step-wise failure of the debris flow dam and its remobilization down channel. This can also be seen in figure 2.3A, where the lake level decreases in three stages before dramatically decreasing.

High noise levels observed during the dam failure hinder efforts to characterize the dynamics of the lahar event and compare the natural and active source data. To ensure that noise effects are minimized, we compute spectra from the pre-event noise and compare this with the dam break and lahar (Figure 2.6). Each spectra is overlain with 10 minutes of pre-event noise, which at some frequencies, has higher amplitudes than the lahar itself. Patterns are noticeable within each spectrum: stations KRVZ, TON1, and TON3 have higher amplitudes at lower frequencies with peak frequencies between 3-5 Hz. In contrast, stations TON4, and TON7 have higher amplitudes at higher frequencies with peak frequencies between 8-10 Hz. These frequency and energy patterns will help later in determining the ideal frequency range for the interpretation of the properties of the lahar. It is important to note that TON7 does not have an east component because of corrupt data.

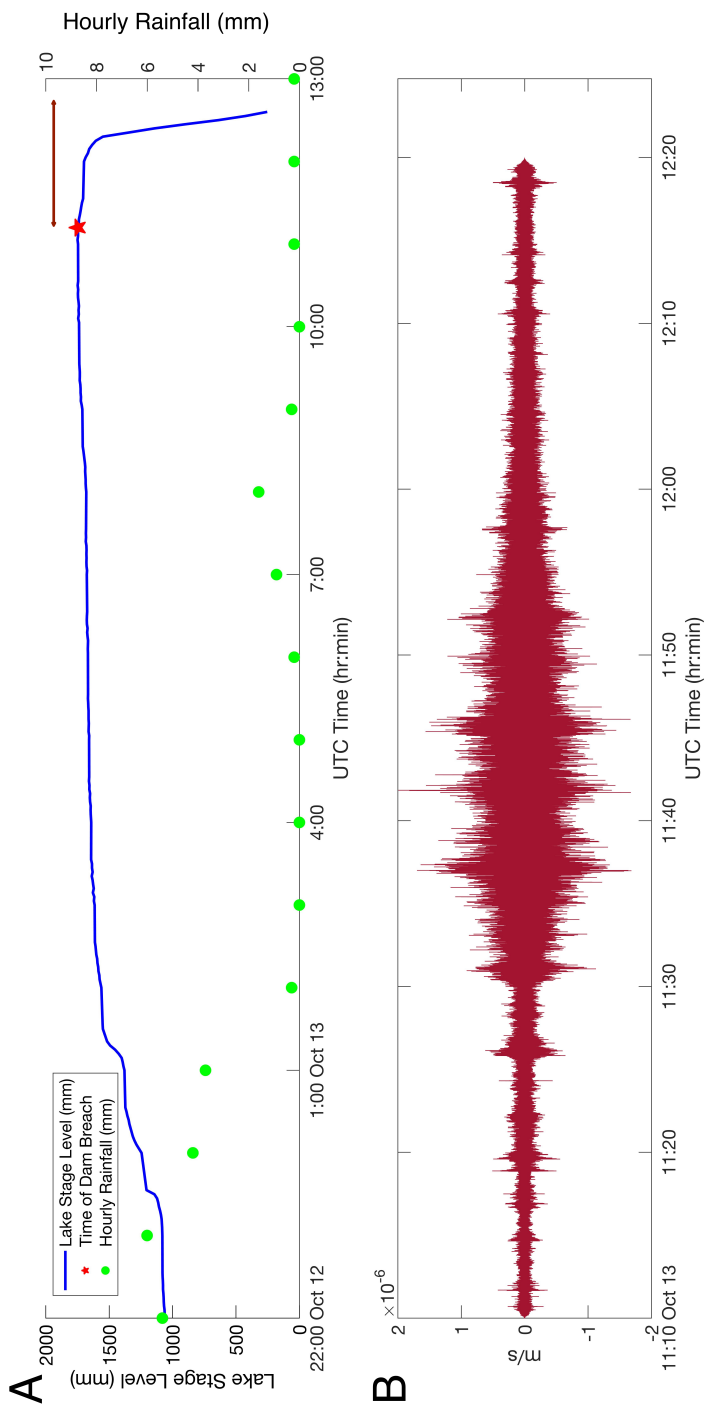


Figure 2.3 A) Graph showing the ephemeral lake level (left y-axis) and hourly rainfall (green circles) in millimeters (right y-axis). The lake level (blue line) steadily increases until the point of the dam breach at 11:20 UTC on 13 October (red star). B) Unfiltered seismogram of lahar from station KRVZ Z-component starting 10 minutes prior and 20 minutes after the lahar onset indicated in 2.3A by the red double arrow.



Figure 2.4 Pictures of the A) Mass flow channel looking up towards the Te Maari vent, B) The debris flow dam and breach, C) Lahar flow, D) Lahar deposits, and E) Stratigraphy of lahar deposits.

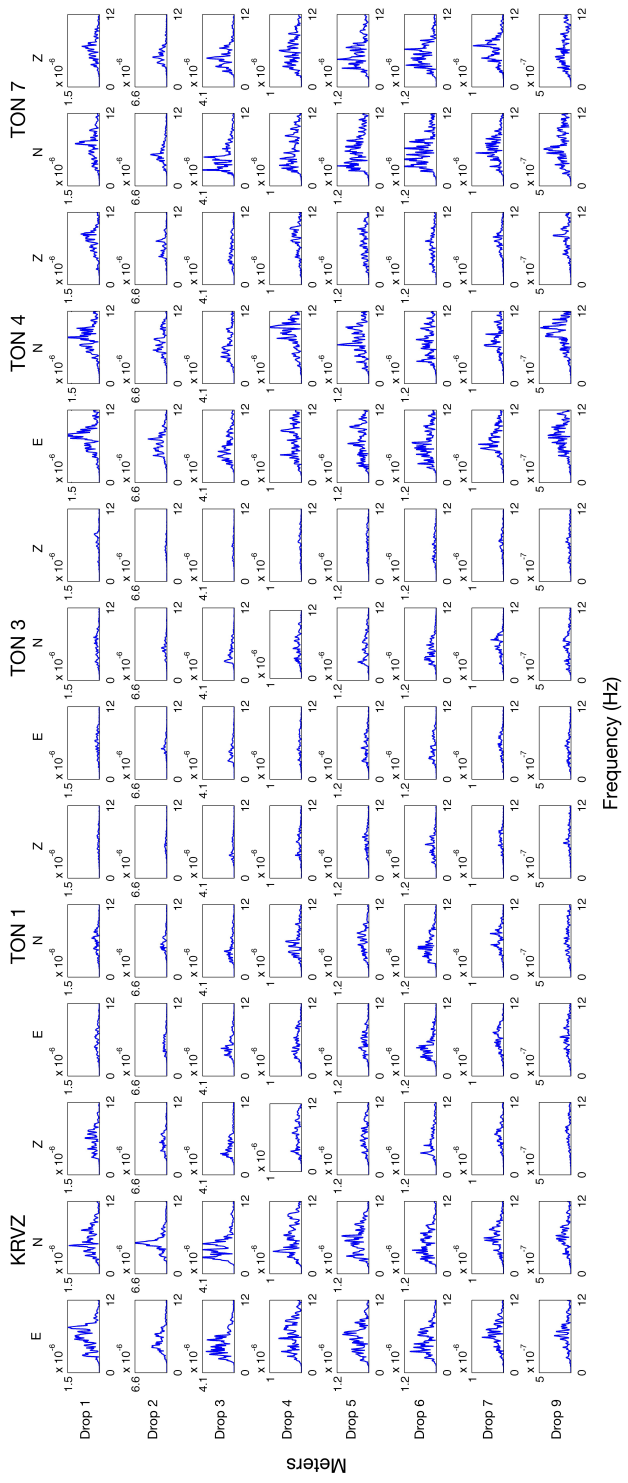


Figure 2.5 Amplitude spectra for 8 active source drops and 14 station components used in this analysis. The spectra include a frequency range between 0-12 Hz. Note TON7 has no East component due to corrupt data.

2.3 Methods

We aim to characterize the dynamics of the 13 October dam breakout lahar by comparing its seismic amplitude distribution to the amplitude distribution from active source seismic data collected in the same stream channel. We proceeded by first completing waveform processing of both active source data and natural data in a consistent manner (Section 2.3.1). Next, we compared the multi-station amplitude distribution for the active source data to the natural lahar event (Section 2.3.2). Then we computed the energy release for the lahar using the active source data for calibration (Section 2.3.3). Finally, we characterized the noise associated with rainfall runoff and wind and then removed data below this threshold from the analysis (Section 2.3.4).

2.3.1 Processing of Natural and Active Source Data

The natural data and the active source data were processed using identical procedures to ensure integrity of the comparison. The raw seismic data for the lahar event were examined for the period 10 minutes before and 20 minutes after the lahar (based on the lake stage data in Figure 2.3A). Next, the natural data were de-trended, and a 1% Hanning taper was applied to the corrected velocity data.

To correlate the active source data with the natural data, we compared the distribution of the available amplitudes. Spectra were computed for a 1024 sample Fast Fourier Transform (FFT) using a two-pass Butterworth filter. This window was dictated by the 10 s impulse response (Jolly et al., 2014C) observed for active source data. For the natural data, the spectra were computed in the same manner

using a non–overlapping moving window. Specific time offsets were also introduced for each station based on the source-to-station travel-time differences at each drop position. Larger distances from the source yielded both greater amplitude decays and larger time offsets in the seismic signals. After spectra were computed for each sampling window for both data sets, the data then were cut to specific frequency bands (e.g. 5-10 Hz, 2-9 Hz) and Root Mean Square (RMS) amplitudes were calculated.

2.3.2 Correlation between Natural Data and Active Source Data

To compare the natural lahar data with the active source data from the drops, a linear correlation was used to determine the maximum correlation. The results relate to finding which drop location correlates best with which time window of the natural data. Sample correlation coefficients may be given in terms of Pearson's equation:

$$R = \frac{\sum(X_i-\bar{X})(Y_i-\bar{Y})}{\sqrt{\sum(X_i-\bar{X})^2 \sum(Y_i-\bar{Y})^2}} \quad (2.1)$$

where R is the correlation coefficient, and $\bar{X}$, $\bar{Y}$ are means (Rogers and Nicewandar, 1988). In order to make the correlation progress more smoothly, two matrices were created: one contained all the RMS amplitudes for each station component of the natural data and the other contained the same for the active source data. Correlation was run on both matrices producing a correlation coefficient cell matrix (number of drops x number of time windows). From each matrix cell the maximum correlation is obtained. The maximum correlation was important

because the value is connected to a specific drop location. Once the maximum correlation coefficient was determined, a list or matrix of best drop locations was determined for each time window of the natural data. We emphasize that the correlation is determined from the distribution of amplitudes at the available stations and is not the classical waveform cross correlation.

2.3.3 Estimating Energy of Natural Data From Active Source Data

The energy of the natural data can be calculated by determining the relationship between the estimated energy input and the measured seismic amplitude output from the active source data. The seismic energy in terms of body waves is shown through Boatwright (1980) and Johnson and Aster (2005) by:

$$E = 2\pi r^2 \rho c \frac{1}{A} \int S^2 U(t)^2 dt \tag{2.2}$$

where r is the source station distance, ρ is the density of the medium, c is the seismic velocity, A is the wave propagation attenuation, S is the site response, and U is the seismic amplitude. Since the active source data contain all the information about geometric decay, attenuation, site effects and bulk Earth properties, equation (2.3) thus can be reduced to,

$$E = G \int U(t)^2 dt \tag{2.3}$$

where G includes all of the wave propagation and site effect terms. To get an energy equation that is useable for obtaining natural energy from the active source energy, a known energy and amplitude from one active source location is G and the direct relationship from a known amplitude to energy is given by equation (2.3),

$$E_i = KEd_i \left(\frac{Ar}{Ad_i}\right)^2 \quad (2.4)$$

where KEd_i is the estimated kinetic energy release of the i^{th} drop location, which can be found on Table 1 of Jolly et al. (2014C), Ar is the RMS average amplitude distribution of the natural data, and Ad_i is the RMS average amplitude distribution of a specific drop location. Each time window of the natural lahar data can be inserted into equation (2.4) and thus the energy for each time window may be calculated.

2.3.4 Noise Characterization

The substantial noise from weather and the active volcano seen prior to and during the dam breakout requires careful treatment before the computation of the lahar source dynamics. For this study a signal-to-noise ratio (SNR) was calculated for each time window of the natural data, by dividing the event signal by the background noise. Since the data were cut 10 minutes before the lahar and 20 minutes after, a more ideal SNR was calculated by

$$SNR = \frac{A_s}{\bar{A}_{ps}} \quad (2.5)$$

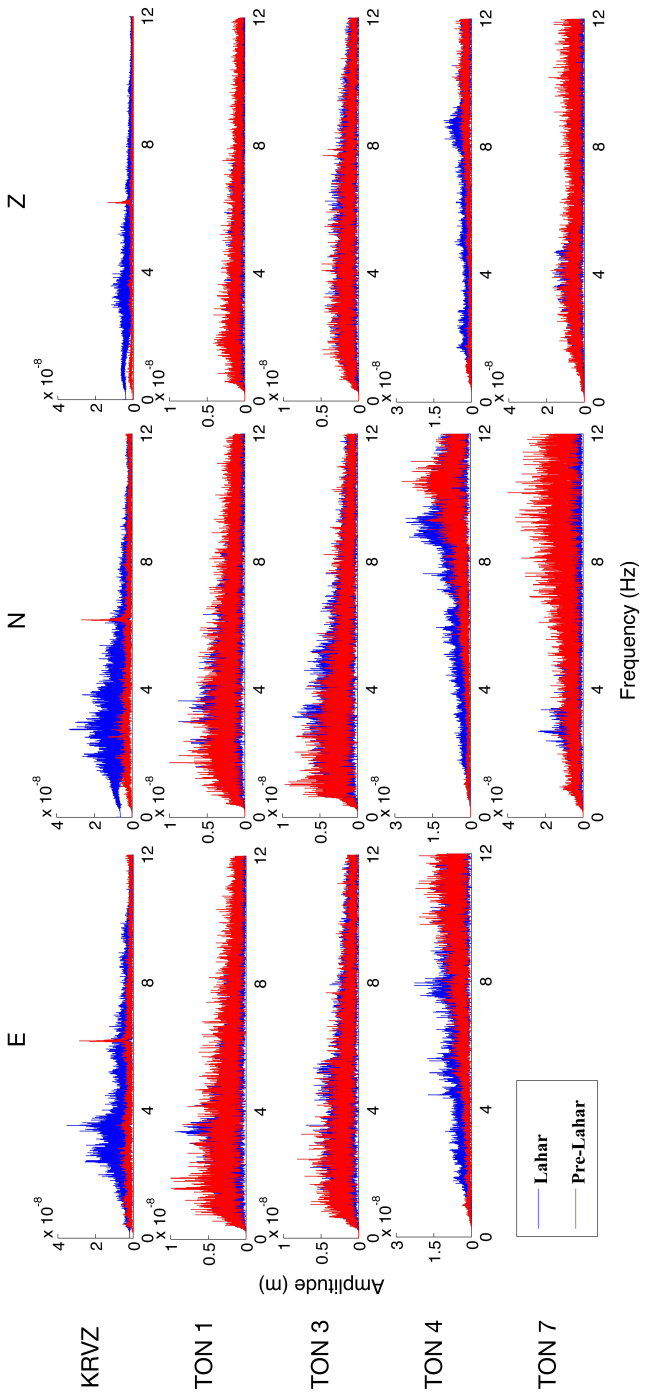


Figure 2.6 Amplitude spectra for the natural data recorded on 14 station components used for this analysis. The spectra include a frequency range between 0-12 Hz. Each spectrogram contains the spectra of the lahar (blue) and an overlay of noise 10 minutes before the lahar (red). Note TON7 has no East component due to corrupt data.

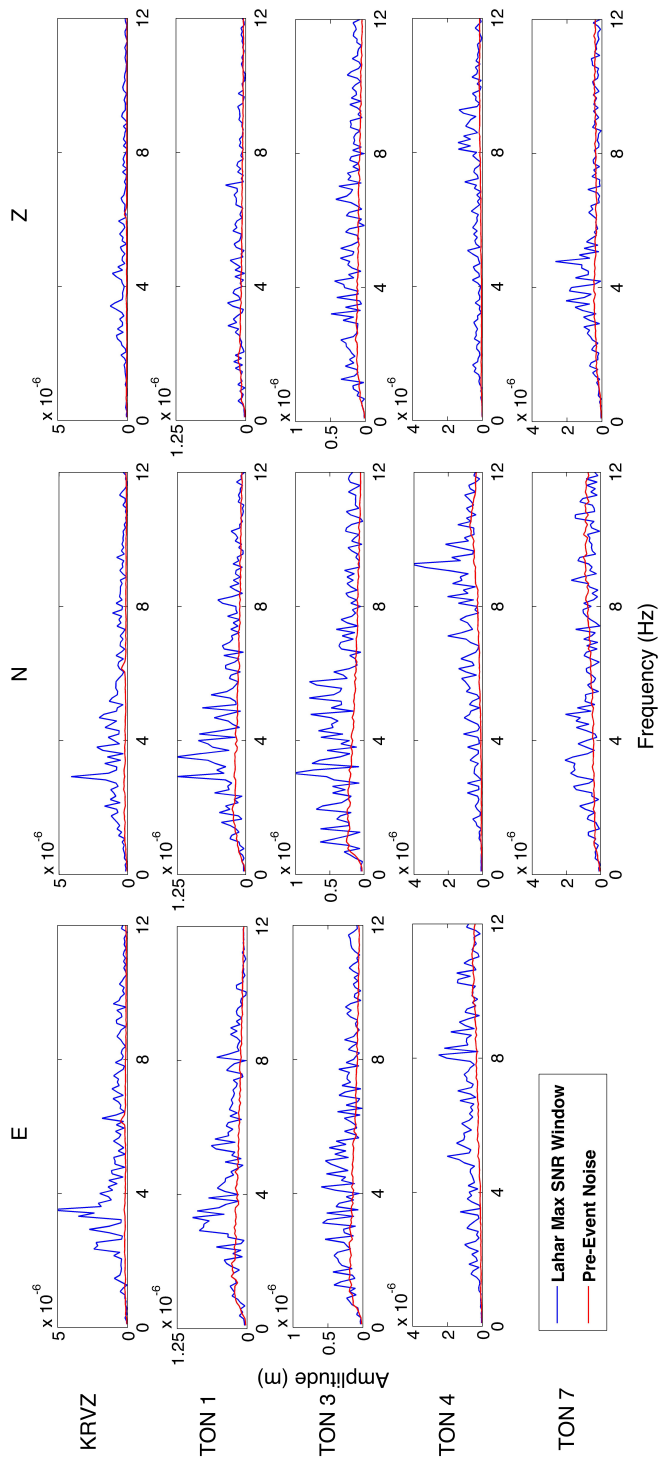


Figure 2.7 Amplitude spectra for the natural data for the maximum correlated time window on 14 station components. The spectra include a frequency range between 0-12 Hz. Each spectrogram consists of the spectra of one time window of the lahar (blue) and an overlay of the averaged 10 minutes pre-lahar (red).

where A_s is the amplitude of the signal, and is the mean amplitude of the pre-event signal, which in this case is 10 minutes before the lahar. By calculating a SNR for each time window, a SNR limit then can be introduced to remove unwanted data below the threshold. The analysis was undertaken from band limited data (e.g. 3-10 Hz, 5-10 Hz) consistent with the spectral bounds seen for both the active source (Figure 2.5) and natural data (Figure 2.6). For example, non-band limited data at a SNR of 2.0 results in 5 usable time windows, whereas band limited data of 3-10 Hz produce 14 time windows above the 2.0 SNR while the 5-10 Hz data yields 12 functional time windows.

2.4 Results

Direct visual inspection of the spectrograms for the lahar and pre-event noise windows in figure 2.6 shows that significant noise is present in all seismograms. Specifically, stations TON1 and TON7 could not be used in the subsequent analysis because the noise overwhelmed the lahar signal at these stations. Alternatively, an examination of higher amplitude portions of the waveform envelope suggests that some sections of the lahar are significantly above the pre-event noise floor. As an example of the best case scenario, figure 2.7 shows the spectra for each station component at the highest SNR time window. This example was created by using 10 min averaged pre-event noise compared with one time-window of the natural data. KRVZ, TON3, and TON4 lahar spectra are above the pre-event noise through the entire frequency range, where TON1 and TON7 have pre-event noise greater than the lahar signal at some frequencies. Additional

filtering of the data was completed through the use of SNRs (e.g. Figure 2.8), which show various SNR limits for the natural data. The strongest SNR is during the period between ~11:30 UTC and 12:00 UTC. This period coincides with the time period of the lahar based on the lake level data. In our interpretation, a SNR limit of 2.0 was chosen to ensure the results were of maximum quality. We also examine results for a SNR of 1.5, yielding a longer time series and adding a higher chance of spurious results.

Three seismic stations were used (KRVZ, TON3, TON4) to compute the best fit location and energy release from the lahar event. Results for a range of frequencies are shown in figure 2.9, where each point represents a 10.24 s non-overlapping moving time window of the natural data, color-coded to the maximum correlated drop location. Multiple frequency bands were examined to identify the appropriate frequency range for interpretation considering three factors: 1) the natural frequency limits for the active source and natural data; 2) which frequency limits match closely to the real dam breakout and lahar position; and 3) the lower frequency limit above which source excitations may average into a mostly isotropic source (e.g., Takemura et al., 2009). Regarding the first criterion, the frequency limits for the active source data are from 3-12 Hz (Jolly et al, 2014C) with peak frequencies in 5-10 Hz. For the highest signal-to-noise time periods (Figure 2.7), the 13 October lahar has a range of 3-10 Hz at KRVZ, TON1, TON3 and TON4 while the peak frequency is 3-5 Hz at KRVZ, TON1 and TON3 and about 8 Hz at TON4. Regarding the second criterion and using the lower SNR threshold, the locations and energy release for lower frequency data (2-6 Hz)

yield source locations (Figure 2.9A) on the lower reaches of the lahar channel (coincident with Drop 3 in Figure 2.2B). This position is not consistent with the dam breakout (Drop 6 in Figure 2.2B). In contrast, the higher frequency 5-10 Hz data yield locations mostly by the main eruption vent. Neither frequency band is consistent with the onset of the dam breakout, which we surmise to be the primary seismogenic locus for the onset of the lahar event (Drop 6 in Figure 2.2B). A broader frequency band of 3-10 Hz (Figure 2.9C) yields an event onset at about 11:30 UTC including Drop 7 and 6 active source locations. Data from the 3-10 Hz frequency band is below the frequency limit outlined by Takamura et al. (2009) for homogenization of the source process. Hence, the third criterion may not be strictly met by an analysis using these broader frequency limits. The 5-10 Hz frequency range, which is also used for classical ASL approaches (e.g., Battaglia and Aki (2003) and Kumagai et al. (2010)), is not ideal in our case because the peak frequencies for the lahar are below this limit. Regardless, the subsequent results and interpretation will be completed using 3-10 Hz frequency limits that are common to both the active source and natural data.

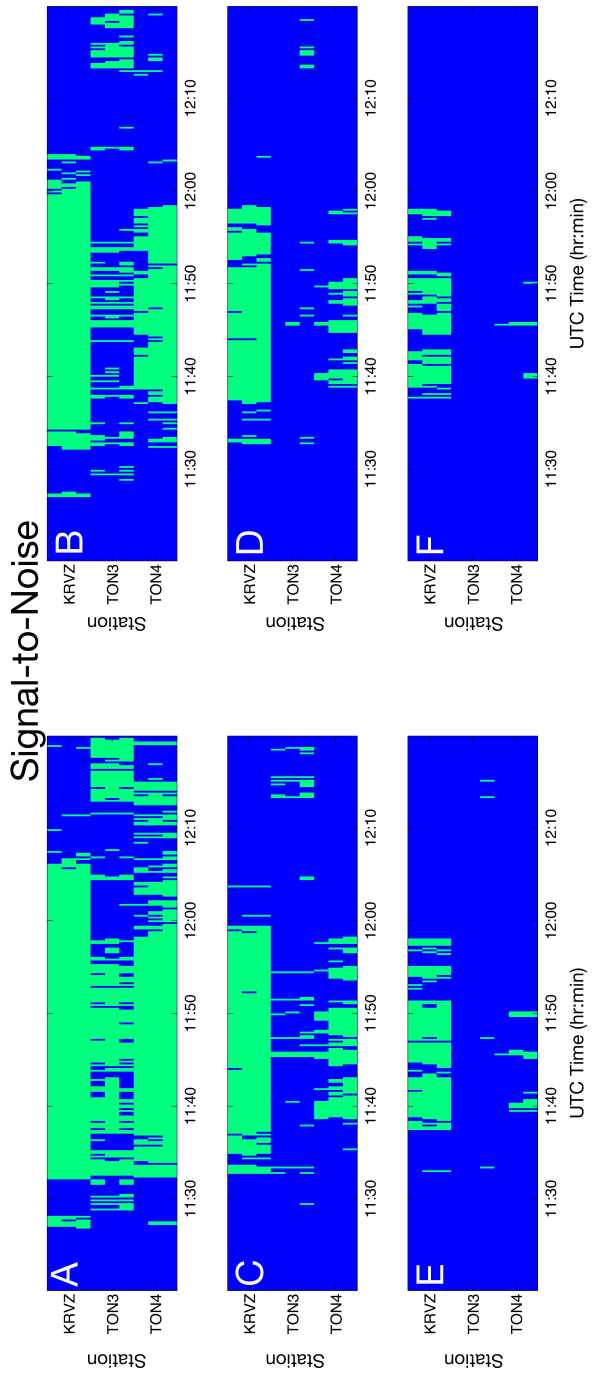


Figure 2.8 Signal-to-noise charts depicting different SNR thresholds at a frequency band of 3-10 Hz for the 9 station components used for the final results for this study, A) 1.5, B) 2.0, C) 2.5, D) 3.0, E) 3.5, F) 4.0. The SNR threshold for time windows below the SNR limit (blue) or above the SNR limit (green).

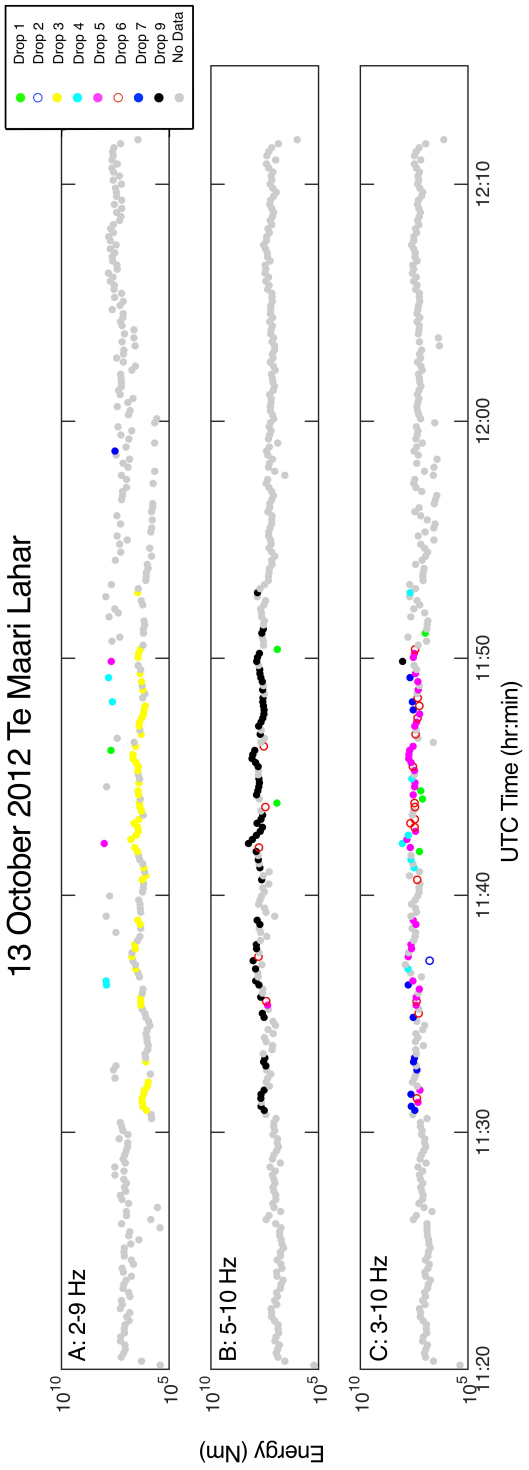


Figure 2.9 Correlation processing and energy release through time for the 13 October 2012 lahar using multiple frequency ranges. Each point correlates to a 10.24 s non-overlapping time window. The points are color coded to match drop locations and grey dots are data that fell below the SNR limit. Further analysis was limited to the 3-10 Hz frequency range (C).

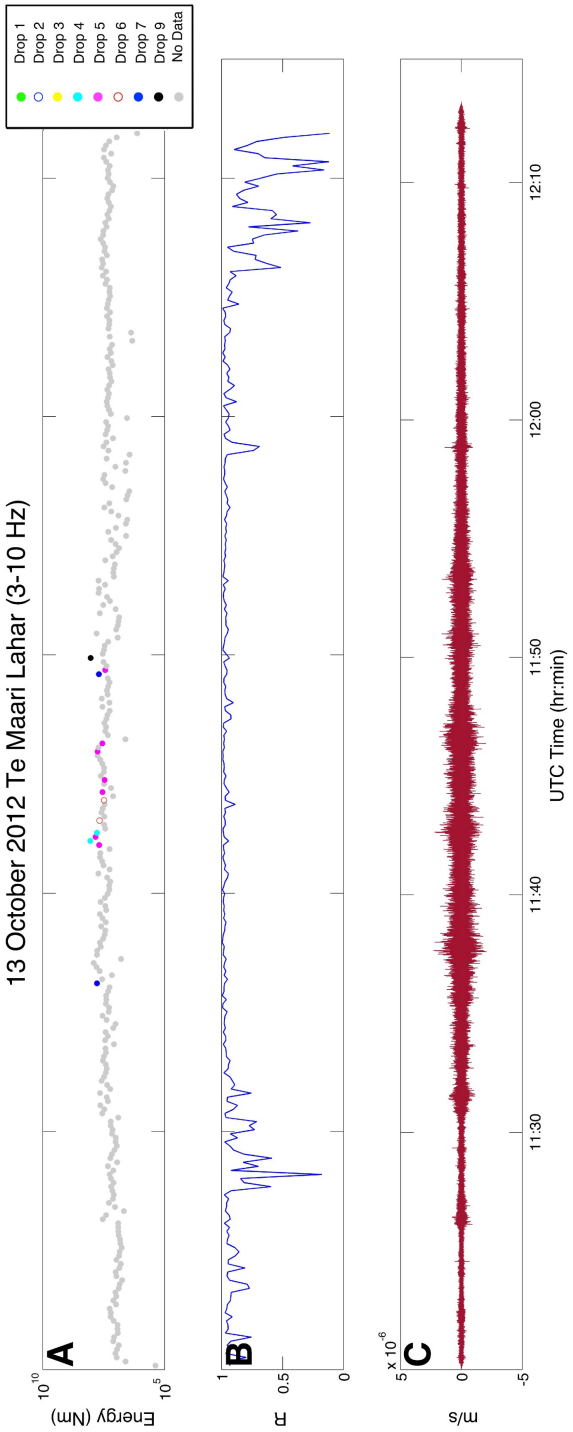


Figure 2.10 Correlation processing for the 13 October 2012 lahar and pre-lahar period. The lahar data were compared to each of the 8 active source drop positions by computing the cross-correlation for a uniform set of 3 stations (9 components) and selecting the best seismic amplitude distribution in a non-overlapping moving time window of 10.24 s each for analysis. Panel A shows the energy release through time with each time window color-coded to the drop location where colors are shown in the legend. Grey dots are "ghost points" or data that fell below the 2.0 SNR limit. Panel B shows the correlation coefficient for the best drop location to the lahar data. Panel C shows the lahar seismogram from the station KRVZ Z-component.

Next we examine results of the correlation processing using the higher SNR threshold >2.0 for the 3-10 Hz spectral band (Figure 2.10); Drop 5 is the most consistent drop location along with Drop 4 and Drop 6 (Figure 2.10A). The location of Drop 6 is directly on top of the ephemeral lake, accounting for the strong matching results. There are also two Drop 7 locations, one at the start and the other towards the end of the event. The high SNR observations (Figure 2.10A) have consistently high cross correlation values (Figure 2.10B) and correspond closely with pulses observed in the KRVZ waveform (Figure 2.10C) as well as cluster around the ephemeral lake and dam breakout location. Given the location uncertainties of ~+/- 0.5 km outlined in the earlier analysis of the eruption and debris flow (Jolly et al., 2014C) we regard the high SNR results (Figure 2.10) to be associated with individual dam breach events.

We next examined the uncertainties associated with the locations by performing a Jackknife resampling on the correlation processing. Jackknife (e.g., Quenouille 1956; Tukey, 1958) uses a general approach where results are recomputed after subset resampling of the underlying data. In our case, amplitude components are randomly removed from the dataset and the correlation processing is reapplied. The nine station components give an 11% chance for each component to be removed for an iteration of the resampling process, yielding a distribution of cross-correlation values and best fit location results (Figure 2.11). We examine three time windows with high SNR limits through 500 iterations of resampling. Figure 2.11A shows the maximum correlation for the specific time window with each drop location, while figure 2.11B shows the minimum

correlation. The time windows chosen occur at UTC 11:31 (lahar beginning), 11:46 (mid-lahar), and 11:51 (late lahar). From figure 2.11, drop locations 7 through 4 all have high correlations with each time window, but there are modest differences between the time windows. The early lahar has lower correlations with lower channel drop locations and higher correlations with the upper channel drop locations. The late lahar time window trends almost inverse to the early lahar. The late lahar is strongly correlated with drop locations farther down channel, but also has high correlation with Drop 9 due to being recorded at a time where the lahar lost most of its energy, hence the weaker correlation coefficient values. The mid-lahar time window has strong correlation values all along the channel, but has maximums in the Drop 7-4 location range, with slightly lower correlations at Drops 1, 2, and 3. The lowest correlation values for the mid-lahar are clearly Drop 9, which is located near the Te Maari vent. The Jackknife results suggest that the onset of the lahar may be associated with upper channel excitations while the late lahar may be subtly related to the lower channel. The Jackknife analysis confirms our earlier assessment that drop locations near the ephemeral lake are best correlated with the lahar.

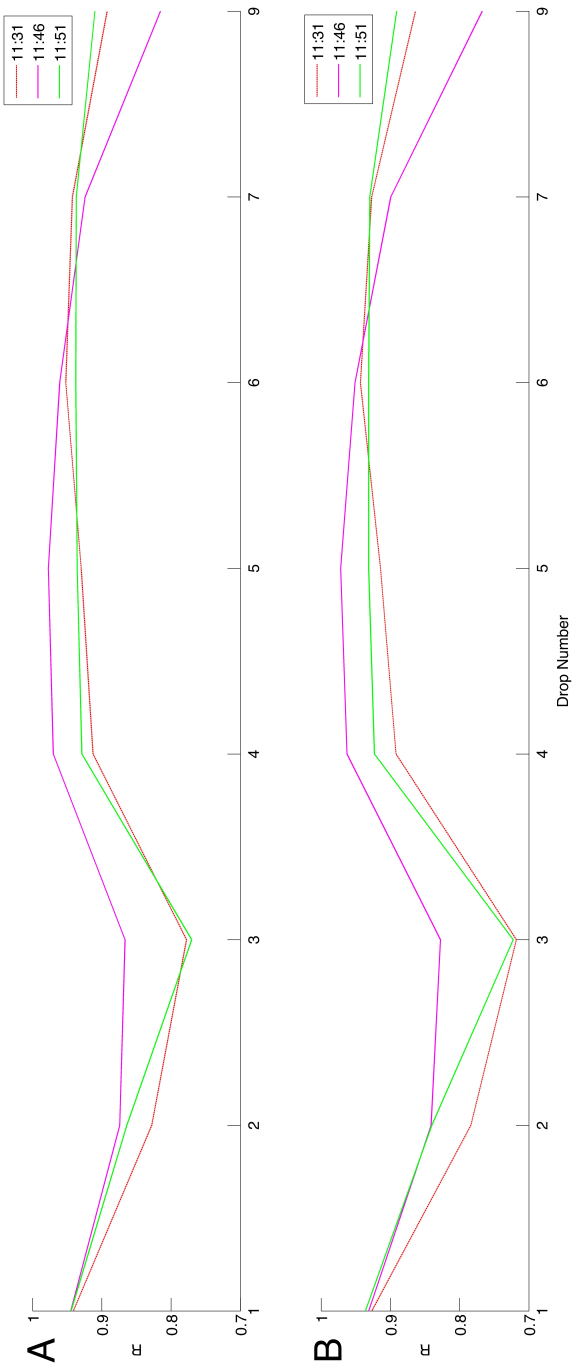


Figure 2.11 Graphs showing three specific time windows (11:31- red, 11:46-magenta, 11:51-green UTC) at various positions in the lahar's progress. Values correspond to the correlation of each time window with each drop location (A) maximum value, B) minimum value) after 500 iterations of Jackknife error analysis. Color on lines correspond to best correlated drop location.

2.5 Discussion

This study shows that correlation processing of natural and active source data is an appropriate approach to estimate the energy and location of the 13 October 2012 Te Maari lahar. The location estimations for tracking the lahar downstream come from the best-correlated drop position. Looking at each time window for the duration of the lahar, distinctive patterns emerge. Drop locations 6, 5, and 4 are related to the location of the ephemeral lake and upper lahar channel. As the lahar propagated downstream, peak energies mostly correlate to these three drop locations. This could simply mean that the results just show a best location match to a mid to upper channel location. When matching the seismogram (Figure 2.10C) with the best located time windows (Figure 2.10A), some similarities emerge. The peak in energies and the pulsing appearance of the seismogram are possibly due to multiple calvings and dam breakouts and/or remobilization of sediment by the lahar. The location of Drop 4 is within the constricted channel; hence excitation from this position may be consistent with either remobilization of sediment or the narrowing of the channel at the location, creating higher lahar velocities.

We surmise that a dearth of observations from Drops 3, 2 and 1 could be related to a lack of flow coupling to the ground at these locations. Alternatively, this could reflect the dominance of calving at the breakout dam over flow coupling further downstream. In this case, high amplitude pulses (Figure 2.10C) would relate to the dam breakout events, while the lower amplitude signals would relate

to down channel flow coupling. In this case, the lower energy observations (below SNR >2) might include the down channel process. Close inspection of the SNR (figure 2.12) supports this hypothesis. Low SNR observations seen in figure 12B include a subset of observations from the furthest down channel observation point (see filled green dots for Drop 1).

The potential energy release and the amount of energy computed from the active source data differ by two magnitudes. In calculating the potential energy the lahar is treated as a single event with one mass for simplicity. The calculations of mass came from the densities and volumes determined by Procter et al. (2014). The mass of the lahar is calculated between 9.4×10^7 and 1.3×10^8 kg within the first 1200 m of the flow at an elevation drop of 220.36 m. With these numbers a potential energy range for the lahar is placed between 2.03×10^{11} Nm and 2.81×10^{11} Nm. Generally the potential energy provides an inaccurate description of the total energy of a mass flow, as the potential energy is not only transferred into kinetic and seismic energy, but most importantly energy can be lost to friction and collision processes (Davis, 1982).

Of the remaining energy given off by the mass flow, only a small amount generates seismically. The computed total integrated kinetic energy for the 2012 Te Maari lahar is 4.87×10^9 Nm with peak energy of 1.12×10^8 Nm. This does not include the pre- and post- lahar data shown in the figures. As mentioned previously, the amount of noise has made it difficult to compute reliable location and energy estimates. The 4.87×10^9 Nm calculated for the lahar's kinetic energy

may be significantly overestimated due to the added noise. To mitigate this, the average pre-lahar background noise was determined and subtracted from the lahar seismogram. When recalculating the energy of the lahar with the unwanted background noise removed, the total integrated kinetic energy is 1.93×10^9 Nm with peak energy around 6.88×10^7 Nm. By removing the background noise, the integrated kinetic energy is about 60 percent less than with the background noise.

With the newly calculated integrated kinetic energy of the lahar, the difference from the calculated potential energy is even greater. The discrepancy between the calculated potential energy and the computed seismic energy could come not only from factors mentioned above but also the lahar itself. Mass flows are known for having poor seismic coupling (Jolly et al., 2014C). Also the Te Maari lahar has strong pulsing (Figures 2.3A and B), interpreted to be sediment breakaways or remobilization of sediment, and the simple potential energy calculation cannot account for these effects.

Characterization of lahars and other volcanic mass flow presents additional challenges due to external related seismic excitations. Noise contamination for lahars may be generated from seismically noisy environments due to the presence of water in the channel or large amounts of rainfall and/or wind from the surrounding area. Unrelated volcanic activity including hydrothermal/magmatic tremor may also contaminate the seismicity originating from the lahar. All of these noise contributions may have been present during the 13 October 2012 Te Maari lahar.

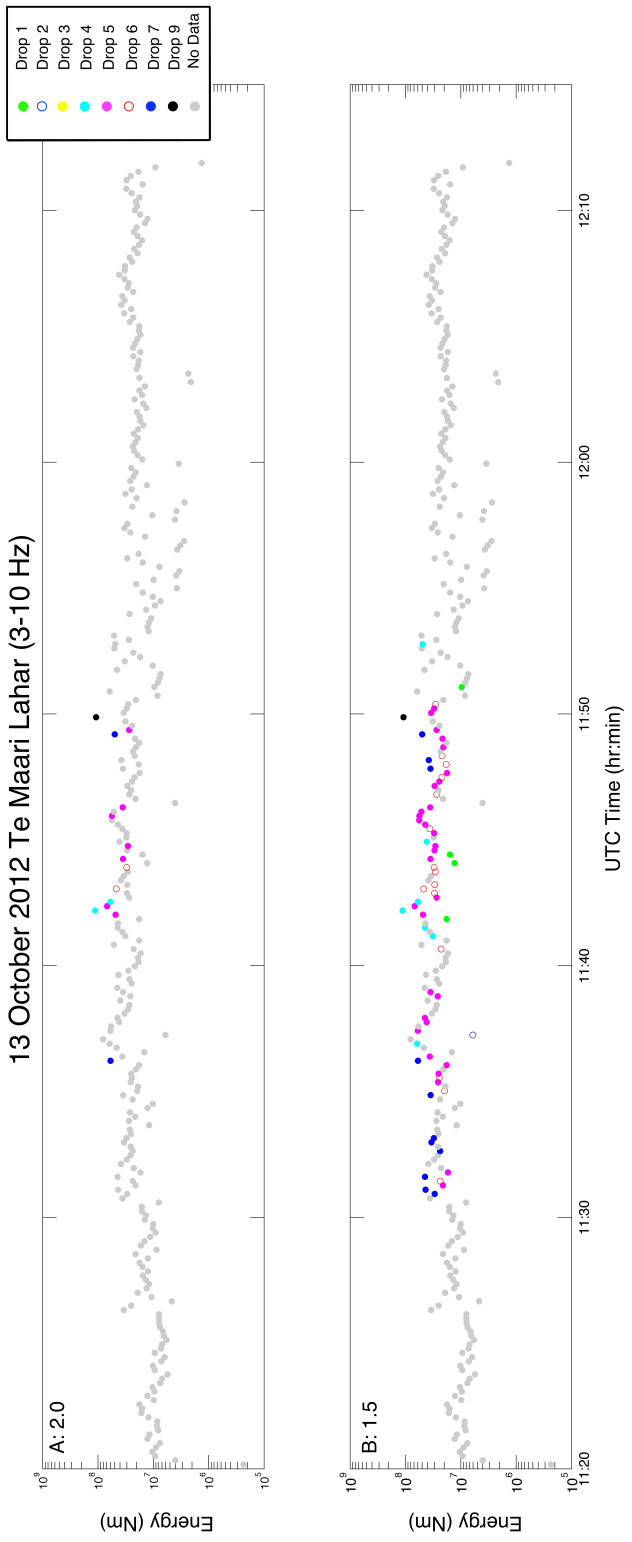


Figure 2.12 Final energy estimates for the 13 October 2012 Te Maari lahar in the 3-10 Hz band displaying two signal to noise results. A) Results with a SNR limit of 2.0, B) results with a SNR limit of 1.5. 10.24s time windows are used and each time window is color coded to the drop location of best correlation; colors of drops are shown in the legend. Grey dots are time windows that fall below the listed SNR limit.

The general application of our active source data to determine the timing, location and energy characteristics of mass flows include some advantages and limitations compared with classical ASL approaches. The primary disadvantage is that the characterization is limited to the number and location of active source data. In our case this is not a strong detriment, because the lahar is confined within the stream channel and source locations are evenly distributed along the channel. This may not be the case with more energetic surface phenomena, however. The classical ASL approach has advantages in ease of application and produces finer granularity in terms of the location process but has not been routinely used to determine the energy release of mass flow events. For example, Kumagai et al. (2009) successfully tracked a lahar using an ASL application to lahar tremor signals, but did not calculate energy. Lube et al. (2012) calculated the potential and frontal energies of the 2007 Ruapehu, New Zealand, lahar, for which they found a potential energy of $\sim 10^{13}$ Nm and a frontal energy in the range of $\sim 10^{12}$ Nm. The Lube et al. (2012) calculation of energy is relevant because of the scale differences in lahar size between the 2007 Ruapehu and the 2012 Te Maari events. Finally, Jolly et al. (2014C) used the very same active source data on the 6 August 2012 Te Maari debris flow through which they calculated similar differences between the potential energy and the calculated active source energy of the debris flow, and also successfully estimated its location.

As a final discussion point, we note that the pulsatory nature of the 13 October event has been observed for other debris flows and lahars in the literature. For example, Lavigne et al. (2000) noted that lahars on Merapi volcano

in Java, Indonesia usually have multiple waves or pulses. Such pulses are very common in debris flows also and have been noted by Anttano and Moia (1999), Kazakov and Minervin (2000), and Naurati et al. (2013). At Te Maari we interpret the pulses to either be the calving or down cutting of the dam and the release of water. Alternative mechanisms such as bulking of the lahar or the pulsation of the flow of material in the lahar due to material flowing over steep lava bluffs (Procter et al. 2014) are also possible but are not resolved by our analysis.

2.6 Conclusions

The 13 October 2012 Te Maari lahar occurred at approximately 11:30 UTC following heavy rain that overfilled an ephemeral lake impounded behind a debris flow dam. The debris flow was created 2 months earlier due to eruptive activity and partial vent collapse from the Upper Te Maari vent region. The lahar, which had no eyewitnesses, was a result of oversaturation of sediments and overtopping and eventual breakout of the debris flow dam. This study compared the seismic tremor amplitudes from the natural lahar to amplitudes generated from active seismic sources distributed along the lahar drainage channel to obtain estimates of lahar tremor location and energy release. The best-correlated locations were found by comparing with one of eight drop locations. During the lahar event the best-correlated locations are with drops near the ephemeral lake (Drop 6) and subsequent drops in the upper channel just below the lake (Drops 5 and Drop 4). The results also show multiple peaks or pulses, which are common for surge like flows such as debris flows and lahars, but in this case may be related to calving and

down channeling of the lahar channel. The cumulative energy calculation ($1.93x10^9$ Nm) for the lahar is underestimated if measured against the straight potential energy treated as a single event and mass ($\sim 2.50x10^{11}$ Nm). While the large difference in energies could be from energy transfer and noise, the most likely difference is from the poor seismic coupling associated with volcanic mass flows and the multiple down cuts in the debris flow dam. With active source information readily available for the Te Maari region, adequate monitoring and consequential calculations of all types of mass flows may be implemented to better understand the mass flow hazards and risks to the area. Future work will focus on application of classical ASL approaches that are calibrated using the existing active source data.

CHAPTER 3: CALIBRATING THE AMPLITUDE SOURCE LOCATION (ASL) METHOD BY USING ACTIVE SEISMIC SOURCES: AN EXAMPLE FROM TE MAARI VOLCANO, TONGARIRO NATIONAL PARK, NEW ZEALAND

Chapter Contents

3.1 Introduction……90
3.2 Data……94
3.2.1 Methods……96
3.2.2 Amplification factors……97
3.2.3 Grid search……98
3.3 Results……99
3.4 Discussion……104
3.5 Conclusions……107

This Chapter is based on a paper submitted to *Geophysical Research Letters.*

Participating Authors:

Braden Walsh (Data processing, data analysis, manuscript development, manuscript writing and editing).

Arthur Jolly (Data analysis, manuscript editing and discussion).

Jon Procter (Map creation, manuscript editing and discussion).

CHAPTER 3: CALIBRATING THE AMPLITUDE SOURCE LOCATION (ASL) METHOD BY USING ACTIVE SEISMIC SOURCES: AN EXAMPLE FROM TE MAARI VOLCANO, TONGARIRO NATIONAL PARK, NEW ZEALAND

3.1 Introduction

Source location and size are amongst the most important parameters in earthquake seismology (e.g., Shearer, 1999) and significant improvements in risk mitigation have developed around the rapid assessment and web based dissemination of these basic observations. Source location approaches usually follow one of three strategies depending on the characteristics of waveforms on the recording network. For impulsive waveforms from brittle failure earthquakes, an arrival time location method is often effective (e.g., Lee et al., 1972), but may produce significant uncertainties for very emergent signals. Waveform coherence methods (e.g., Neidel and Tarner, 1971) are useful when waveforms are low frequency and dominated by radial wave propagation, but often fail for higher frequency signals that are complicated by heterogeneous source and path effects (e.g., Almendros and Chouet, 2003). The correlation of rectified waveform envelopes has also been exploited to determine locations for episodic tremor burst activity in subduction zones (e.g. Ide, 2010). The amplitude source location (ASL) method (e.g., Kanamori, 1993; Yamasato, 1997) has become increasingly popular over the past decade due to its ability to obtain locations and size estimates for events that cannot be located by more traditional arrival-time or coherence approaches. ASL exploits amplitude decay characteristics due to geometrical

spreading and attenuation, and is particularly powerful for emergent earthquakes (Battaglia and Aki, 2003), or migration of volcanic tremor (Taisne et al., 2011; Ogiso and Yomogita, 2012). The approach has also been successful for a range of event types including volcano-tectonic (VT) earthquakes (Kumagai et al., 2013), long-period (LP) events (Battaglia and Aki, 2003), volcanic tremor (Ogiso et al., 2015), explosion events (Kumagai et al., 2011), magma intrusions (Taisne et al., 2011), rockfalls (Aki and Ferrazzini, 2000), lahars (Kumagai et al., 2009), debris flows (Ogiso and Yomogita, 2015), and pyroclastic flows (Yamasato, 1997; Jolly et al., 2002).

Uncertainties in ASL locations include the effects of the amount and distribution of stations, as well as uncertainties in geometrical decay, attenuation and velocity models along with site amplification effects. The large number of model parameters testifies to the system dependency on model inputs that are possible. Kumagai et al. (2010) showed that variations in attenuation models and frequency content might produce strong ASL location discrepancies at Copaxi, Ecuador for LP/VLP earthquakes. By contrast, Kumagai et al. (2013) noted the effects of noise and velocity are less important than amplification factor (AFs) at Taal volcano, Philippines. At Tungurahua, Ecuador Kumagai et al. (2010) discovered AFs were less important than at other volcanoes.

While the effects of input models and AFs have been well studied for the ASL method, the impact of non-uniform station sets is poorly understood. In addition, the concepts of accuracy, the discrepancy between the ASL location and the true

location, precision, and the repeatability of measurements obtained from the ASL, require that the analysis be completed using calibrated seismic data with a known location. Towards this goal, ASLs have been applied to surficial mass flows, where the locations could be directly compared to visual observations and locations within ~1.5 km (Jolly et al., 2002; Kumagai et al., 2009; Ogiso and Yomogita, 2015) could be demonstrated. The nature of the source process in these cases, which is a propagating distributed flow within a long channel, allow only approximately 'true' location estimates; however, an application to a discrete known source would be preferred.

In this contribution, we provide the first high resolution calibration of ASL algorithms and procedures with active seismic source events to better understand the accuracy of the approach and uncertainties from input parameters, AF corrections, and the effects of variable station use. Results show that location discrepancies of ~1.0 km may be achieved for surface events recorded on a 4-5 station network. However, the discrepancy is reduced to ~0.5 km if the AFs are computed directly from the active source events. Corrections for the AFs, computed from regional earthquakes, do not improve the locations in our case, theorized to be from the uneven distribution of our earthquakes or incidence angles of the incoming waves. Standard errors determined using a standard AF computation approach yield significant dispersion in the ASL location at Tongariro.

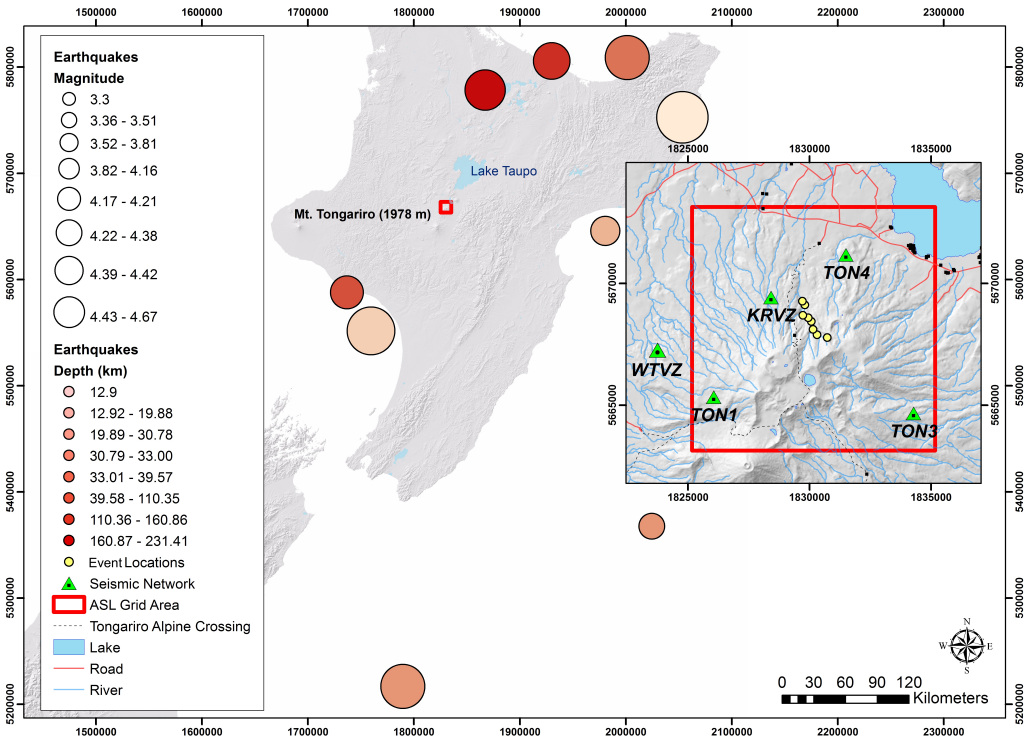


Figure 3.1 Earthquake locations used in the coda wave normalization method to calculate amplification factors (AFs). The red square in the center is the ASL grid area. Active seismic sources are yellow circles and seismic stations are green triangles.

3.2 Data

The active source experiment was completed in February 2013 near the site of the 2012 Te Maari eruption vent in Tongariro National Park (Jolly et al., 2014). Active sources were generated by releasing masses from a helicopter (e.g., Jolly et al., 2012) along a 2.0 km section of the Mangatetipua stream. Masses were composed of ~1000 kg bags of sand dropped from ~1000 m above topography and had impact energies ranging between 7.1×10^6 and 9.2×10^6 Nm. All sites were visited at the end of the experiment to determine impact depths and GPS locations. Of the eleven attempted drops, eight produced seismic impulses to ~6.0 km on the surrounding network and six had sufficient signal to noise ratios (SNR) to compute ASL locations. The data were captured on five 3-component seismic stations (KRVZ, TON1, TON3, TON4, WTVZ) on and around the Tongariro massif (Figure 3.1). All the seismic stations used 24-bit digitizers with 100 Hz sampling and local GPS time stamps. Stations included Guralp 6T sensors except for station KRVZ and WTVZ, which had short period Sercel L4C3D sensors.

To process the active source data P-wave arrivals were picked and the instrument response was deconvolved. Next amplitude spectra were computed from a 1024 sample window having a 256 sample cosine taper. Figure 3.2 shows example waveforms at each of the five stations.

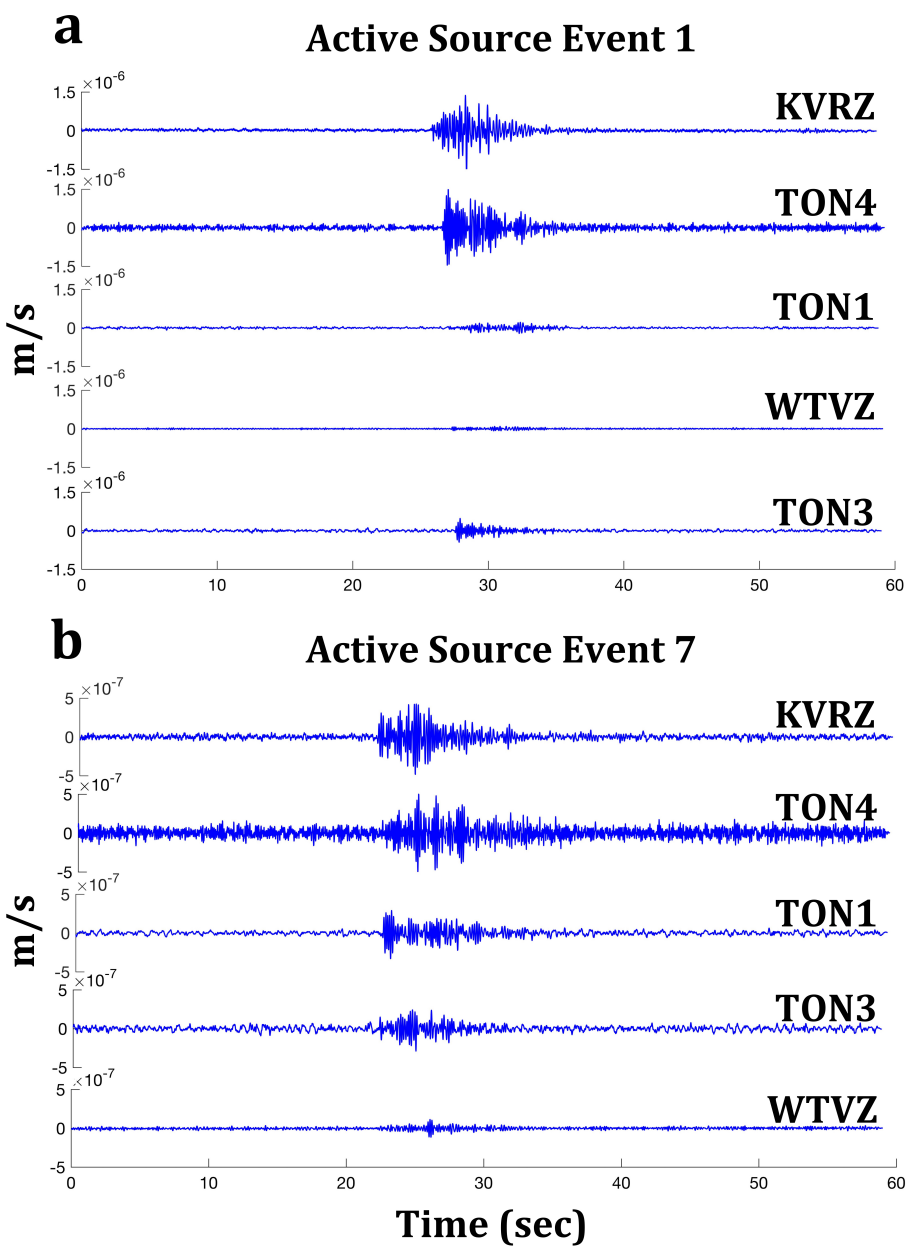


Figure 3.2 Example waveforms for the active source event 1 (A) and event 7 (B) for each of the seismic stations used in the ASL analysis, shown by distance away from source.

3.2.1 Methods

ASL exploits the decay of seismic amplitudes for waves traversing through a geological medium under the influence of attenuation and geometric spreading (Jolly et al., 2002). Following the approach of Kumagai et al. (2009), the amplitude decay of seismic surface waves may be written as:

$$A = A_0 \frac{e^{-B*r}}{\sqrt{r}} * S \tag{3.1}$$

where A is the observed amplitude, r is the source to receiver distance, and S is the site amplification correction. B in equation (3.1) is represented as:

$$B = \frac{\pi f}{Q\beta} \tag{3.2}$$

where f is the average frequency, Q is the quality factor, and β is the average surface wave velocity. For body waves, the geometrical decay is expressed by instead of in equation (3.1) and the S-wave velocity is taken as from Kumagai et al. (2014). Using coda wave normalization and calculating AFs (section 3.2.2) for each station and at an assumed source location, equation (3.1) now becomes:

$$A_0 = \frac{1}{N}\sum_{n=1}^{N} \frac{A_n}{S_n}\sqrt{r_n}e^{Br_n} \tag{3.3}$$

where N is the number of seismic stations and n is a particular station. Errors may then be computed from residuals with the following standard formulation:

$$Residual\ Error \equiv \frac{\sum_{n=1}^{N}\left[A_n - A_0\frac{e^{-Br_n}}{\sqrt{r_n}}\right]^2}{\sum_{n=1}^{N} A_n^2} \tag{3.4}$$

The input frequency of 3-10 Hz was used for the determination of amplitudes A_n consistent with prior ASL research. However, Takemura et al. (2009) noted that source features below ~5.0 Hz would not have homogenous source radiation patterns from its source mechanism and such effects might influence the final location results. However, we surmise that lateral variations in the source radiation would be minimal for the vertically impacting active sources used in this study. Next, due to poor energy coupling, only seven out of the eight active sources were used for the calibration. Event 9, which landed on the Te Maari cone, was excluded due to its smaller mass, lower energy release, and high SNR compared to other active source events (Jolly et al, 2014).

3.2.2 Amplification factors

Local site characteristics can adversely affect the amplitude of the recorded seismic impulse. These local distortions can be mitigated by applying a normalization (S_n from equation 3.3) from the average of several earthquakes recorded on the local network. We used the coda wave normalization method based on Ogiso and Yomogita (2015), which was originally introduced by Phillips and Aki (1986). Nine regional earthquake (Figure 3.1) waveforms, filtered between 3-10 Hz to match the active source events were extracted from the GeoNet database, and coda wave AFs were calculated. The starting time for the coda wave has been defined as twice the difference between the earthquake origin time and S-wave arrival time (Aki and Ferrazzini, 2000). At the coda onset, the root mean squared (RMS) amplitudes were calculated for three 10.0 s time windows having

5.0 s overlaps. To reduce noise contamination, an SNR ≥ 2 was selected. The noise window was calculated from a 10 s time window before the P-wave arrival and coda time windows that fell below the selected SNR were removed. Time windows from each station were divided by the reference station (TON1) and the mean and standard deviations were computed (Table 3.1).

3.2.3 Grid search

The active source data were located by finding the minimum residual error from equation (3.4) in a grid search. The grid encompasses a 10 X 10 X 2 km volume centered on the active source region (Chapter 2) and has a 100 m grid spacing. Exploiting equation (3.4), a best-fit location was estimated for each active source, and then compared to the known source position. For our purposes, surface excitations are assumed to generate a significant portion of surface waves, but may have body waves also. Subsurface excitations would incorporate body wave geometrical decay into equation (3.4), hence the grid search is extended to depth for both surface and body wave analysis. The grid spacing for depth uses surface elevation as zero depth for the consideration of topography in the results. Input baseline parameters for the grid search included a surface wave velocity of 1500 m/s (Jolly et al., 2014) and a quality factor of Q=60 (Titzschkau et al., 2010) for all subsequent sensitivity analyses except where indicated.

Table 3.1 Amplification Factors

Station	AFs Earthquakes	Standard Deviation	AFs ActiveSource	Standard Deviation
KRVZ	0.8645	0.3412	0.5883	0.1551
WTVZ	1.3479	0.752	0.54775	0.0578
TON1	1	NA	1	NA
TON3	0.7878	0.2303	1.1112	0.5229
TON4	0.7819	0.1297	1.1296	0.485

3.3 Results

Stable residual minimum locations were obtained (Figure 3.3A) for the vertical waveforms within the search grid region for constrained input parameters including velocity, attenuation and AFs. For the six active sources the ASL locations corrected by AFs (green circles) are at greater distances (up to 1.3 km) from the source than for the solutions without AFs (red circles). This could be due to the uneven distribution of regional earthquakes (Figure 3.1) or alternatively might reflect the local heterogeneities or anisotropy in the Te Maari region (Johnson and Savage, 2012).

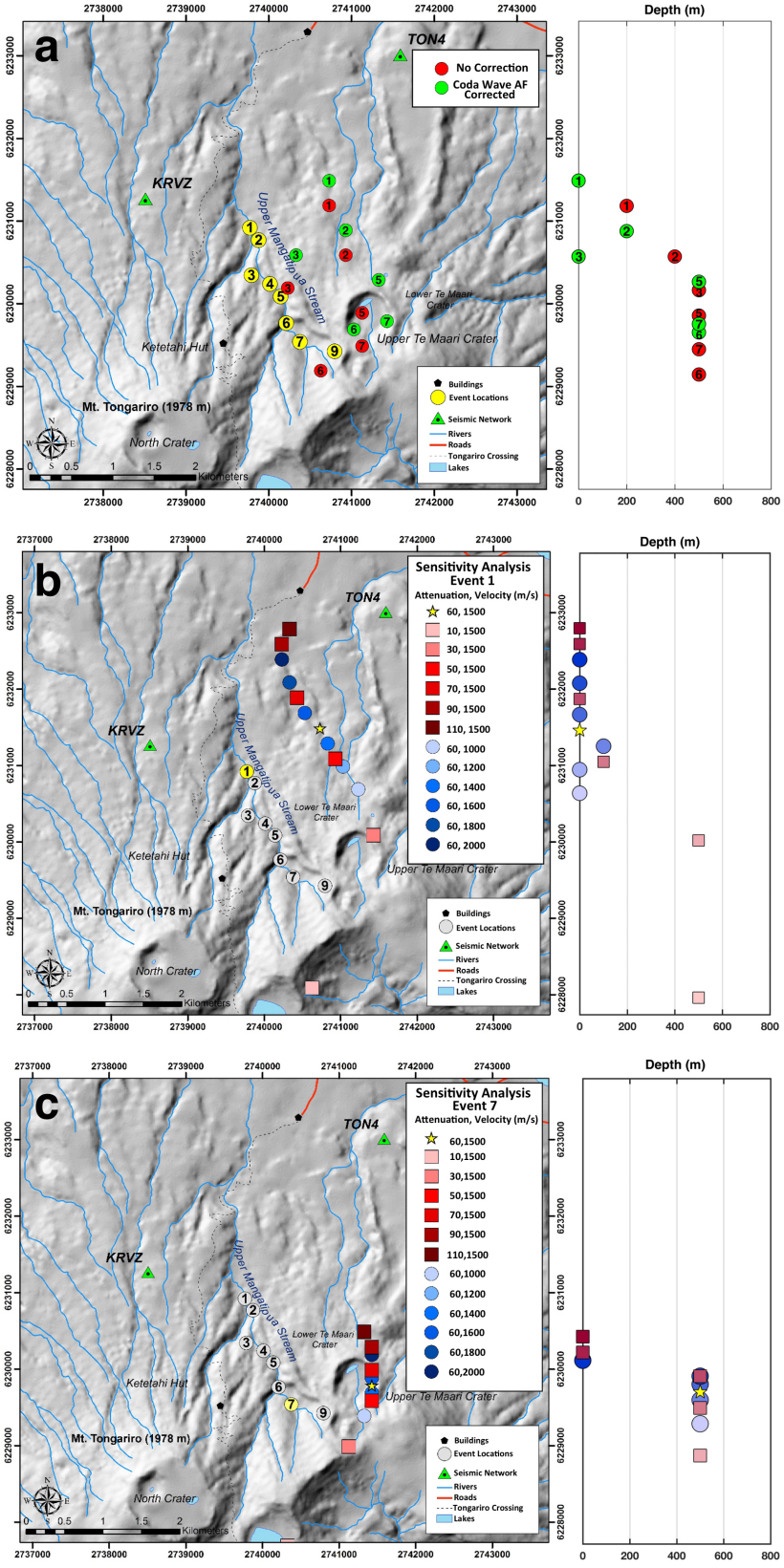


Figure 3.3 A) Location of active source events used in this study (yellow circles) and surface wave ASL locations with corrections with AFs (green) and without (red). B-C) location results for events 1 and 7 with variable attenuation and velocity. Stars represent the base value of an attenuation of Q=60 and a surface wave velocity of β=1500 m/s, while the attenuation is represented as squares and velocity as circles.

We next examine the sensitivity of the ASL input parameters by varying the velocity and attenuation from the aforementioned base values (Figure 3.3A and C). We have conducted this analysis with all six events, but limit the presentation to events 1 and 7 for clarity. For all events, the minimum error location only changes along a line semi-parallel to the channel and never moves significantly towards or away from the true location. Increasing the attenuation value or the velocity moves the minimal residuals down slope from the volcano, while decreasing the same values moves the locations toward the vent, which is consistent with the theoretical tradeoff shown in equation (3.2). Systematically changing attenuation values with set low and high velocity values (results not shown), yield suboptimal locations with higher residual errors. We find that lower channel active source events (event 1) are highly sensitive to both the assumed velocity and attenuation (Figure 3.3B). In contrast, the upper channel (Figure 3.3C) active sources (event 7) are relatively insensitive to the input velocity or attenuation. Intermediate channel positions show a gradual evolution from strong to weak sensitivity to these parameters (results not shown).

We surmise that sensitivity to velocity and attenuation models is related to the station geometry and relative station distance to the sources. Down channel (event 1) sources are closer to KRVZ and TON4 yielding larger amplitudes than TON1 and TON3 (Figure 3.2). In contrast, event 7 is closer to the center of the 5 station array and the observed station amplitudes are less varied (Figure 3.2). In our case, uncertainties in decay models may be expressed by strong lateral location sensitivities at positions where strong amplitude differences are observed. In

contrast, the sensitivities might be accommodated by changes in the event depth, when the station amplitudes are similar. This is the case for the upper active sources where events 5,6, and 7 cluster at source depths around 500 m. In contrast, events 1, 2, and 3 all cluster at or near the surface.

Given the tradeoff in lateral and depth changes in our sensitivity tests, we next examine the effects of applying a body wave decay model to the calibration data. The body wave minimal residuals tend to group closer to the Upper Te Maari vent (Figure 3.4A), whereas the surface wave results are more spatially similar to the true active source locations. The average epicentral distance from the true source positions are very similar, ~1.2 km for body wave decay and ~1.0 km for the surface wave decay. The body wave decay model yields location depths ~500 m below the surface regardless of event location. For the surface wave decay model, lower channel events are systematically shallower than their upper channel equivalents (Figure 3.4A).

In addition to the standard ASL corrections and sensitivity tests, we examined the effects of: 1) re-locating events using non-uniform station sets, 2) sensitivity of locations to the natural AF uncertainties, and 3) creating AFs from the active sources.

Multi-station location algorithms are highly dependent on the station use patterns, which can introduce substantial location errors (kms or larger). These can be evaluated using standard bootstrap and Jackknife methods (e.g., Lahr, 1989; Waldhauser and Ellsworth, 2000), which are designed to assess the effects of

station use. We assessed the direct effects of station geometry errors by systematically removing stations to evaluate their influence on the location process. For small sample sizes this is similar to using the Jackknife method for only 5, 4, and 3 stations (Figure 3.4B). The computation yielded lateral distribution errors of ±1.60 km, and depth errors up to ±150 m for event 1 and errors of ±1.40 km and ±200 m respectively for event 7. Station KRVZ has the strongest influence on the location errors, and location results including only WTVZ, TON1, and TON3 produced the largest departure (6.10 km for event 1 and 4.65 km for event 7) from the true active source position.

Next we examined the distribution of location errors due to uncertainties in the computed AF corrections. We used the AFs and their standard deviations (Table 3.1) to generate a random normal distribution of AF corrections. For each of 1000 randomly generated AF corrections, a location was computed, producing a spatial hypocentral distribution indicative of the location uncertainties associated with the AFs standard errors (Figure 3.4B). The results show substantial lateral location errors of ±0.87 km and depth errors of ±140 m for event 1 and ±0.85 km and ±230 m for event 7.

As a final test we compute the AFs based on the measured amplitudes for the active source data (e.g., use the active source data as inputs to compute the AFs). As anticipated, the calibrated corrections yield locations on or near the debris flow channel with an average true error distance of ~0.50 km at depths around 400-500 m (Figure 3.4C) for all active sources except event 1. The discrepancies

between active source location and those computed using active source AFs is probably due to highly localized variations in the attenuation, and velocity, as well as local source variation effects.

3.4 Discussion

Many influences can affect the ASL location including the geometrical decay model, attenuation, wave velocity and the site corrections (AFs) drawn from aggregate regional seismicity. In addition, the array geometry and station density influence the computed ASL location.

At Tongariro, both the local velocity structure and attenuation have been estimated and the spread of test values (Figure 3.3B and C) are much larger than the true uncertainties of these model inputs. The inherent value of these sensitivity tests in this case is to obtain an understanding of how such uncertainties are accommodated within the given station geometries. In our case, the proximity of the active sources to stations KRVZ and TON4 produce a significant distortion of the location depending on the input velocity. This effect is stronger in down-channel positions, while upper-channel sources are accommodated by changes in the depth (Figure 3.3B and C).

The results show that station geometry and station density are possibly the most important influences on the ASL accuracy (Figure 3.4B). Average location errors of ~2.0 km from true location are obtained with a sparse network geometry (three stations). ASL locations will often utilize uniform phase sets from small numbers of seismic stations, and such studies may have substantial absolute

location errors, but reasonably good location precision for different observation times. New ASL approaches have exploited the amplitude ratios between seismic stations (e.g., Taisne et al., 2011) for continuous tremor sources. In these cases, the absolute accuracy is less important than the precision of the measured ratios and small amplitude changes may be related to source migration. This precision estimate is not in the scope of the present work, but active source analysis of such methods could improve interpretations from these particular ASL approaches.

AFs have been applied successfully at some volcanoes, e.g. Cotopaxi, Ecuador (Kumagai et al., 2010), and Miharayama, Japan (Ogiso and Yomogita, 2015), while at others, including Tungurahua, Ecuador (Kumagai et al., 2010), and Te Maari, New Zealand (Figure 3.3A), AFs actually impair the location quality. This has led to Kumagai et al. (2015) forgoing site amplification factors in determining locations at Tungurahua. The AF sensitivity analysis completed here (Figure 3.4B) suggests that such corrections may introduce significant uncertainties into the location process. Site and area effects, as well as the uneven distribution of earthquakes due to the tectonic setting of New Zealand, which could increase location uncertainty, influence the AF computation. Examination of the standard errors for the AFs in Table 3.1 suggests that they will only offer first order corrections to the data. We find that the standard errors for AF datasets should be incorporated into the ASL error analysis to inform the location uncertainties. Resampling of the AFs using the standard errors shown in Table 1 yield an average true location error of ~1.40 km at Te Marri, which encompass the active source equivalents.

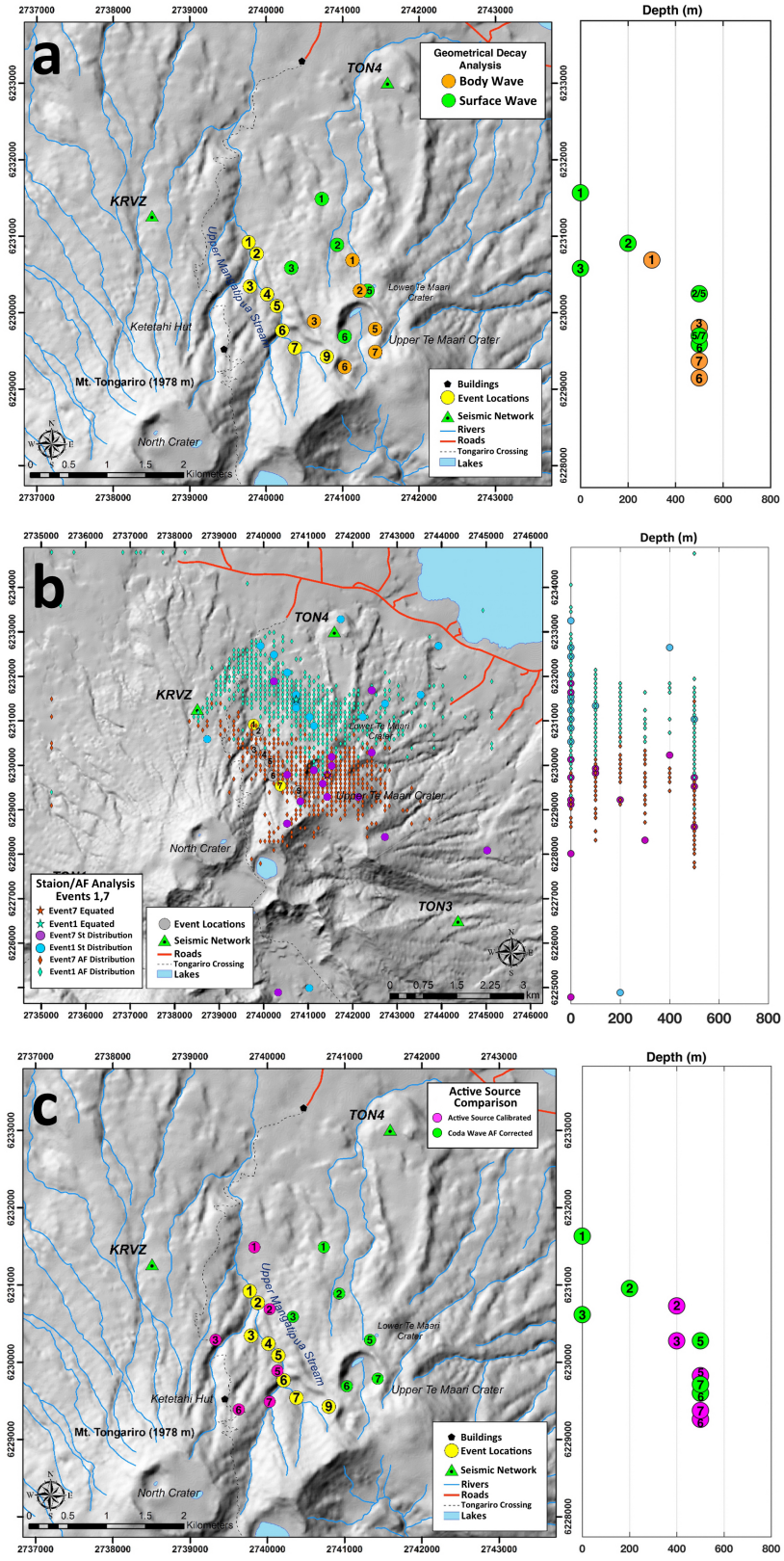


Figure 3.4 Analysis of the location effects for A) the body wave (orange) and surface wave (green) geometrical spreading. Sensitivity tests (B) relating to non-uniform station sets for event 1 (blue circles) and event 7 (purple circles) and the distribution of standard errors associated with AFs for event 1 (cyan diamonds) and event 7 (orange diamonds). Stars represent locations based on the mean AFs. (C) ASL results for AFs computed from the aggregate active source data (purple) compared to standard AF locations (green).

3.5 Conclusions

We completed the first calibration of an ASL method using active seismic sources at Tongariro National Park, New Zealand. The results suggest that location accuracies of ~1.0 km may be achieved with sparse networks <4 to 5 stations and reasonably constrained input parameters. Significant improvements in ASL accuracy would require inputs from other information sources, including calibration data from active sources. The application of AFs derived from regional earthquakes may hinder the location quality in some cases, and an error assessment via re-location of AF error distributions is recommended. Sensitivity tests for ASL input parameters show that attenuation and velocity have moderate influences on the location, but are easy to independently constrain. AFs are shown to strongly influence the location, and their application may introduce substantial location uncertainties.

CHAPTER 4: GEOPHYSICAL EXAMINATION OF THE 27 APRIL 2016 WHAKAARI/WHITE ISLAND, NEW ZEALAND ERUPTION AND ITS IMPLICATIONS FOR VENT PHYSIOGNOMIES AND ERUPTIVE DYNAMICS

Chapter Contents

4.1 Introduction……111
4.2 Data……117
4.2.1 Eruption history and background……117
4.3 Locating eruption sources using the amplitude source location method……118
4.4 Insights into eruption dynamics using infrasound……128
4.4.1 Source migration analysis……129
4.5 Analyzing the very long-period earthquake……135
4.6 Determining eruption pulse characteristics using the volcanic acoustic-seismic ratio……139
4.7 Discussions……144
4.8 Conclusions……148

This chapter is based on a paper in preparation.

Participating Authors:

Braden Walsh (Data processing, data analysis, manuscript development, manuscript writing and editing, discussions)

Jon Procter (Manuscript editing and discussion)

Ivan Lokmer (Data processing, data analysis, manuscript writing and discussion)

Johannes Thun (Data processing, data analysis, manuscript writing and discussion)

Tony Hurst (Discussions)

Arthur Jolly (Data processing, data analysis, manuscript writing and discussion)

CHAPTER 4: GEOPHYSICAL EXAMINATION OF THE 27 APRIL 2016 WHAKAARI/WHITE ISLAND, NEW ZEALAND ERUPTION AND ITS IMPLICATIONS FOR VENT PHYSIOGNOMIES AND ERUPTIVE DYNAMICS

4.1 Introduction

Whakaari Island (Maori for "The Dramatic Volcano") (Figure 4.1) is an active volcanic composite cone that lies at the northern end of the Taupō Volcanic Zone in the Bay of Plenty, New Zealand (Houghton and Nairn, 1991; Mayer et al., 2015). The island itself has a basal diameter of ~17 km, but only has about a 2 km diameter above the sea, and rises above sea level to ~320 m in elevation (Houghton and Nairn, 1991; Nishi et al., 1996). The horseshoe-shaped crater on Whakaari Island is a centrally located crater ~0.5 x 1.25 km in size and lies up to 10 m below sea level (Nishi et al., 1996). Periodically, the active crater fills up with a combination of seawater, rainwater and volcanic vapors, hiding the active vent location (Christenson et al., 2017).

The existence of water has given Whakaari many periods of continuous hydrothermal activity, with sporadic pheratic eruptions as well as phreatomagmatic and Strombolian eruptions (Nishi et al., 1996; Cole et al., 2000; Mayer et al., 2015). These eruptions are inferred to originate at shallow depths (<1.0 km) (i.e. Nishi et al., 1996; Jolly et al., 2017) due to the theorized location (0.5-2.0 km in depth) of the magma chamber in the upper crust (Houghton and Nairn, 1991; Cole et al., 2000; Werner et al., 2008). The hydrothermal activity sourced from these shallow depths are expressed on the surface during non-

eruptive periods as intense degassing fumaroles, mud bubbles, steaming ground, and hot springs (Houghton and Nairn, 1991; Heap et al., 2015).

The first seismometer (WIZ) was installed on Whakaari in 1976 and began recording many different types of earthquakes (Sherburn et al., 1998). In 2007 the seismic station was upgraded to a broadband sensor, but it was not until 2013 a second recording station (WSRZ) was installed. Furthermore, since 2011 Geological and Nuclear Sciences (GNS) has operated a varying number of seismic stations, which has lead to modern volcanic monitoring. Subsequently, ever since seismometers have been installed on the island, many have described in detail the different types of signals produced by the Whakaari volcanic system from: volcano tectonic (VT) events (Nishi et al., 1996), long-period (LP) events (Sherburn and Scott, 1993), very long-period (VLP) events (Jolly et al., 2017), and volcanic tremor (Sherburn et al., 1991).

A source location for an event is one of the most important parameters in hazard analysis. This significance has lead to the development and advancement of many source location techniques. Source location methods are typically divided up into four different categories depending on event type, recording network, and the properties of the recorded waveforms. Arrival time methods (i.e. Lee et al., 1972; Lahr, 1989) are mostly used for brittle rock failures that have well defined onsets, but may fail when signals are weak or if there are continually arriving excitations (i.e. tremor). Coherence methods (i.e. Neidell and Taner, 1971; Alemendros and Chouet, 2003) are very useful when waveforms are at low frequencies, but lack in

source location accuracy when locating higher frequency content or waveforms with large amounts of noise. The amplitude source location (ASL) method (i.e. Kanamori, 1993; Yamasato, 1997) is used for finding many different event source locations due to its ability to locate sources in areas where more traditional methods fail. ASL exploits the decay of the amplitude through geometrical spreading and attenuation of the waveform to estimate an original amplitude and source location. Furthermore, along with traditional ASL, recently the active source matching method has been able to determine source locations with great accuracy (e.g. Jolly et al., 2014A; Chapter 2). The method compares the decay characteristics of the active sources with that of the natural event, avoiding the need for site and path assumptions. The active source method lacks in the likelihood of having active source data at the research site and locating sources at depth.

This research uses a combination of both seismic and acoustic data to characterize the eruption sequence on April 27th 2016. Acoustic data is used to determine the precise timing of the eruption, along with eruption characteristics. Through the use of the ASL technique, eruption vents are located based on the calibration of ASL through active sources. Additionally, we describe and locate a VLP event during the eruption by using a waveform semblance approach. Finally, we integrate all the results together to form an eruption history of how the eruption sequence occurred.

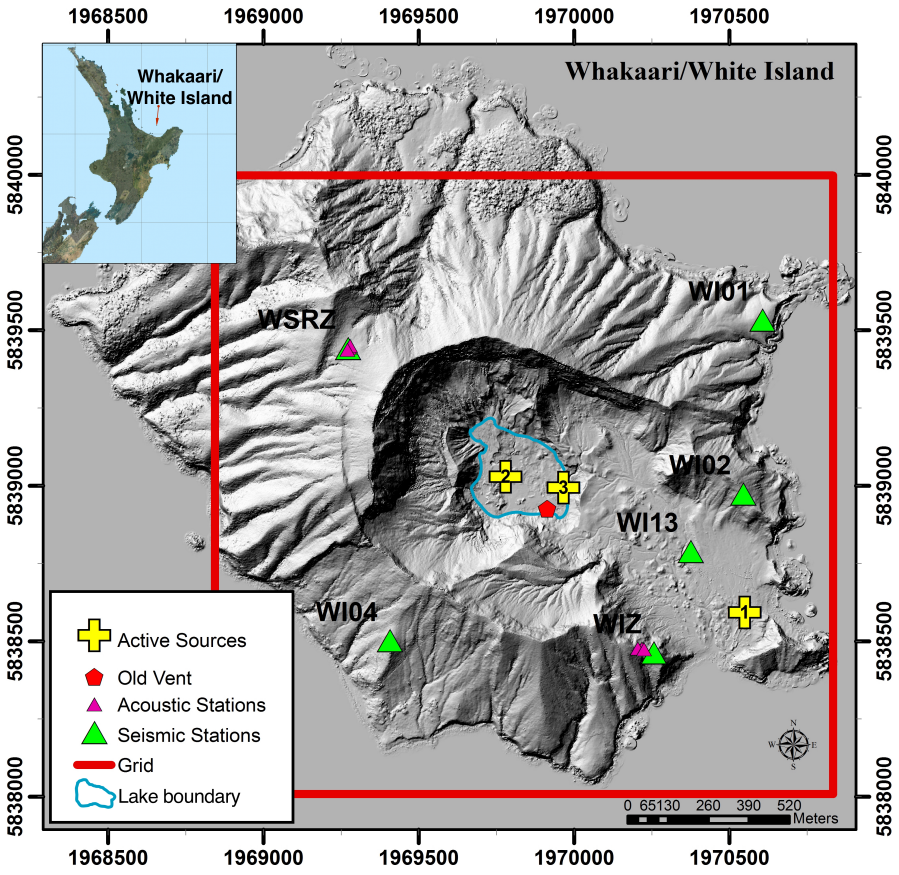


Figure 4.1 Map of Whakaari Island, New Zealand depicting the locations of seismometers (green triangles), acoustic sensors (magenta triangles), and active source drops (yellow crosses).

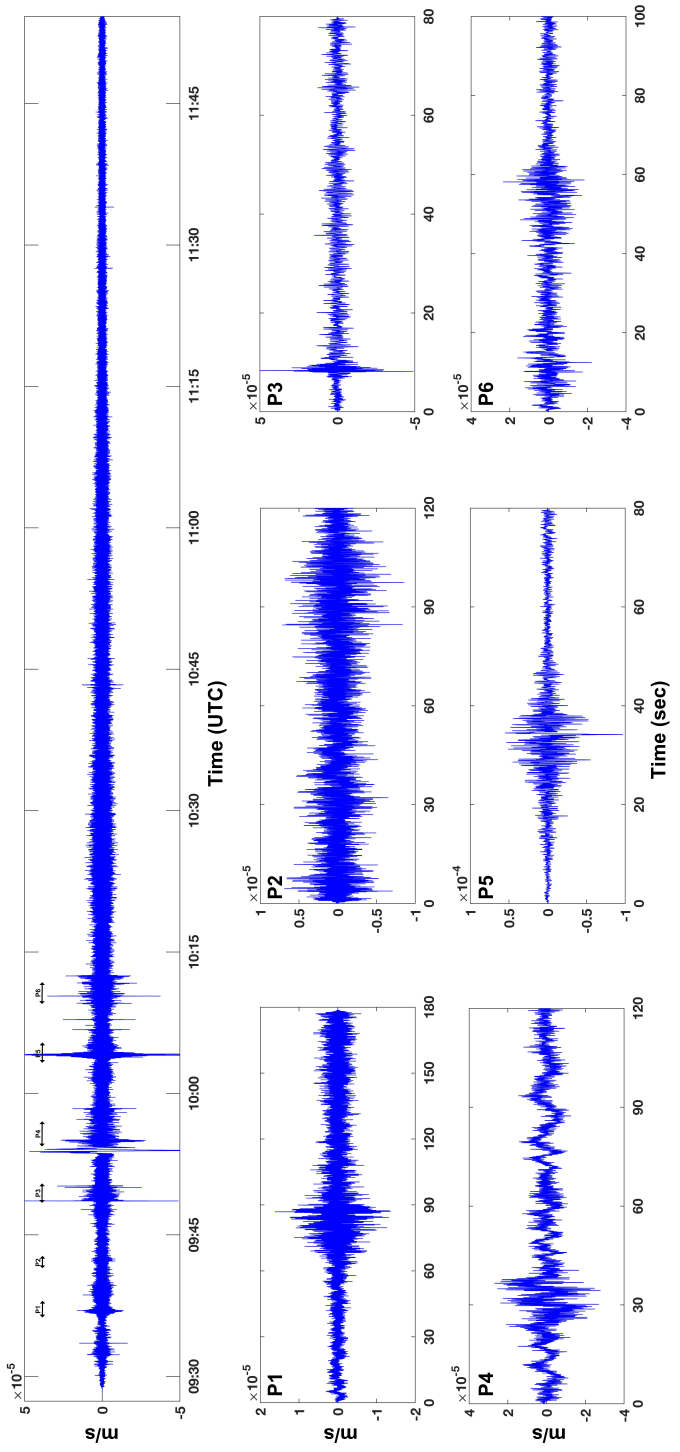


Figure 4.2 Seismic waveforms from station WIZ of the April 27th 2016 Whakaari eruption. Subfigures represent each of the eruptive pulses during the event.

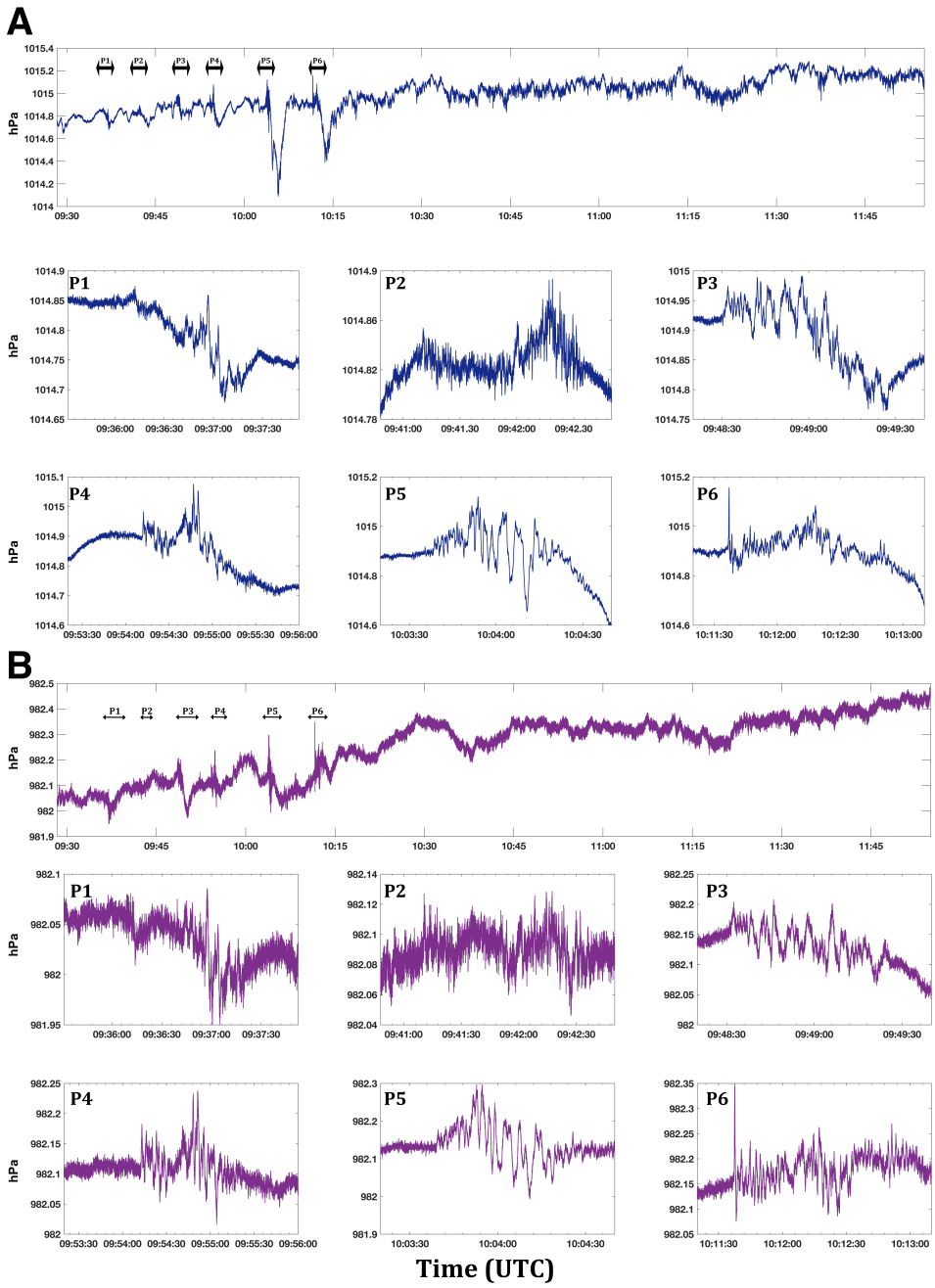


Figure 4.3 Acoustic waveform data from station WIZ (A) and WSRZ (B) of the April 27th 2016 Whakaari eruption. Subfigures represent each of the eruptive pulses during the event.

4.2 Data

During the April 2016 eruption there were two permanent *GeoNet* seismic stations (WIZ and WSRZ), along with four GNS Science seismic stations (WI01, WI02, WI04, and WI13). The *GeoNet* seismic stations consisted of Guralp 3ESP broadband seismometers with Quanterra Q330 digitizer. The GNS seismometers were composed of both Trillium compact seismometers and 24 bit Nanometrics Taurus digitizers. All six of the seismometers recorded at 120 s periods. Furthermore, sites WIZ and WSRZ contained three acoustic sensors, one Setra 270-600 pressure transducer with a sensitivity of 42 mV/Pa and two InfraBSU sensors. The acoustic sensors on Whakaari are set up in two sets of "L" shaped arrays, where the distances between sensors range between 5-15 m. Both seismic and acoustic instruments at every recording site sampled at 100 Hz.

4.2.1 Eruption history and background

On 27 April 2016 at ~09:30 UTC a moderate sized phreatic eruption occurred during the night, which ejected the entire crater lake water, along with a considerable amount of ash and debris that deposited on and around Whakaari. The eruption contained no juvenile material and only redeposited the crater floor material (Kilgour et al., 2018 in prep). Furthermore, Hamling (2017) noted that the eruption was preceded by a period of uplift. The eruptive plume reached a maximum height of 4.0 km and covered the whole island with dark yellow-green ash. The ash thickness was 5.0 mm at ~500 m from the eruption vent (Kilgour et al., 2018 in prep). Along with ash deposits, hot surge deposits were found along the

northern rim of the crater. The surge deposits are thought to have ejected horizontally since the deposits were only found on one side of large objects such as boulders (Kilgour et al., 2018 in prep). After the eruption, displacement rates on Whakaari increased by 300% due to the instability brought on by the lack of water in the crater lake and partially collapsing of the crater rim (Hamling, 2017).

The eruption event can be characterized as an eruptive period of up to six distinct pulses occurring over the first 30 minutes, and a late tremor period lasting up to two hours after the pulsing phase. Both seismic (Figure 4.2) and acoustic (Figure 4.3) sensors on the island were able to record these events. The eruptive pulses each lasted ~1-2 minutes in length and were separated on average of ~7.0 min apart. Additionally the seismic data recorded a VLP earthquake that preceded the forth eruptive pulse and the most energetic portion of the eruption at ~09:53 UTC.

4.3 Locating eruption sources using the amplitude source location method

The amplitude source location method uses the theory of seismic waves decaying with distance due to attenuation and geometrical spreading to estimate an original amplitude (Yamasato, 1997). Many since have used ASL to estimate locations from a variety of sources, such as: debris flows (Ogiso and Yamogida, 2015), lahars (Kumagai et al., 2009), pyroclastic flows (Yamasato, 1997), rockfalls (Aki and Ferrazzini, 2000), VT earthquakes (Kumagai et al., 2013), volcanic tremor (Ogiso et al., 2015), LP events (Battaglia and Aki, 2003), explosion events (Kumagai et al., 2011), and magma intrusions (Taisne et al., 2011).

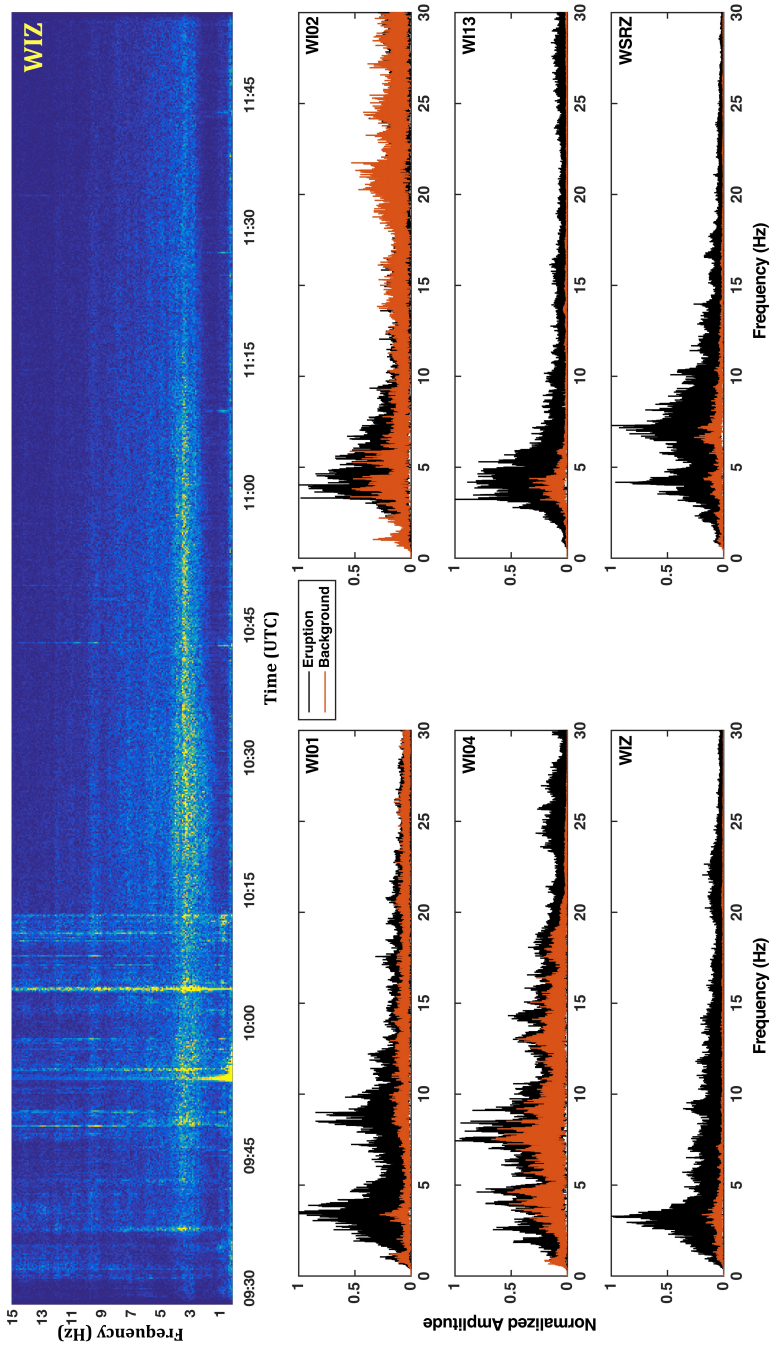


Figure 4.4 Seismic spectrogram for the eruption event (station WIZ) along with amplitude spectra for each of the seismic stations. The eruption spectra (black) are overlain by pre-event noise (blue) for background noise comparison.

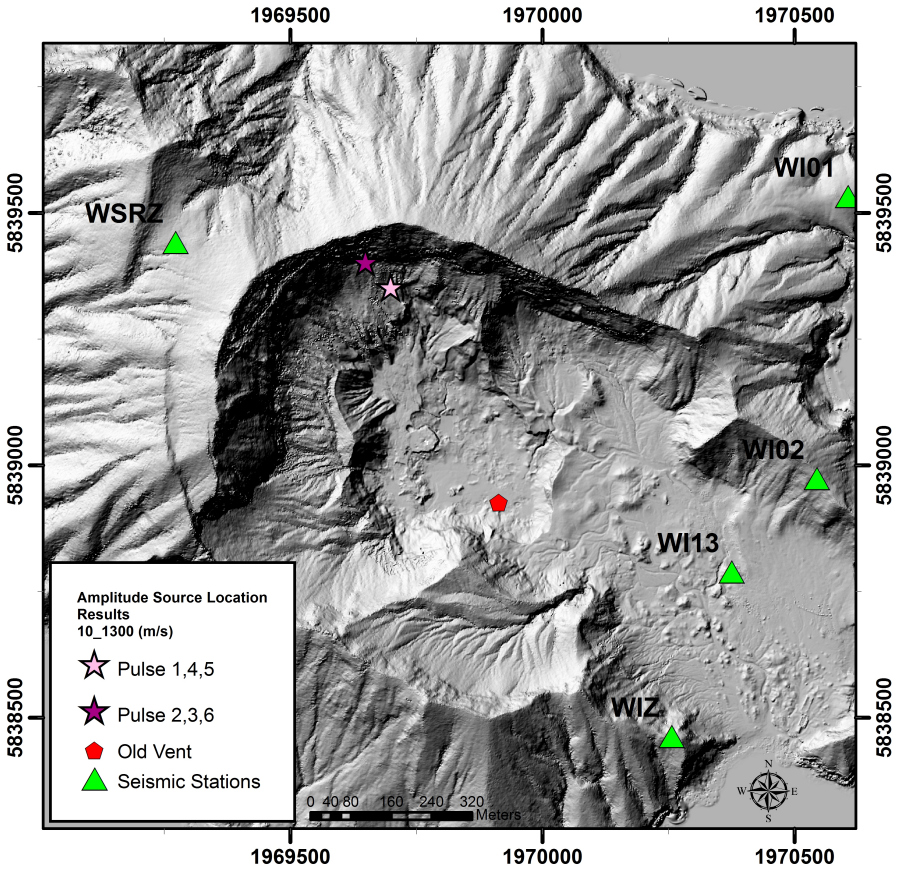


Figure 4.5 Minimal residual amplitude source location results (stars) using the base input values of β=1300 m/s and an attenuation value of Q=10.

Here we follow the method proposed by Battaglia and Aki (2003), which were among the first to apply ASL to volcanic processes and Walsh et al. (2017) to determine the locations of the six main eruptive pulses on April 27th 2016 Whakaari event. Seismic wave decay for a body wave is represented by:

$$A = A_0 \frac{e^{-B*r}}{r} * S \tag{4.1}$$

where A is the observed amplitude, r is the distance between the source and receiver, S is the site amplification correction, and B can be described as:

$$B = \frac{\pi f}{Q\beta} \tag{4.2}$$

where f is the average frequency of the signal, Q is the quality factor, and β is the average S-wave velocity. Rearranging equation (4.1) to solve for the original amplitude, we get:

$$A_0 = \frac{1}{N}\sum_{i=1}^{N} \frac{A_i}{S_i} r_i e^{Br_i} \tag{4.3}$$

where N is the total number of seismic station and i is a single station. Knowing both the observed amplitude and estimated original amplitudes; we can then calculate errors by determining normalized residuals by:

$$\text{Residual Error} \equiv \frac{\sum_{i=1}^{N}\left[A_i - A_0 \frac{e^{-Br_i}}{r_i}\right]^2}{\sum_{i=1}^{N} A_i^2} \tag{4.4}$$

To preform ASL, a grid search is used to estimate residual errors at many points. The grid point with the minimum residual error is used as the predicted ASL

location of the source. At Whakaari, the ASL grid is 2x2 km in area with 50 m grid spacing between points with surface elevation as zero depth for consideration of topography in the results.

For the ASL method to work, multiple input parameters are needed for using equations 4.1-4.4. First we note that for our location results, we do not calculate amplification factors. Others have shown at other locations amplification corrections actually do not improve location results, most notably on Tungurahua, Ecuador (Kumagai et al., 2015), Te Maari, New Zealand (Chapter 3), and Illgraben, Switzerland (Walter et al., 2017).

To determine eruption locations, the frequency range of 5-10 Hz was used, which is consistent with previous ASL research (e.g. Kumagai et al., 2015) and well within the peak energy range of the eruption (Figure 4.4). Baseline parameters for the ASL grid search include a S-wave velocity of 1300 m/s (Jolly et al., 2017) and an attenuation value of Q=10 (Jolly et al., 2012) for all subsequent analyses except where indicated.

Location results for the six pulses were obtained (Figure 4.5) from the vertical waveforms using the baseline input parameters. Stars represent the ASL minimal residual error location for a particular eruptive pulse. Lighter shades represent earlier pules and darker shades represent later arriving pulses. Pulses 1, 4, and 5 plot at the same location, as well as, pulses 2, 3, and 6 are altogether to the Northwest. The ASL locations are ~400-500 m off from the theorized vent location as well as, not locating in the crater lake. The lowest

residual locations instead plot up on the steep crater slope, thus more investigation needs to be conducted on input values in addition to site and path corrections.

To examine the input parameters on the ASL results, we next assess the sensitivity of the ASL method by changing the velocity and attenuation of the medium (Figure 4.6). For all of the pulses, the minimal residual error ASL location after sensitivity analysis changes up to a ~300 m difference. Increasing the attenuation value moves the minimal residual location to the Northwest, while decreasing the attenuation value moves the location to the Southwest toward the active crater. Increasing and decreasing the velocity input produces the same results displaying the theoretical trade-off between the two values shown in equation (4.2). Examining all six pulses, input values of Q=3 for the quality factor and a velocity of 1300 m/s show best locations compared to the theorized vent location. The very strong attenuation (Q=3) value used in obtaining improved results is consistent with Whakaari, shown by Jolly et al. (2012).

With the best predicted ASL results locating on average a couple hundred meters off from the estimated vent location, we next follow Chapter 3 by calibrating the ASL locations. Instead of calculating amplification factors, active source events (Jolly et al., 2012) are used to correct source and path effects. In 2011, three large ~700 kg bags of beach sand were dropped ~300-400 m above ground height. The first impact location was located by GPS, whereas the next two impact locations were located by triangulation. The sand bag impacts were recorded on 15 3-component broadband seismic stations on Whakaari. To process

the active source data, the impacts arrivals were picked, placed under a 1% Hanning taper, converted to velocity, and finally filtered between 5-10 Hz for the use with the natural data for the determination of station corrections on Whakaari (Table 4.1). Two of the three active source events landed in the active crater, with a third locating beyond station WI13 (Figure 4.1), and not centrally located. Subsequently, due to active source locations, we only use the two events that located in the crater to determine amplification factors.

After calibrating the ASL method from active source events on Whakaari, location estimates for eruptive pulses (Figure 4.7, green stars) locate on or close to the inferred vent location. The calibration of the ASL yielded a direct distance difference of ~300 m from the best located non-corrected results (Figure 4.7, pink stars). Likewise, the estimated calibrated pulse locations similarly locate together like the original results. Differing is the grouping of the pulses, where pulses 1, 4, and 5, and 2 and 6 are located together, with pulse 3 alone. The groupings may not have any significance because like the original results, the pulse locations are on adjacent grid points.

Table 4.1 Station corrections determined from active sources for 13 broadband seismometers that were installed during the active source experiment.

Station	Station Corrections	Standard Deviation
WI01	8.209	1.649
WI02	3.596	0.825
WI03	38.841	13.477
WI04	2.457	0.549
WI05	20.083	8.946
WI06	47.797	39.832
WI08	16.114	11.781
WI09	4.974	3.954
WI10	4.214	2.833
WI12	9.798	1.075
WI13	1.828	0.198
WI14	0.264	0.012
WI15	0.545	0.238
WIZ	1	NA
WSRZ	23.334	18.532

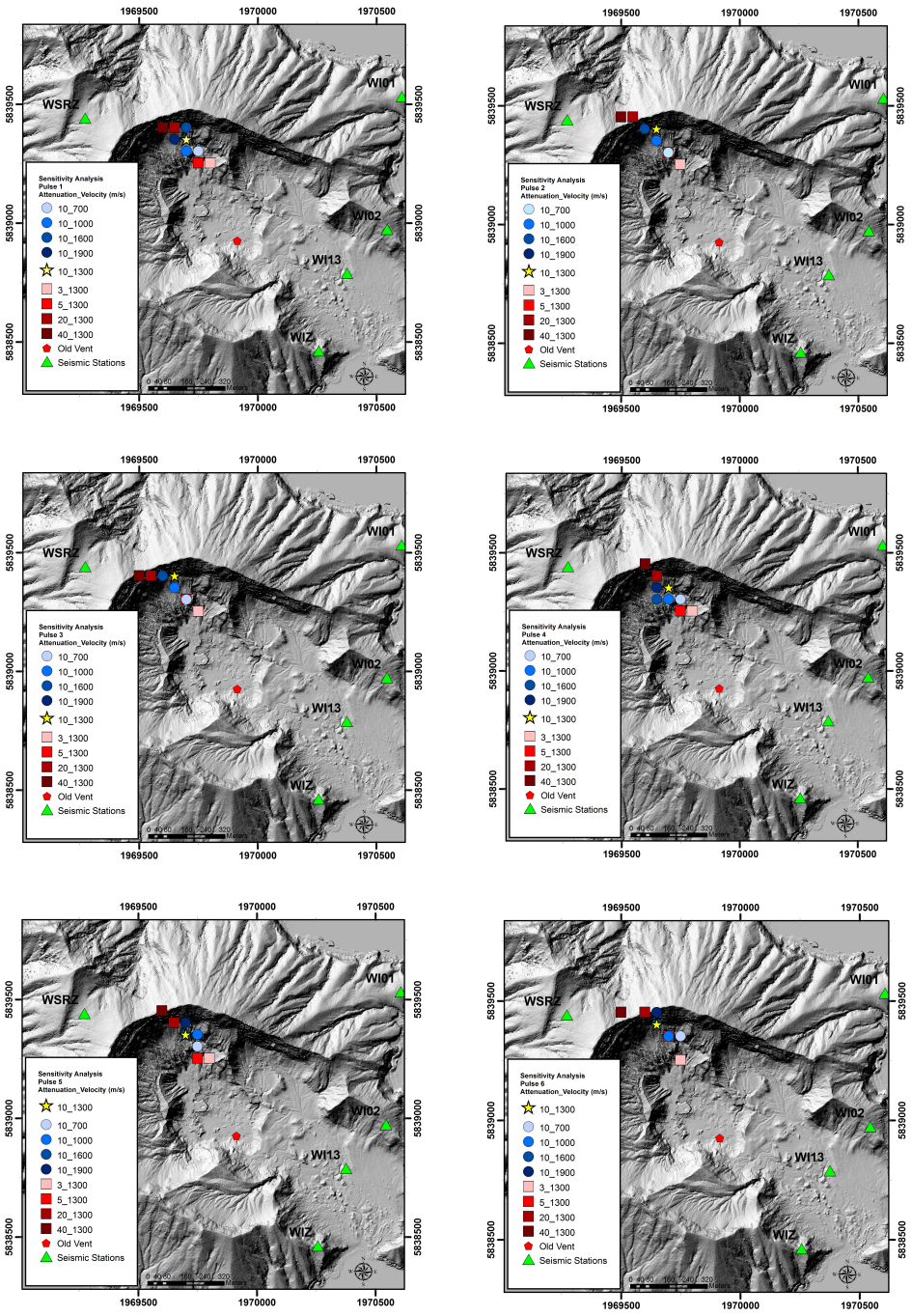


Figure 4.6 Amplitude source location results for each of the eruptive pulses with variable attenuation and velocity. The stars represent the base values of an attenuation of Q=10 and a body wave velocity of β=1300 m/s, while the attenuation is represented as squares and the velocity as circles.

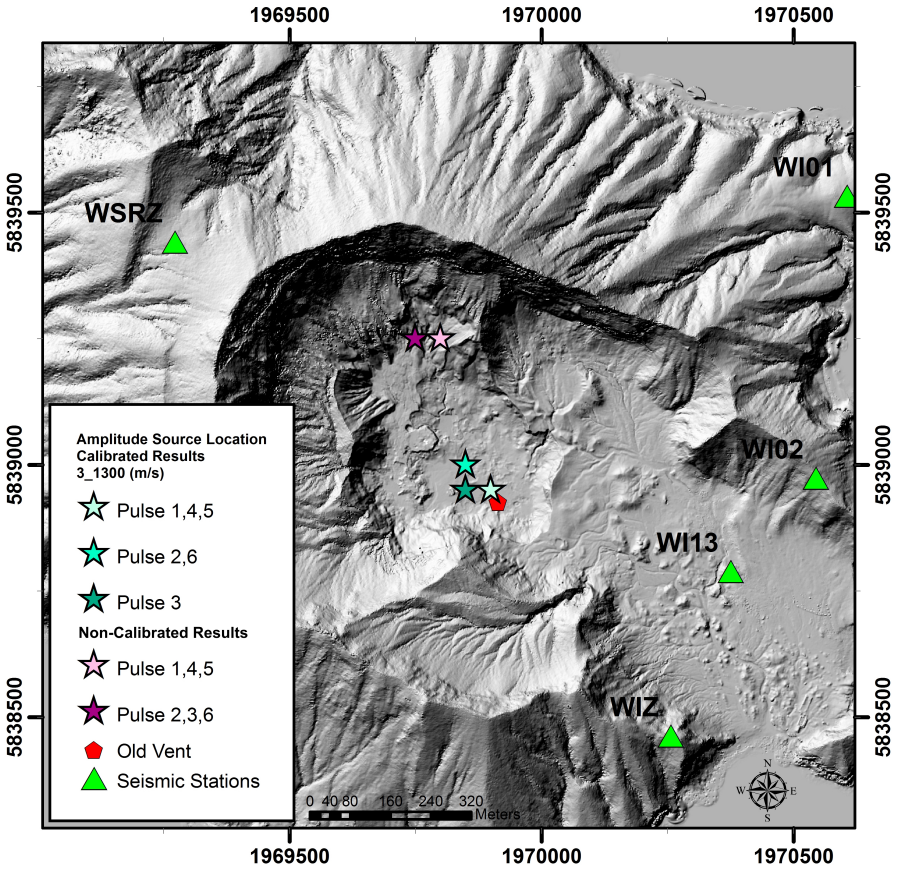


Figure 4.7 Calibrated amplitude source location results for each eruption pulse. Input values of an attenuation of Q=3 and a body wave velocity of β=1300 m/s were used to determine the locations of non-corrected results (pink stars) and active source corrected locations (green stars).

4.4 Insights into eruption dynamics using infrasound

To further the investigation the characteristics of the eruption, more specifically the individual eruptive pulses, we will next examine the acoustic waveform data. Acoustic data has been used for many years on and around volcanoes to understand eruptive behavior (i.e. Vergniolle and Brandeis, 1994; Yamasato, 1997; Johnson, 2003). Acoustic data from volcanoes is relatively easy to record because when a volcano erupts, it causes an increased pressure trace relative to the atmospheric background (Johnson, 2003). Additionally, acoustic signals given off by eruptions tend to be governed by frequencies below 10 Hz (i.e. Garces and McNutt, 1997; Ripepe and Marchetti, 2002; Jones et al., 2008).

Due to the fact that acoustic data is easier and simpler to use compared to seismics due to less assumptions for path effects, many have successfully used the data to locate volcanic sources. There are a variety of location techniques, most having to do with coherence amongst the signals (i.e. Ripepe and Marchettii, 2002; Johnson et al., 2006; Matoza et al., 2007). More specifically, Garces et al. 2003 used a progressive multichannel correlation method (PMCC) on Kilauea, Hawai'i, Johnson (2005) used cross-correlation (i.e. phase lag) to locate degassing vents on Stromboli, and Jolly et al. (2014B) used a back projection method on Te Maari, New Zealand.

4.4.1 Source migration analysis

Due to the dimensions of the acoustic sensor setup, traditional triangulation location method results are not the most reliable and accurate. The sensor spacing range of 5-15 m limits the range of frequency content that can be distinguished between each of the three sensors in the array. To this extent other location methods such as back projection cannot provide reliable results as well, due to the insignificant travel time variations. Therefore, with this instrumental set up, we stacked each recording station and observed time lags for each eruptive pulse (Figure 4.8). When overlaying both acoustic signals, station WIZ (blue) records the eruption onsets of each pulse first followed by WSRZ (red). Furthermore, the signals are highly variable in wavelength and frequency. To further investigate this phenomenon we look into the frequency content of each pulse by preforming source migration analysis (Figure 4.9) on each pulse at differing frequency bands (no filter, 0.1-0.2, 0.2-2 Hz) at 10 sec non-overlapping time windows (plotted sections). Additionally, figure 4.9 shows the pulse signal, peak frequency, and the correlation coefficient for each of the moving time windows. In the first panels (Figure 4.9), if a phase lag time window contains no data, this indicates times of non-explosion excitations or cycle skips within the acoustic signal. Like figure 4.8, figure 4.9 shows for the most part that station WIZ is the first arrival. Phase lag shifts to WSRZ only show up at lower frequencies (Figure 4.9B) and are not seen at frequencies above 0.2 Hz (Figure 4.9C). Furthermore, the best correlation between the two acoustics signals occurs at lower frequencies. When a reliable phase lag (under 1 sec) occurs, filtered data under 0.2 Hz illustrates highly correlated

coefficients. On the flip side, high frequencies (Figure 4.9C) have correlation coefficients that hover around zero, but can still show areas of high correlation when the phase lag is more near zero seconds. Comparing the phase lag to the correlation coefficient shows that the correlation increases when the phase lag tends to ~0-0.5 sec between the two signals. This indicates that when the phase lag increases beyond ~1.0 sec, the correlation decreases, and thus a timing or frequency contrast occurs.

These migration patterns could be due to many effects. Matoza et al. (2013) noted that acoustic wave frequencies from eruptions are variable due to high temperature jet like gasses that is expelled out of the vents at high velocities causing increased turbulence and friction. Another effect on frequency in the acoustic signal can come from scattering due to diffraction of the crater geometry or topography of the ground. Rowell et al. (2014) noted that reverberations from crater walls can cause signal interference, and cause timing delays in the data. At Whakaari, the current conduit/vent location is ~10 m below the main crater floor, and then there is an extra up to 300 m in elevation to the crater rim. Any acoustic signal coming from the vent location would not only have to travel out of the eruption crater, but up and over the larger crater rim to reach station WSRZ (Figure 4.1). The increased scattering in source migration time is most likely occurring from topographical affects. The explanation for the frequency contrasts in the eruptive pulses could be due to the type of eruption mechanism, and will be described further down.

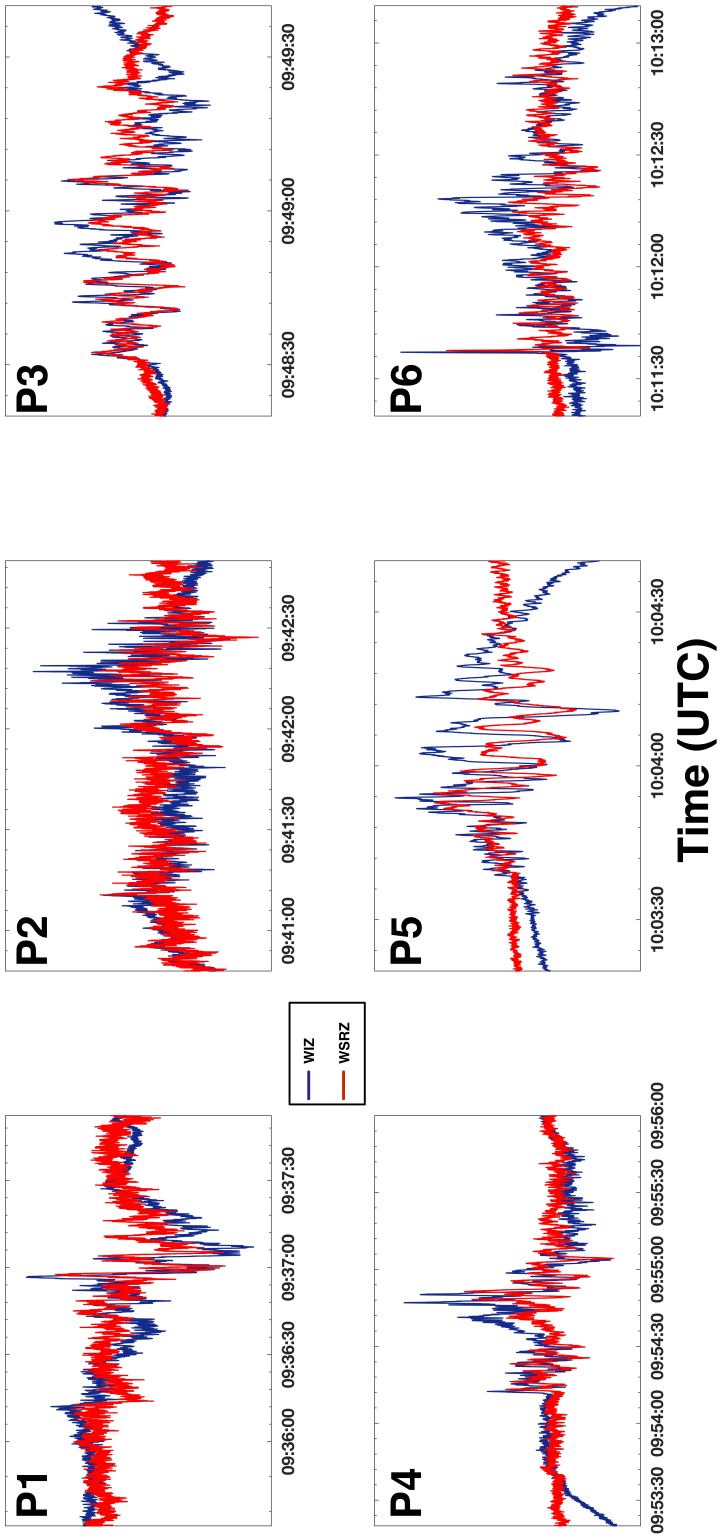


Figure 4.8 Acoustic signals for each eruptive pulse. Both WIZ (blue) and WSRZ (red) sensors are stacked and overlain at the same timing.

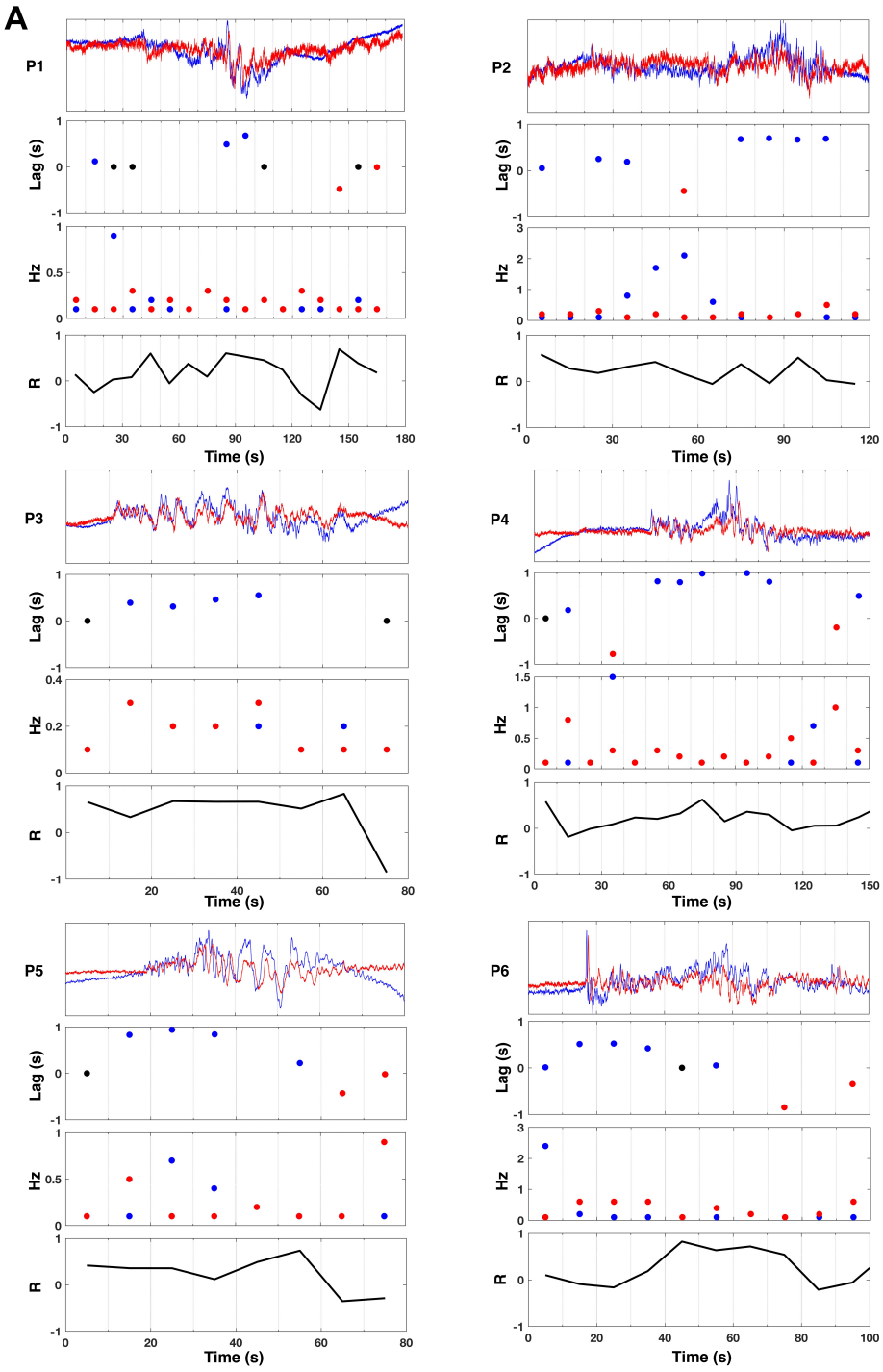


Figure 4.9 Source migration analysis figures (A) no filter, (B) 0.1-0.2 Hz, and (C) 0.2-2.0 Hz for the acoustic signals of both stations WIZ (blue) and WSRZ (red) for each eruptive pulse. Each subfigure contains the acoustigram, phase lag, peak frequency, and correlation coefficient values between the two stations.

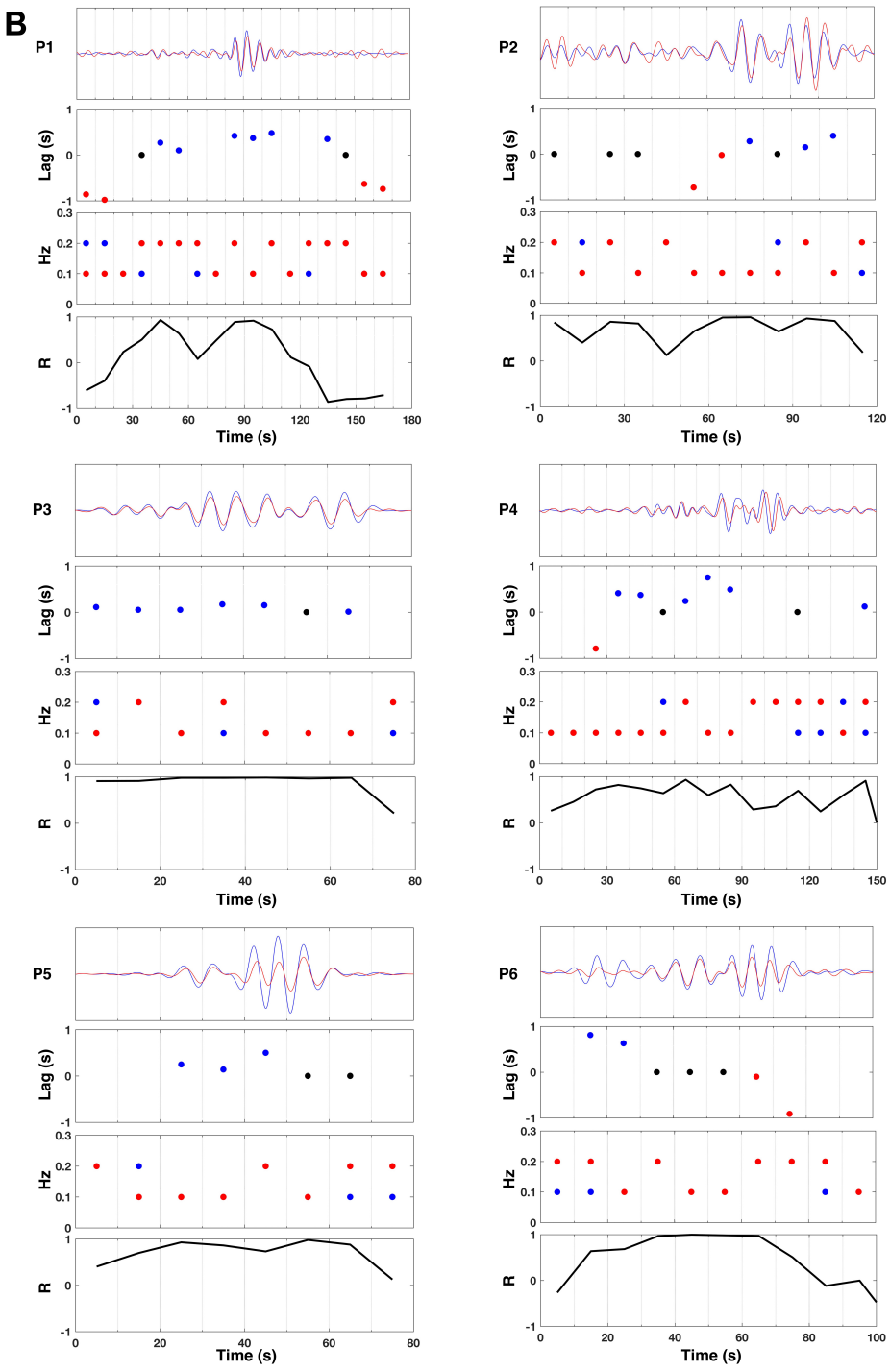


Figure 4.9 Continued.

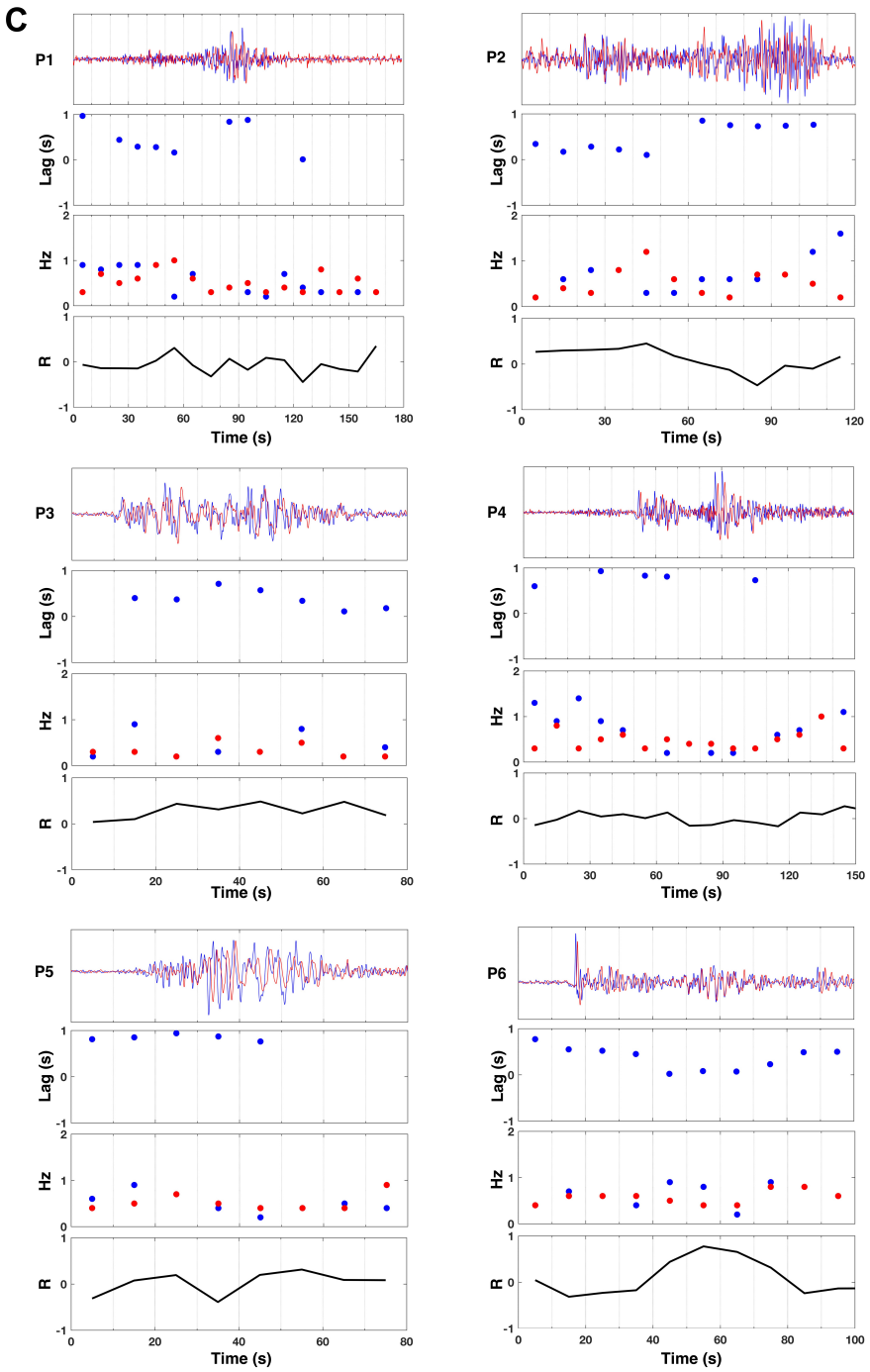


Figure 4.9 Continued.

4.5 Analyzing the very long-period earthquake

We used the waveform semblance as described in Kawakastu et al. (2000) for the analysis of the VLP during the April 27th eruption. The eruption sequence was recorded on a subset of seismic stations that were also utilized for a VLP swarm occurring in August 2011 (Jolly et al., 2017). From Kawakatsu et al. (2000), coherency amongst seismograms can be characterized using:

$$S = \sum_{j=1}^{L}\left(\sum_{i=1}^{N} u_{i,j(i)}\right)^2 / N \sum_{j=1}^{L}\sum_{i=1}^{N} u_{i,j(i)}^2 \qquad (4.5)$$

where L is the length of the seismogram, N is the number of stations and $u_{i,j(i)} \equiv u_i(t_i + j\Delta t)$ is a seismogram of the ith station at the $j(i)$th time sample at the start time t_i.

For a stationary isotropically radiating point-source seismic waves will propagate as compressive body waves that may be rectified into a linear particle motion (Kawakatsu et. al, 2000). In the radial component (the direction of a station from the source) the seismogram particle motion is given by $u_{i,j(i)} \equiv R_{i,j(i)}$. Differences in the multi-station travel-times are accommodated with adjustments for these time delays (t_i), which should improve the radial waveform coherence. The mutually perpendicular components $H_{i,j(i)}$ and $V_{i,j(i)}$ for an isotropic radiating source, should have negligible contributions. In this case, the waveform semblance (Kawakatsu et al., 2000) may be applied to emphasize the radial excitation from the isotropic source and penalize departures from rectilinear behavior via the following equation:

$$S_3 = \frac{1}{D}\sum_{j=1}^{L}\left\{\left(\sum_{i=1}^{N} R_{i,j(i)}\right)^2 - N\left(\sum_{i=1}^{N} V_{i,j(i)}^2\right) - N\left(\sum_{i=1}^{N} H_{i,j(i)}^2\right)\right\} \quad (4.6)$$

where *V* is the component in the direction perpendicular to *R* within the vertical plane, which contains both source and receiver, and *H* is in the horizontal component perpendicular to both *R* and *V* (*V* may not be vertical). *L* is the number of time samples and *N* is the number of stations. We take the scaling factor *D* as:

$$D = N\sum_{j=1}^{L}\sum_{i=1}^{N} R_{i,j(i)}^2 \quad (4.7)$$

S_3 measures the rectilinearity of particle motion pointing via the signal coherency in the radial direction. As in Kawakatsu et al. (2000) we normalize each seismogram so that the RMS amplitude of each signal at each station becomes unity:

$$RMS_i^2 = \frac{1}{L}\sum_{j=1}^{L}(R_{i,j(i)}^2 + V_{i,j(i)}^2 + H_{i,j(i)}^2) = 1 \quad (4.8)$$

which removes the amplitude information from the original seismograms giving equal weight to each station during the coherence computation.

As for the prior analysis (Jolly et al., 2017), we compute the waveform semblance within a grid search of the target volume. We searched over a 2.0 km grid centered on the crater lake and from sea level to 3.0 km below sea level at 100 m grid spacing. At each grid point we compute the source to station distance, azimuth and incidence angle, as well as, rotate the *E*, *N*, *Z* seismograms for each station into *R*, *H* and *V* components having an appropriate travel-time-delay based on the independently determined velocity model (Jolly et al., 2017). Results are

normalized using Equation (4.5) and the waveform semblance is computed with Equation (4.6). After determining the best fit semblance in the coarse grid search, we re-computed the semblance within a 20 m grid spacing within a 200x200x200 m search volume centered on the best fit coarse solution. The validity of the waveform semblance was confirmed via location of synthetic examples as outlined in Jolly et al. (2017).

The waveform semblance computation used in this chapter was rigorously tested using both synthetic waveform data and a swarm of 25 VLP events that occurred at Whakaari Island in August 2011 (Jolly et al., 2017). The synthetic tests incorporated uncertainties in velocity structure and source geometry, and monitored departures between the computed and retrieved locations. The synthetic tests allowed uncertainties for the 2011 swarm to be robustly assessed and were about +/- 200 m both laterally and in depth. The VLP observed before the fourth eruptive pulse (Figures 4.2 and 4.3), is located (Figure 4.10) within the same location distribution found for the 2011 earthquakes and has similar location uncertainties (Table 4.2).

Table 4.2 Summary of semblance location for VLP event 2016-04-27 09:53:30 UTC filtered between 0.02 to 0.125 Hz. The location is in meters based on New Zealand Map Grid coordinates in meters. The lateral and depth (er_l (z)) error estimates are in meters based on 20% error limit from the maximum semblance.

Easting (m)	Northing (m)	Depth (m)	Er_1 (z)	Semblance	S/N
2880000+200	6400100+150	1000	800-1200	0.8473	3.9882

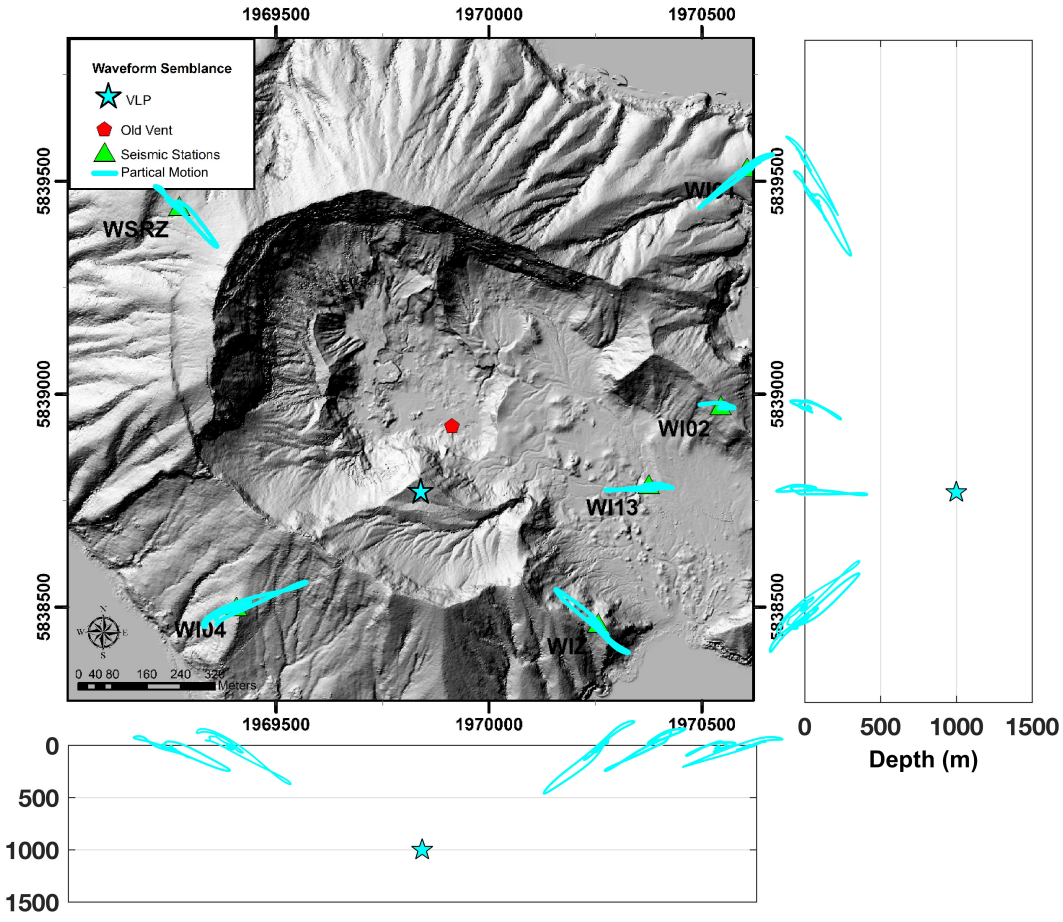


Figure 4.10 Map of particle motions based on waveform semblance for the VLP event during the eruption sequence, a blue star represents the best-fit location.

4.6 Determining eruption pulse characteristics using the volcanic acoustic-seismic ratio

The volcanic acoustic seismic ratio (VASR) is the ratio between the acoustic energy and the seismic energy of an eruption or eruption sequence. VASR was first popularized by Johnson and Aster (2005) on Karymsky, Russia and Erebus, Antartica, and later used on Redoubt Volcano, Alaska (McNutt et al., 2013), Te Maari, New Zealand (Jolly et al., 2014B), and at Tungurahua, Ecuador (Palacios et al., 2016). We use VASR on the Whakaari eruption sequence as a means to partition the energy between the ground and atmosphere to determine eruption source characteristics, as well as, other differences between the multiple pulses (i.e. energy transfer, conduit size, and source area). Johnson and Aster (2005) outlined varying situations for values of VASR, where a low VASR may indicate a large source region, long narrow conduit, and/or a high density plume. Additionally, if the VASR has a high value, the source region may be small, have a short/wide conduit and/or have a low density plume.

To determine the VASR, both seismic and acoustic energies need to be estimated. To estimate the acoustic energy of an eruption and assuming that the source is a monopole, the total acoustic energy as depicted by Johnson and Aster (2005) as:

$$E_{Acoustic} = \frac{2\pi r^2}{\rho_A c_A} \int \Delta P(t)^2 dt \quad (4.9)$$

where r is the source to station distance, ρ_A is the air density, c_A is the air wave velocity and ΔP is the pressure. For the use at Whakaari, we use a ρ_A= 1.204 kg/m^3 and an air velocity (c_A) of 330 m/s. Determining the seismic energy of the eruptive pulses in terms of body waves can be shown through Boatwright (1980) and Johnson and Aster (2005) by:

$$E_{Seismic} = 2\pi r^2 \rho c \frac{1}{A} \int S^2 U(t)^2 dt \quad (4.10)$$

where ρ is the density of the ground, c is the seismic medium velocity, S is the site response, U is the seismic amplitude and A is the intrinsic attenuation term and can be described as:

$$A = e^{\frac{-\pi f r}{cQ}} \quad (4.11)$$

where f is the average frequency and Q is the quality factor. Estimating seismic energies, values of ρ=2000 kg/m^3 and c=2200 m/s were used for Whakaari.

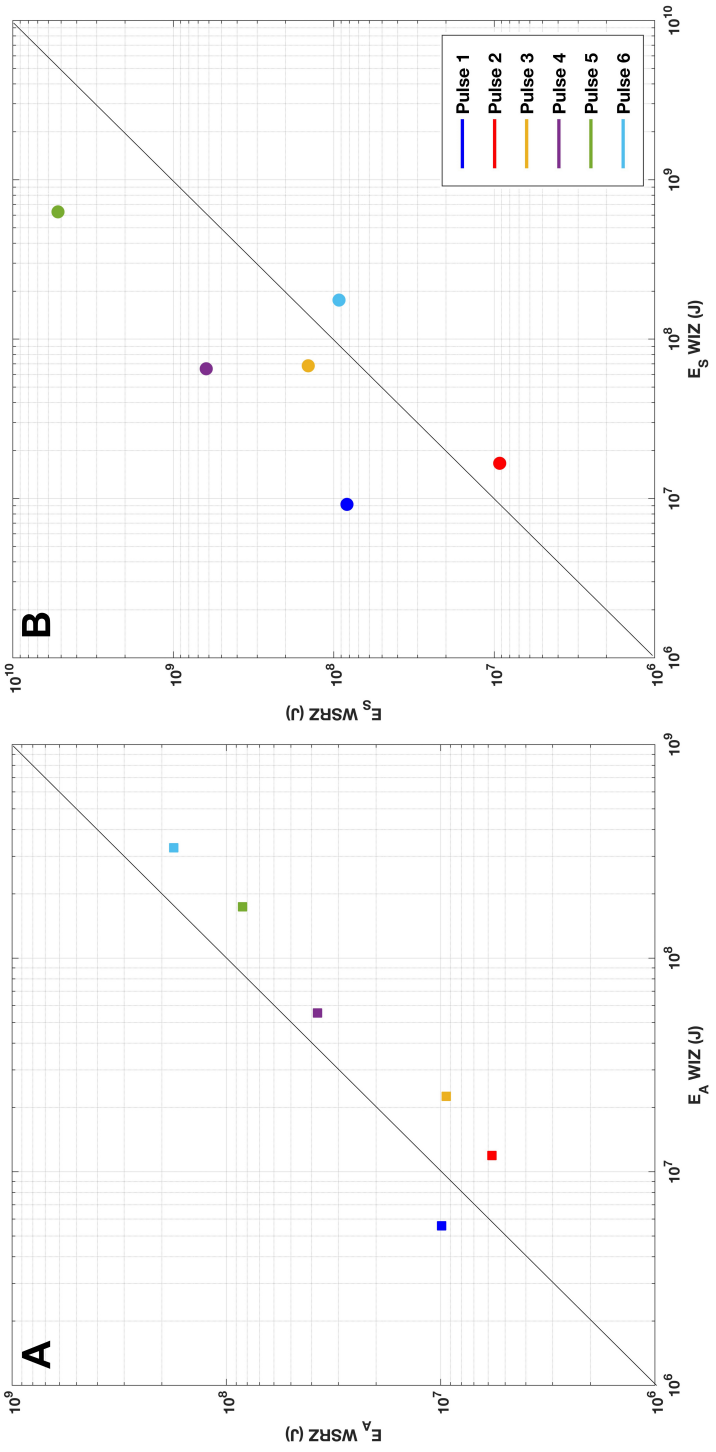


Figure 4.11 Energy partitioning between stations WIZ and WSRZ for acoustic data (A) and seismic data (B). The colors of the points represent the different eruptive pulses.

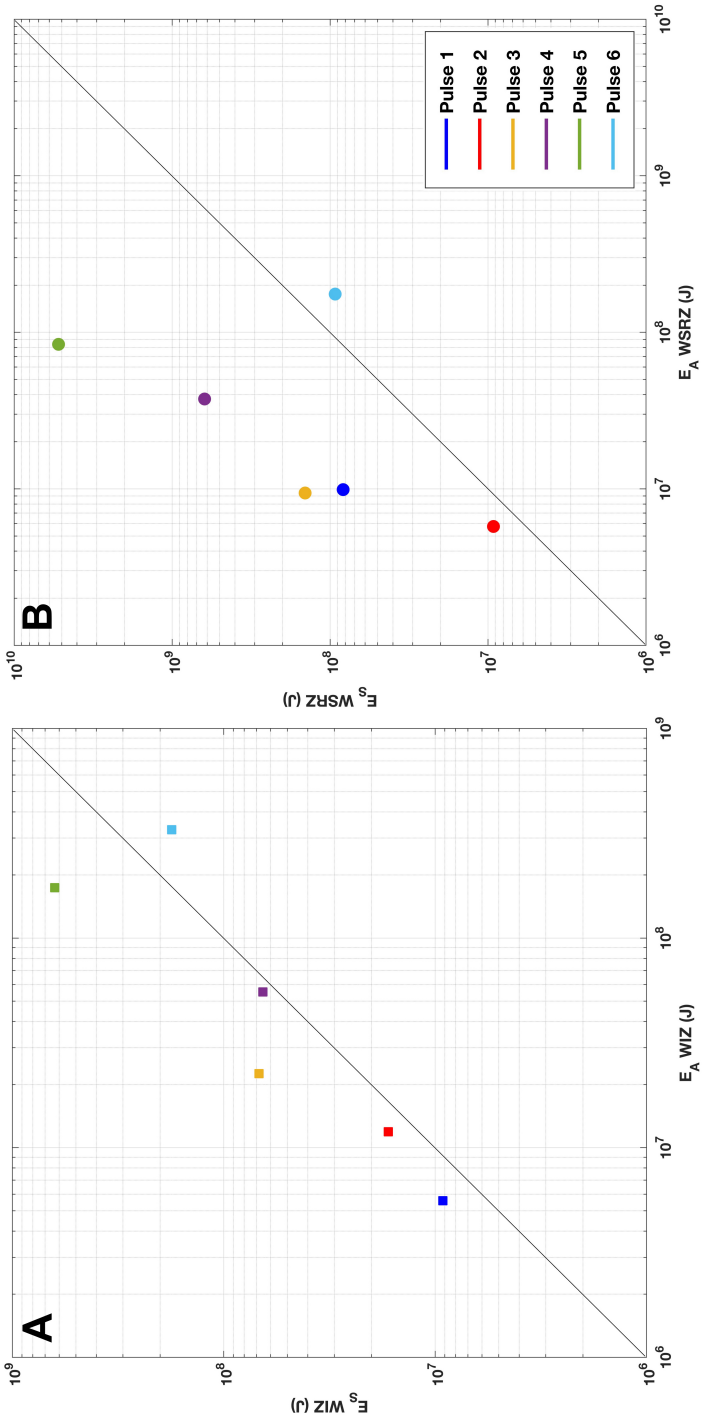


Figure 4.12 VASRs between stations WIZ and WSRZ for all six eruptive pulses for acoustic data (A) and seismic data (B).

Due to possible directional variations amongst the network array, we compare the energies for both acoustic and seismic data at both stations (Figure 4.11). The VASR data for both data sets were filtered between 0.5-10 Hz to obtain peak energy content from both sources of data. The acoustic partitioning (Figure 4.11A) between WIZ and WSRZ show a stable correlation, with station WIZ recording slightly higher energies, which is expected due to station location. As for the seismic energy, the partitioning (Figure 4.11B) shows a relatively even energy distribution, but the eruptions tend to have stronger signals for station WSRZ. This could be due to vent location, but is more likely a geological medium effect or an effect from the source radiation directionality of each pulse. Since our signals contain data below 5.0 Hz we may have near source scattering effects as noted by Takemura et al. (2009). However, we surmise that the variations would be minimal, in the determination for VASR partitioning.

Next, we estimate the ratio of the amount of energy that is transferred through the air compared to the ground by the VASR represented by:

$$\eta = \frac{E_{Acoustic}}{E_{Seismic}} \tag{4.12}$$

These values can be exemplified visually by plotting the acoustic and seismic energies for each pulse against each other (Figure 4.12). Station WIZ (Figure 4.12A) depicts greater energies for all the pulses, except for pulse 6, which has higher acoustic energy. Furthermore, for station WSRZ (Figure 4.12B) the veer toward the seismic energy is greater than for WIZ. We also note that for both stations pulse 6 is the only eruption to be stronger in acoustic energy than in

seismic energy. Additionally, pulse 5 for both sensors has the most seismic energy. The significance of the differences in terms of the whole eruption setting and process in acoustic and seismic energy or VASR value will be discussed in detail below in the discussions section.

4.7 Discussions

On April 27th 2016 at approximately 09:30 UTC Whakaari produced a phreatic eruption generating six distinct eruptive pulses of hot gas and older crater material. Accumulating all the data from the eruption, we thus create an eruption history and method of causation. The waveform semblance method constructed a VLP depth of ~1.0 km depth, which occurred 50 s before pulse 4 and accompanying acoustic wave onset (Figure 4.13). Due to the timing and the depth of the VLP, we take to the theory pointed out by Jolly et al. (2017) where a gas slug rises up from depth through a preexisting crack. The gas slug then reaches the surface and bubble bursts or explodes creating the eruptive pulse in the signals. Additionally, the acoustic data (Figure 4.3) contains a pressure drop or down pressure indicating the presence of a buoyant ash cloud rising up after the initial eruption.

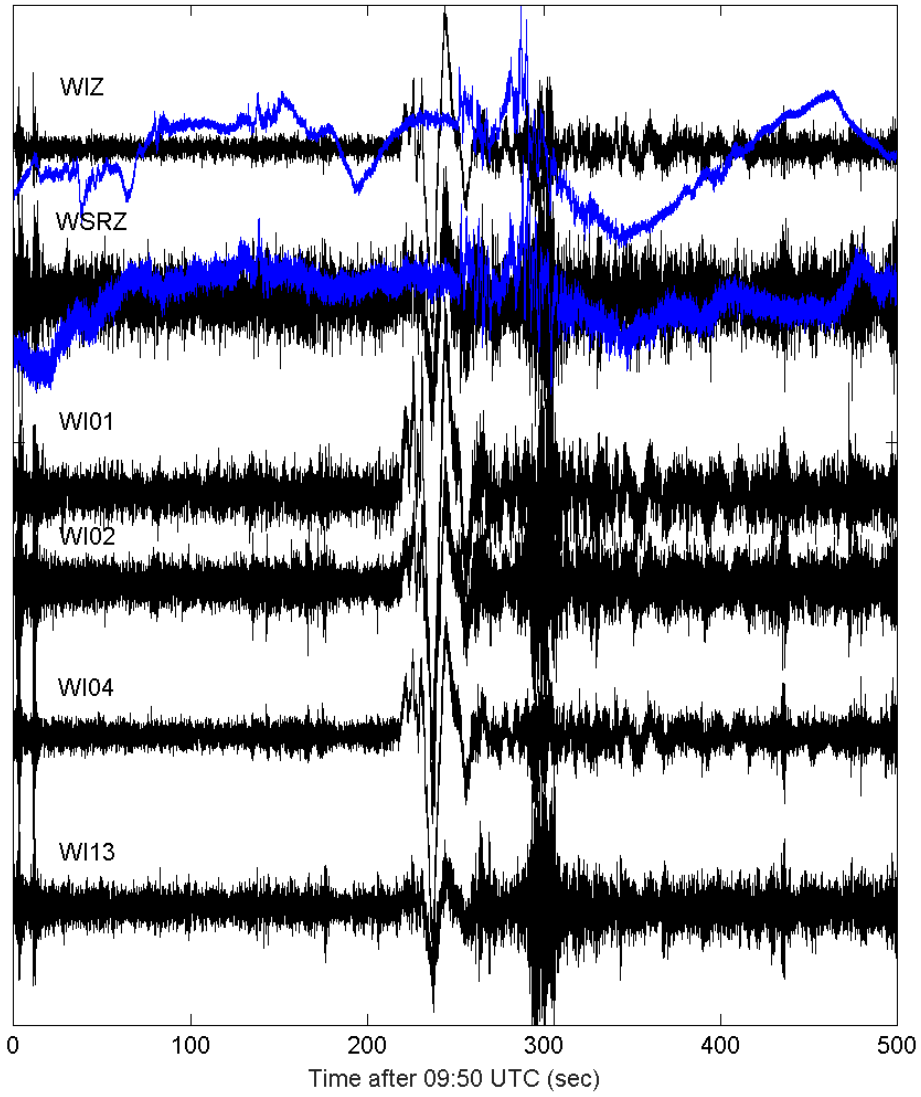


Figure 4.13 Eruption waveforms for all recording stations for both seismic (black) and acoustic (blue) data depicting the VLP event and the fourth eruptive pulse. Notice the differences in onsets (~50 s) of the VLP on the seismic waveform compared to the eruption onset on the acoustic waveform.

The varying frequency levels in the acoustic signals can help describe vent characteristics. While changing frequencies can be caused by turbulence from the eruptive gases (Woulff and McGetchin, 1976), the changes can also be caused by eruption dynamics. There are two leading theories that combine with the idea of gas slugs rising up from depth. First, the frequency contrasts could be due to multiple explosions at once (e.g. Ripepe et al., 1993; Taddeucci et al., 2012) where there is a large slug burst followed immediately by smaller bubbles erupting. The second theory explains the difference in frequencies by changing the flux of the gas slug (e.g. Goto et al., 2014). Here multiple gas slugs of varying sizes move up the preexisting crack, which creates the variations in the frequency content of each pulse.

Additionally, along with the variations in acoustic frequency, there are also variations within each eruptive pulse in the phase lag between the two stations (Figure 4.10). The phase lag change switching from the two stations could represent eruptive bursts from multiple vents or source locations, or as noted by Matoza et al. (2013) could be jet turbulence excitations or eddies at different altitudes and jet axis angles in the eruption column.

The seismic results show that there could be two or three different vents, but at the same time considering the propinquity to each other, the pulses could have easily came from a single vent. Analyzing the acoustic data also shows that when the signals are highly correlated the phase lag between the two stations is ~-0.1-0.5 seconds, indicating that the eruption most likely has come from an area

of multiple vents instead of just one district main vent. Additionally, ASL source locations for all the pulses lie within 100 m of the previous vent location and within 30 m of the post eruption depressions on the crater floor, theorized to be the location of the new vent (Figure 4.14). Looking further into the acoustic phase lag data (Figure 4.9), pulses 1, 4, and 5 tend to have larger phase lags than that of pulses 2 and 6, when the correlation coefficient is near 1, indicating that pulses 1, 4, 5 were closer to station WIZ than pulses 2 and 6. This suggests that the seismic data through ASL compares very well with the acoustic source migration results, because of the similar groupings in eruptive pulses, and the locations for pulses 1, 4, 5 to be closer to WIZ and pulses 2 and 6 to be more central located between the stations.

To determine eruption dynamics we looked at the partitioning between the acoustic and seismic energies for each eruptive pulse. A VASR value can mean many different things in terms of the eruptive processes. Johnson and Aster (2005) have detailed four different possibilities for a high or low VASR. A Low VASR could mean a large source region, a deep source, high density plume, or a high impedance lava lake, and visa versa for a high VASR. Looking at the VASRs for the April 27th eruption and averaging both recording stations, pulses 1, 4, and 5 have low VASR values compared to pulses 2 and 6. Considering just the most energetic eruptions, this could very well mean that pulses 4 and 5 came from a deeper source region then pulse 6. We take to the theory of depth differences in terms of VASR difference, because the seismic signals (Figure 4.2) show pulses 1, 4, and 5 with distinct heightened traces compared to the signal of the other eruptive pulses.

Additionally, if we combine the vent location information from both ASL and source migration analyses, the results match up with the VASR values, in which we can consider the vent for pulses 1, 4, and 5 source from a deeper crack (~1.0 km from semblance interpretation) than that of pulses 2 and 6.

4.8 Conclusions

At approximately 09:30 UTC on April 27th 2016, a phreatic eruption occurred on Whakkaari Island producing six major eruptive pulses. Seismic and acoustic data was collected and eruption vent locations were determined through the use of ASL with the seismic data and source migration analysis with the acoustic data. Vent locations for the eruptive pulses were found to have come from two to three different locations, where pulses 1, 4, and 5 and pulses 2 and 6 located from the same vent. These locations compare well with the VASR analysis conducted to determine eruption dynamics. The VASR analysis showed that pulse 5 contained more seismic energy, and that pulse 6 had stronger acoustic strength then the rest of the pulses. This indicated that pulse 5 came from a deeper source location than pulse 6. Through the use of semblance and a VLP event that occurred before pulse 4, it was determined that the VLP source was ~1.0 km below the surface. In concluding, we take to the theory that pulses 1, 4, and 5, erupting from one vent, and pulses 2 and 6 erupting from another, with eruption pulses gradually increasing in strength with time, where pulses 1, 4, and 5 came from a deeper source (~ 1.0 km) than pulses 2 and 6.

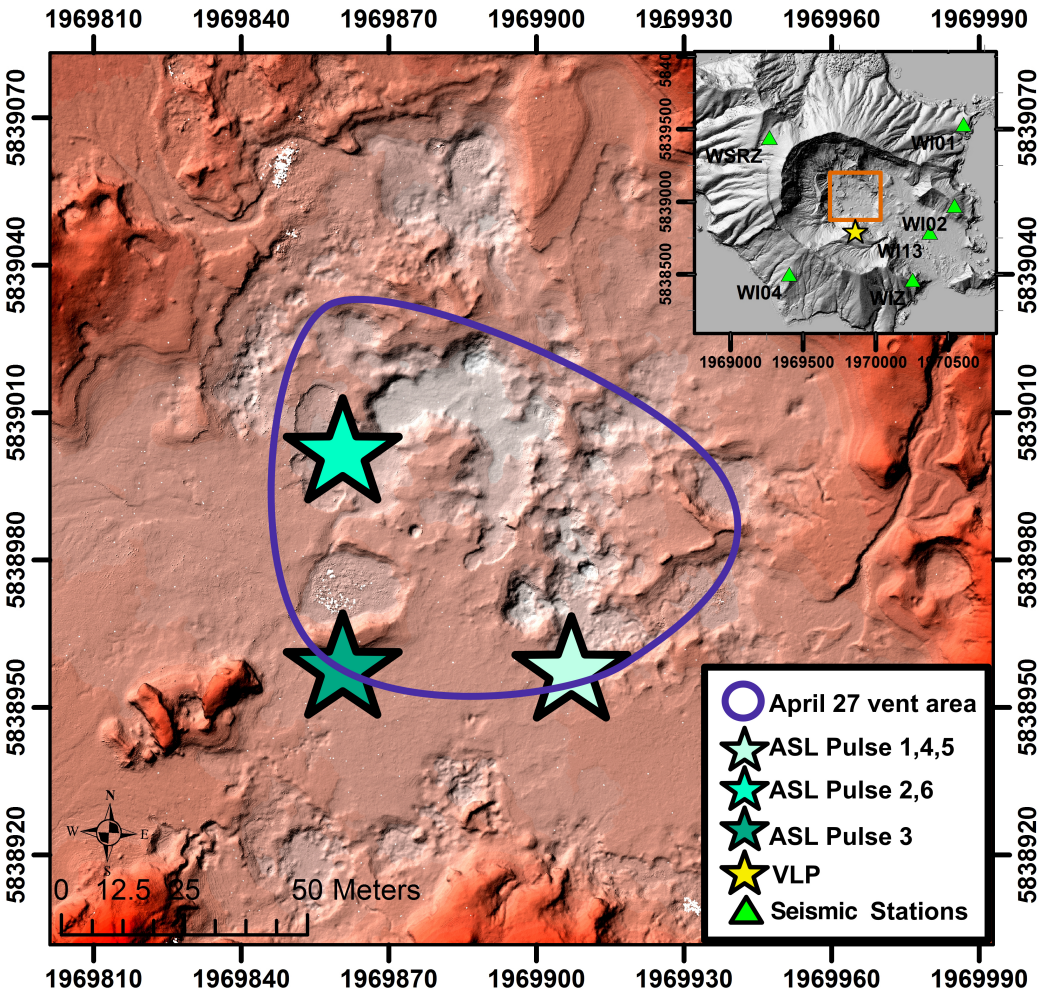


Figure 4.14 Post eruption imagery from Whakaari crater area. Green stars represent ASL locations for the six pulses, yellow star represents location of the VLP, and the purple circle represents the theorized April 27th eruption vent area.

CHAPTER 5: IMPROVING SEISMIC SOURCE LOCATIONS THROUGH THE AMPLITUDE SOURCE LOCATION (ASL) METHOD USING 3-COMPONENT ANALYSIS: AN EXAMPLE FROM TE MAARI VOLCANO, TONGARIRO NATIONAL PARK, NEW ZEALAND

Chapter Contents

5.1 Introduction.....152
5.2 Data.....154
5.3 Methods.....157
5.3.1 Amplification factors.....158
5.3.2 Grid search.....161
5.4 Results.....161
5.5 Component analysis.....168
5.6 Discussions.....173
5.6.1 Estimating locations for 3-componetn ASL using H/V ratios to correct site response.....176
5.7 Conclusions.....183

CHAPTER 5: IMPROVING SEISMIC SOURCE LOCATIONS THORUGH THE AMPLITUDE SOURCE LOCATION (ASL) METHOD USING 3-COMPONENT ANALYSIS: AN EXAMPLE FROM TE MAARI VOLCANO, TONGARIRO NATIONAL PARK, NEW ZEALAND

5.1. Introduction

The amplitude source location (ASL) method has become one of the most common seismic techniques for locating sources in volcanic regions. Many different events have been successfully located with this method, for example, pyroclastic flows (Yamasato, 1997), debris flows (Ogiso and Yomogita, 2015), lahars (Kumagai et al., 2009) Volcano-tectonic (VT) earthquakes (Kumagai et al., 2013), LP events (Battaglia and Aki, 2003), and seismic tremor (Ogiso and Yomogita, 2012). ASL is different from other source location methods due to the fact there is no need for distinct arrivals. Location methods, such as the phase arrival and need such arrivals to calculate time differences in the phase arrivals (Kao and Shan, 2004). Waveform coherence methods can be difficult to use as well because they lack in source location accuracy when locating higher frequency content or waveforms with large amounts of noise (Alemedros and Chouet, 2003). This can be very difficult in volcanic settings because of the large number of heterogeneities in the geological medium (Jolly et al., 2014B).

The ASL method is ideal in volcanic terrains due to it only using the decay of seismic waves and not needing impulsive onsets or the difference in arrival times (Kanamori, 1993; Yamasato, 1997). Although distinct arrivals do not need to be

known for the ASL method to work, ASL does require assumptions from the *a priori* data (velocity and attenuation models) (Chapter 3). Along with geological medium models, ASL also needs to be corrected for site conditions. To solve this, amplification factors are used because seismic amplitudes recorded at seismic stations in a network are individually affected by local site conditions (Kumagai et al., 2009).

Chapter 3 noted that there are problems with how amplification factors (AFs) are calculated, and that AFs do not always work. This has been seen on Tungurahua, Ecuador (Kumagai et al, 2015) and Te Maari, New Zealand (Walsh et al., 2017), where standard errors can be up to ±900 m on the surface and ±230 m in depth. To improve on these errors, we calculated AFs, as well as source locations, using a combination of all three components of the seismic stations. We hypothesized that by adding additional station components, we may be able to achieve minimal residuals closer to true location.

The theory behind using all three components originates from geological engineering, where in most cases amplification factors are calculated in both the vertical and horizontal directions. Engineers must consider all three directions of earthquake motion to build durable structures that will withstand any and all phases of an earthquake. Celebi (1991) notes that on many occasions peak accelerations are higher in the horizontal plane. This kind of seismic response usually occurs for site effects due to the geology and/or the topography of the station location (Spudich et al., 1996). Recently using all three components has

become standard in the study of volcanic mass flow events. Many such studies have shown that the energy released from sources is stronger in non-vertical directions, i.e. landslides (Surinach et al., 2005), VT earthquakes (Tsuruga et al., 1997), snow-slurry lahars (Cole et al., 2009), snow avalanches (Kogelnig et al., 2011), and hyperconcentrated flows (Chapter 2).

5.2. Data

To determine if using all three components of the seismic station reduces ASL location errors, we used actives sources on Te Maari volcano in Tongariro National Park, New Zealand (Figure 5.1). The active sources were recorded in February 2013 (Jolly et al., 2014C) when 1000 kg bags of sand were dropped from a helicopter approximately 1000 m above the topography. In total there were eleven drop attempts, eight of which were successful producing seismic impulses up to ~6.0 km. We here use six active sources because Chapter 3 noted that only six of the events produced enough quality data to use with the ASL method. The active seismic sources have kinetic energies ranging between $7x10^6$ and $9x10^6$ Nm. To process the active source data P-wave arrivals were picked and the instrument response was deconvolved. Next amplitude spectra were calculated with a sampling window of 1024 s and a 256 sample cosine taper.

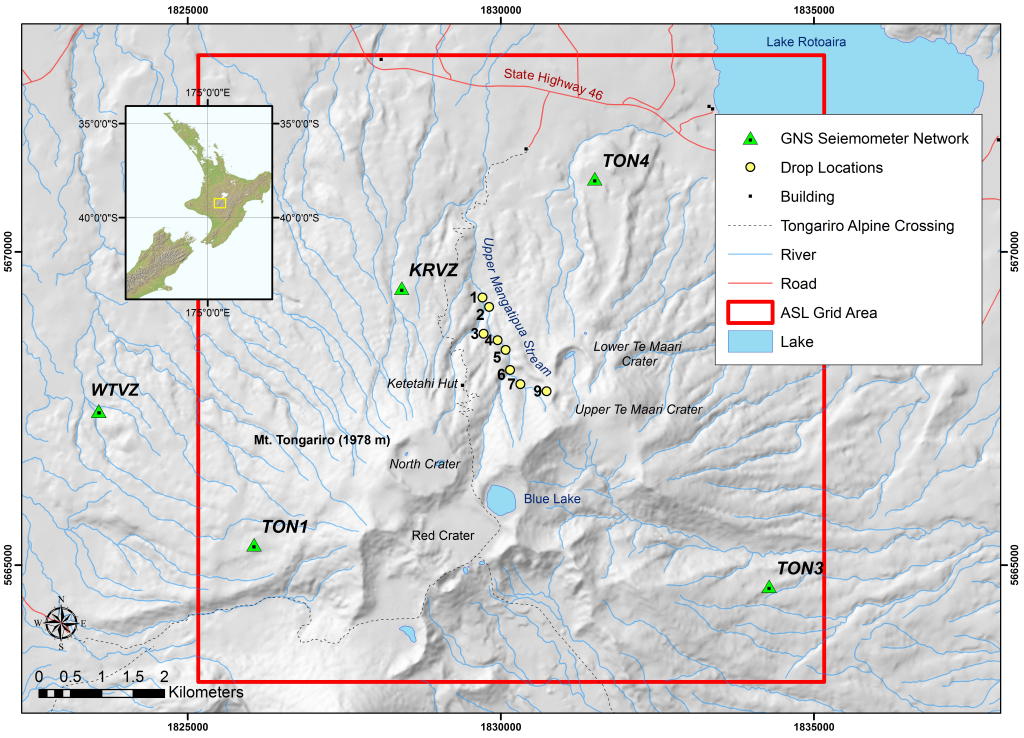


Figure 5.1 Location of study area, northern section of the Tongariro National Park, New Zealand. Yellow circles represent the active source event locations along the Te Maari debris flow channel.

During the active source experiment, each event was recorded on five 3-component broadband seismic stations (KRVZ, WTVZ, TON1, TON3, TON4) in Tongariro National Park. All five seismic stations used 24-bit digitizers with 100 Hz sampling and local GPS time stamps. Stations included Guralp 6T sensors except for station KRVZ and WTVZ, which used short period Sercel L4C3D sensors.

Figure 5.2 shows the example spectra for six of the events in all three station components. Events (1,2,3) lower down the channel have stronger spectral amplitudes for stations KRVZ and TON4, whereas active source events higher up the debris flow channel have more uniform spectral amplitudes across the five seismic station array. Overall the spectra show an increase in amplitude in the East and North components over the vertical component. Stations KRVZ and TON4 produce the highest spectral amplitudes for all the events in every component except for the event 6 vertical component where TON1 has the maximum amplitude. Mid-channel events prefer the North component, whereas the upper channel events along with event 1 produce more energy in the East component.

5.3 Methods

ASL is based on the theory that seismic amplitudes decay while traveling through a geological medium. The decay of the amplitude is due to two main factors, the attenuation and the geometric spreading of the seismic waves (Jolly et al., 2002). Following the methodology of Chapter3, the decay in amplitude of a surface wave may be shown as:

$$A = A_0 \frac{e^{-B*d}}{\sqrt{d}} * AF \tag{5.1}$$

where *A* is the observed amplitude, *d* is the distance between the source and receiver, and *AF* is the amplification factor correction. The "*B*" in equation (5.1) is the *a priori* information and equates to:

$$B = \frac{\pi f}{Q\beta} \tag{5.2}$$

where *f* is the average of the chosen frequency range, *Q* is the quality factor, and β is the average seismic velocity. After AFs are applied to correct site and path effects, equation (5.1) becomes:

$$A_0 = \frac{1}{N} \sum_{i=1}^{N} A_i \sqrt{d_i} e^{Bd_i} \tag{5.3}$$

where N is the number of seismic stations and *i* represents one station. Combining recorded amplitudes with estimated predicted amplitudes allows errors to be calculated from normalized residuals for each assumed source location:

$$Residual\ Error \equiv \frac{\sum_{i=1}^{N} \left[\square_i - A_0 \frac{e^{-Bd_i}}{\sqrt{d_i}} \right]^2}{\sum_{i=1}^{N} A_i^2} \tag{5.4}$$

5.3.1 Amplification Factors

In complex regions, such as volcanic areas, site amplification can greatly differ from station to station due to the amount of heterogeneity in the geological subsurface (Mayeda et al., 1991). To resolve site amplification, Aki and Chouet (1975) first worked on the idea of using coda waves from regional earthquakes to calculate amplification factors. The coda method needs no prior knowledge of the ground properties because coda waves are an averaging of the subsurface through which they travel removing all direct propagational effects of local earthquakes (Aki and Chouet, 1975; Phillips and Aki, 1986).

Calculating AFs from equation 5.1 (*AF*), we use the coda wave normalization method implemented by Chapter 3, which is based on the approach of Phillips and Aki (1986). Coda wave normalization requires the extraction of coda waves from several well-spaced regional earthquakes. The starting time for a coda wave has been defined as two times the difference between the origin and S-wave arrival times (Aki and Ferrazzini, 2000). From the starting time of the coda wave, three 10.0 s time windows with 5.0 s overlaps were withdrawn from the earthquake seismograms and root mean squared amplitudes were calculated. Adding quality control, we next used a 10 s time window before the P-wave arrival, which was used for the signal-to-noise ratio (SNR) calculation. Time windows that fell below a SNR ≥ 2 were removed. Finally, each time window from each seismic station was divided by the reference station.

Station	KRVZE	KRVZN	KRVZZ	TON1E	TON1N	TON1Z	TON3E	TON3N	TON3Z	TON4E	TON4N	TON4Z
Method 1	2.0107	2.3879	0.8645	2.3032	2.1063	1	1.2747	1.9119	0.7878	1.7468	1.3819	0.7819
SD	1.2698	1.1743	0.3412	0.7824	0.7844	NA	0.4959	0.7742	0.2303	0.9497	0.3985	0.1297
Method 2	0.7904	1.0047	0.8645	1	1	1	0.5168	0.797	0.7878	0.7555	0.6615	0.7819
SD	0.2479	0.3982	0.3412	NA	NA	NA	0.1616	0.2446	0.2303	0.3734	0.1666	0.1297
Station	NGZE	NGZN	NGZZ	OTZVE	OTZVN	OTZVZ	WTVZE	WTVZN	WTVZZ			
Method1	1.6517	1.6661	1.3566	0.8483	0.9693	1.456	1.7608	2.3042	1.3479			
SD	1.1747	0.9901	0.9544	0.3872	0.4197	0.8269	0.714	0.9398	0.752			
Method 2	0.7764	0.836	1.3566	0.3382	0.4533	1.456	0.878	0.9053	1.3479			
SD	0.4643	0.5452	0.9544	0.1122	0.2446	0.8269	0.453	0.1666	0.752			

Table 5.1
Amplification Factors

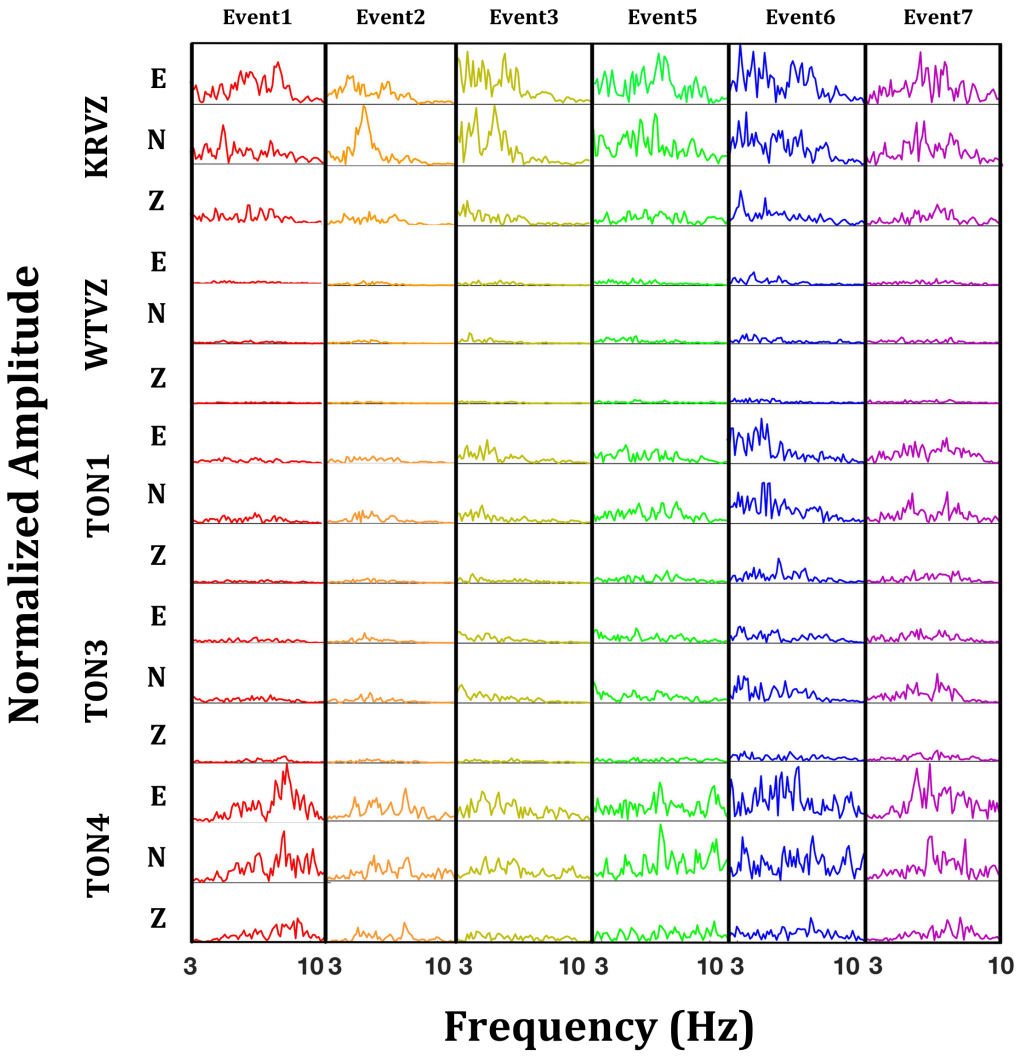


Figure 5.2 Seismic spectra for all of the active source drops for each station component. Normalization is to the maximum amplitude of each component for each station.

5.3.2 Grid Search

Locating seismic sources using equation 5.4 requires the use of a grid search to determine the minimal residual, resulting in an estimated source location. The grid Chapter 3 where a 10x10x2 km volume grid was implemented around the Upper Te Maari debris flow channel centered on the 2012 ephemeral lake and event location 6 (Walsh et al., 2016). The 200 km volume has a grid spacing resolution of 100 m between grid points, and spacing at depth uses surface elevation as zero to follow the natural topography. Exploiting equation 5.4, a best-fit location was estimated for each active seismic source, and then was compared to the true known location of each active source event for analysis.

5.4 Results

Stable residual minimum locations for the grid search were obtained when the following input parameters for Tongariro were used: an attenuation value of Q=60 (Titzschkau et al., 2010), a velocity model of 1500 m/s (Jolly et al., 2014C) for surface waves, and a frequency band between 3-10 Hz. 3-10 Hz was chosen because the active source data having peak frequencies in the range and is consistent with similar ASL studies.

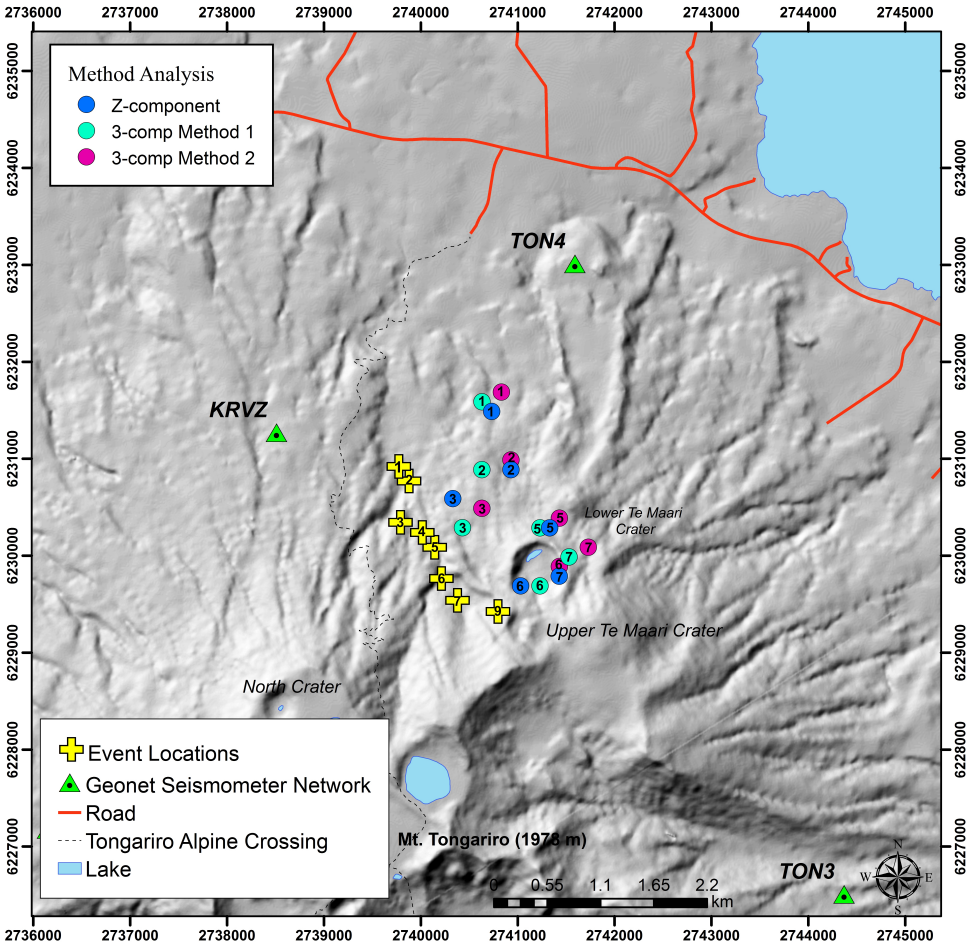


Figure 5.3 ASL minimal residual location results for the vertical component (blue), 3-component amplification factor method 1 (teal), and 3-component method 2 (magenta).

Completing ASL location results for the vertical component and both AF methods (Figure 5.3), we obtain true distance average errors of ~1.03 km, 1.01 km, and 1.25 km for vertical, method 1, and method 2 respectively. Between using all the components together to estimate AFs (magenta circles) and estimating AFs by separating the seismic components (teal circles), we achieve better ASL results by separating the components and using each TON1 component as the reference station, hence further analyses will only use AFs calculated using method 1. Comparing these results to the standard technique of using the vertical component (blue circles), method 1 locations are about the same with a standard error of ±0.15 km on the surface and ±70m in depth.

In order to further compare the 3-component results with the vertical component results, we set up analyses similar to Chapter 3, with tests of relocating the events by using different seismic station configurations, as well as sensitivity examination of AF uncertainties. For these analyses, we only present here results for events 1 and 7 for clarity. Event 1, which is lowest down the debris flow channel, should present results for sources in the lower topography and be less centralized in the seismic setup. Event 7 will provide results that are in the middle of the station array and near the volcanic crater.

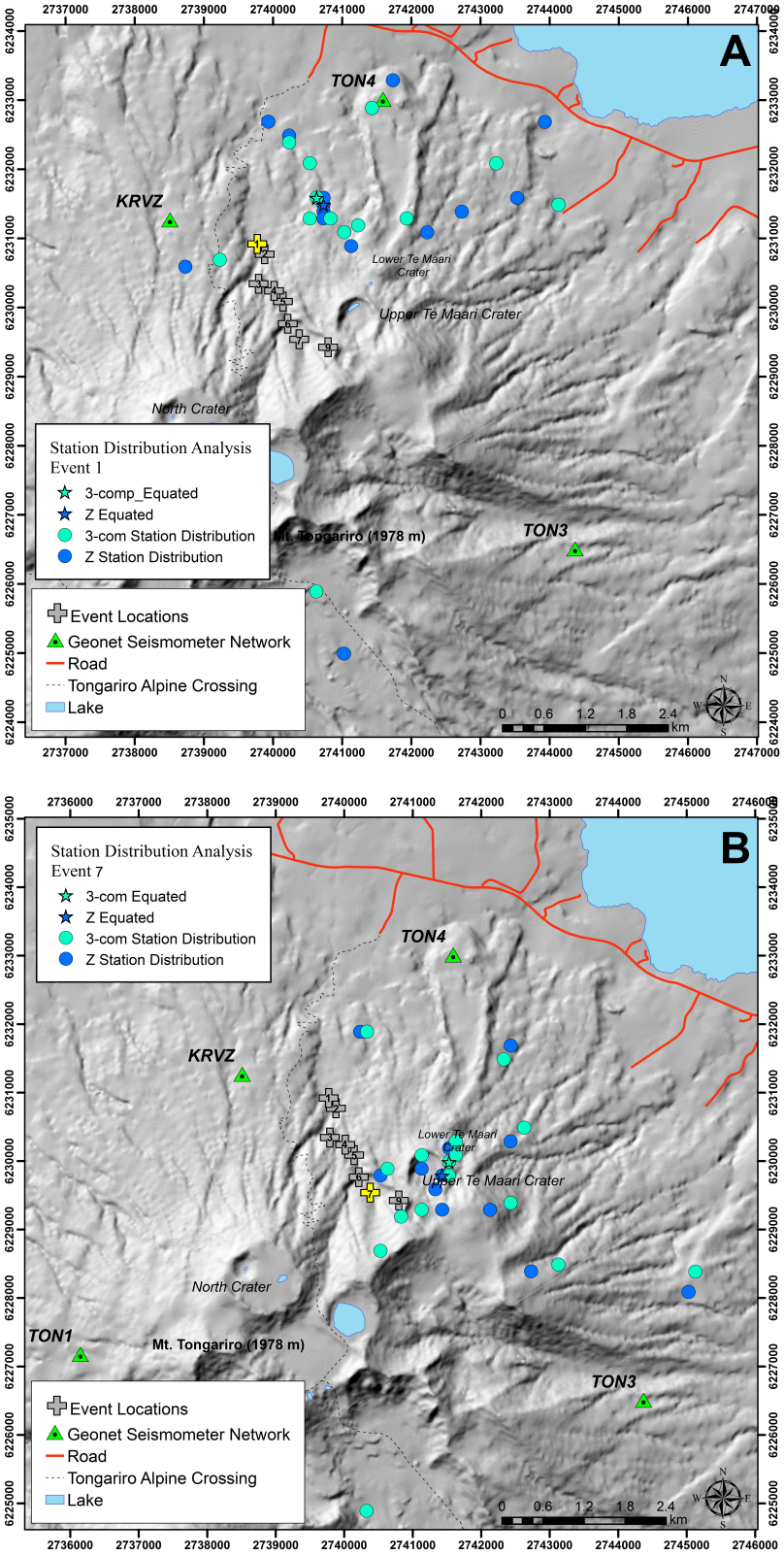


Figure 5.4 Analysis of the location effects for station distribution effects for comparing the vertical component and 3-component distribution for event 1 (A) and event 7 (B). Note the difference in spread between the two data sets as well as events.

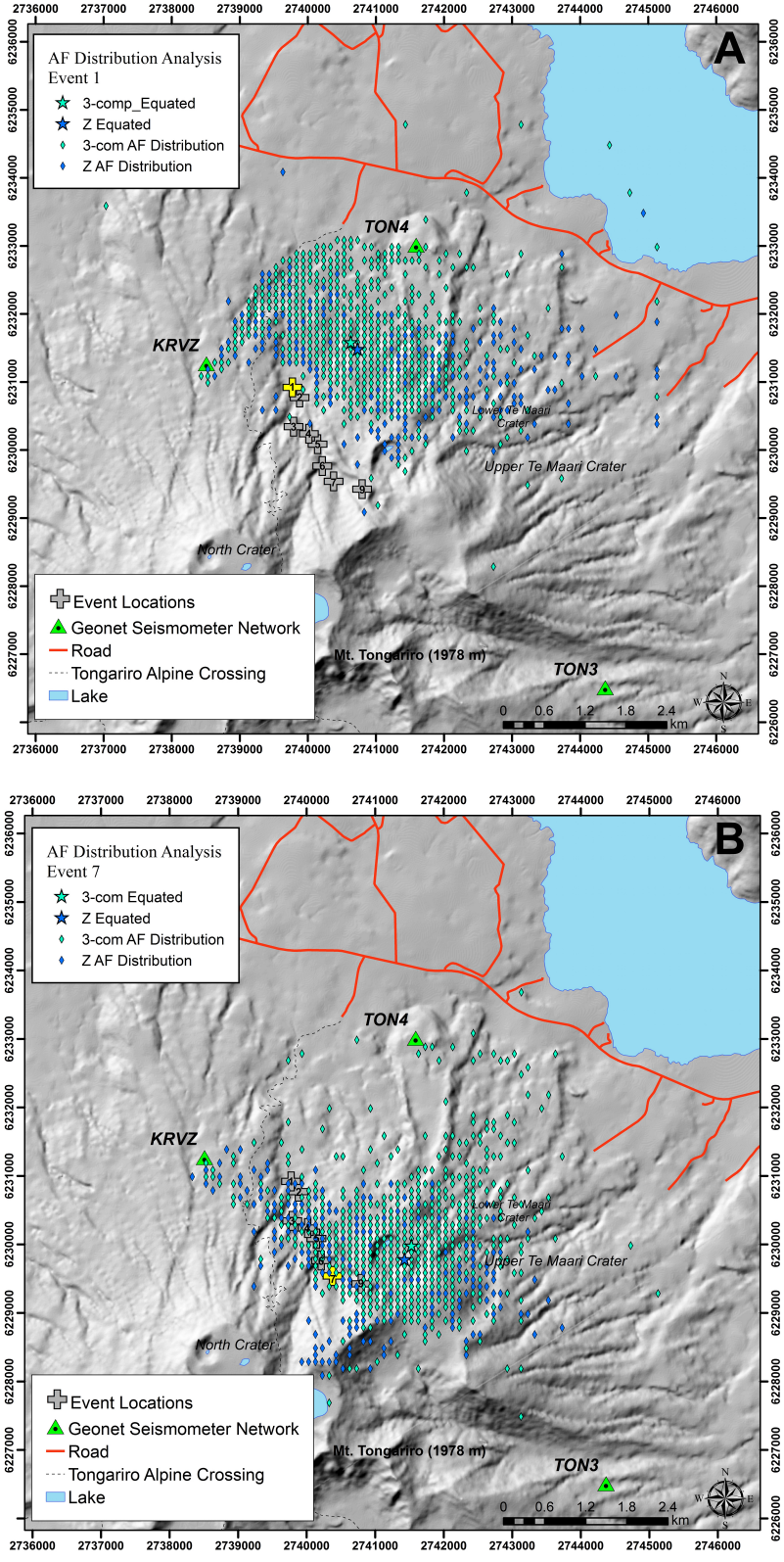


Figure 5.5 Analysis of the location effects for amplification factors of standard errors for comparing the vertical component and 3-component distribution for event 1 (A) and event 7 (B).

To examine the distribution of results by using different station sets, we use a jackknife and bootstrapping method (i.e., Tukey, 1958, Lahr, 1989), where subsets of the five station array are systematically resampled to assess the effects of station location. Computing station analysis results (Figure 5.4), the lateral true distance errors for the vertical component and all three components are 2.26±1.49 km and 1.92±1.34 km for event 1 (Figure 5.4A) and 1.88±1.36 km and 1.92±1.34 km for event 7 (Figure 5.4B). Even though the errors are very close, using three components limits the extreme error locations away from the center of the five station geometry. Vertical results have true location errors up to 6.10 km for event 1 and 4.65 km for event 7, whereas using all three components yields maximum errors of 5.10 km for event 1 and 4.65 km for event 7.

Estimating AF location error values, we calculate 1000 randomly generated AF corrections by using the standard deviations (Table 5.1) to generate a random normal distribution (Figure 5.5). Location uncertainties for comparing the vertical component and three components are 1.58±0.85 km and 1.60±0.74 km, respectively, for event 1 (Figure 5.5A) and 1.34±0.76 km and 1.59±0.84 for event 7 (Figure 5.5B).

Standard error estimations for both methods compare favorably, but can be misleading. To determine if one approach is better than the other, we conduct an F-test (i.e. Harper, 1984) by comparing the variance or spread of dispersion of the location results. Furthermore, to be consistent with above results we will only describe F-test outcomes for active sources 1 and 7. The F-test uses probabilities

and null hypotheses. If the F-test returns a value of $p>0.05$ then the null hypothesis is rejected and the datasets are statistically the same. For computation, distances from source location are calculated to determine which dataset is superior if proven statistically different. For the F-test, 1000 randomly distributed distances are used from calculating root mean squared errors (RMSE) (i.e. Willmott, 1981) for each of the recorded signals (Table 5.2).

To obtain the best comparison possible, we used locations without AF corrections to remove any biases in the corrections. The 1000 RMSE distances resulted in means of 2.18±1.33 km (vertical) and 2.06±1.16 km (3-component) for event 1, and 2.37±1.29 km (vertical) and 2.33±1.24 km (3-component) for event 7. F-test results through using RMSE show that for event 1, there are statistical differences between the three components dataset and the vertical component data set, with a P-value of 0.027. Event 7, on the other hand recorded, a P-value of 0.544, which means both methods produce statistically the same results.

Table 5.2 Root mean squared errors

1.00E-06	East	North	Vertical
KRVZ	0.516	0.606	0.217
WTVZ	0.726	0.067	0.031
TON1	0.188	0.192	0.086
TON3	0.214	0.156	0.064
TON4	0.451	0.388	0.207

5.5 Component Analysis

ASL location results on Te Maari show statistical differences between using three components and using the vertical component based on true location error. Furthering the investigation into reducing the amount of error in ASL results, we conduct the aforementioned techniques (i.e. station analysis, AF analysis, and F-test) on each individual station component. Figure 5.2 shows that the horizontal components have higher spectral amplitudes for each event, and thus may produce more reliable ASL results.

ASL results for individual components (Figure 5.6) show the locations for each active source event, along with the results for the 3-component analysis. Average true location errors for all six events are ~1.03 km for vertical (blue circles), ~0.94 km for the East (pink circles), and ~1.22 km for the North component (green circles). The individual components show similar plotted locations for each event, only yielding an average standard error or spread of ±0.25 km on the surface and ±19.25 km in depth when all events are combined.

Examining error estimations for station locations and amplification factors, we conduct the same jackknife and error methods as above for each component. Station distribution analysis (Figure 5.7) depicts each component's ASL locations through subsets of station use. Active source event 1 provided distance errors of 2.26±1.49 km, 1.87±1.40 km, and 2.25±1.65 km for Z, E, N components. Event 7 yielded distance errors of 1.50±1.37 km, 1.42±1.41 km, and 1.79±1.48 km respectively.

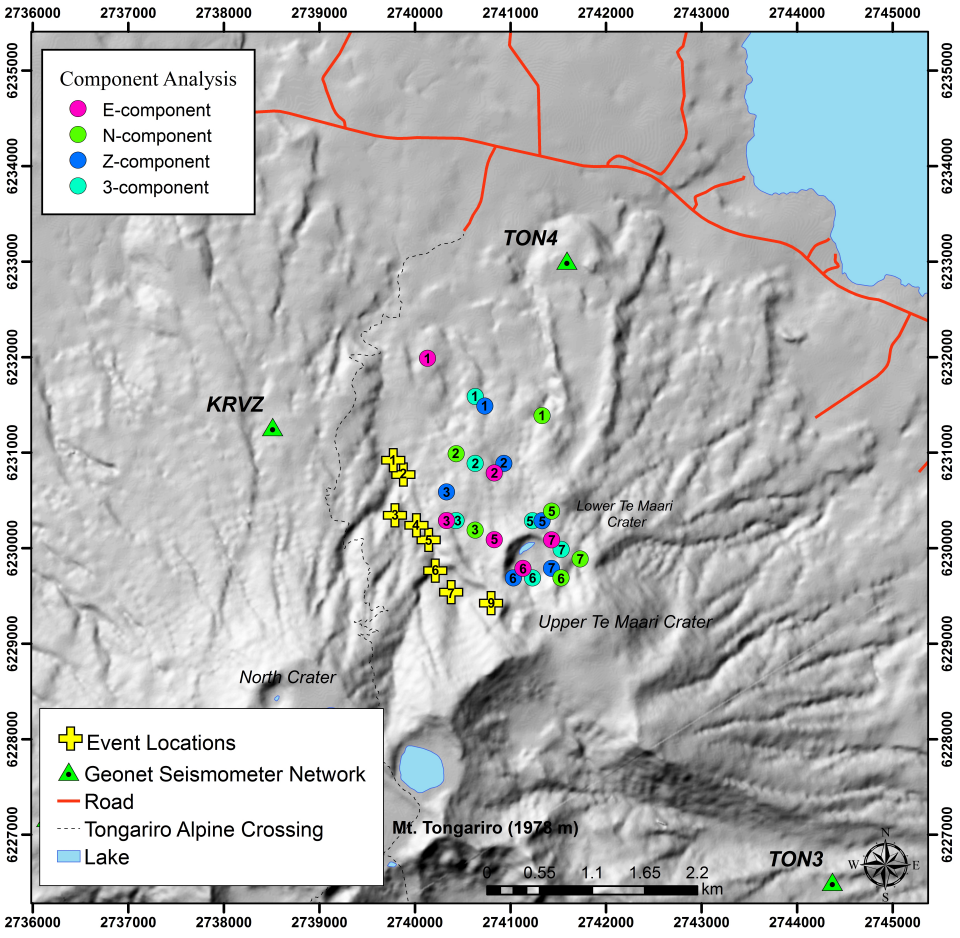


Figure 5.6 ASL minimal residual location results for the vertical component (blue), 3-component amplification factor method 1 (teal), East component (pink), and North component (green).

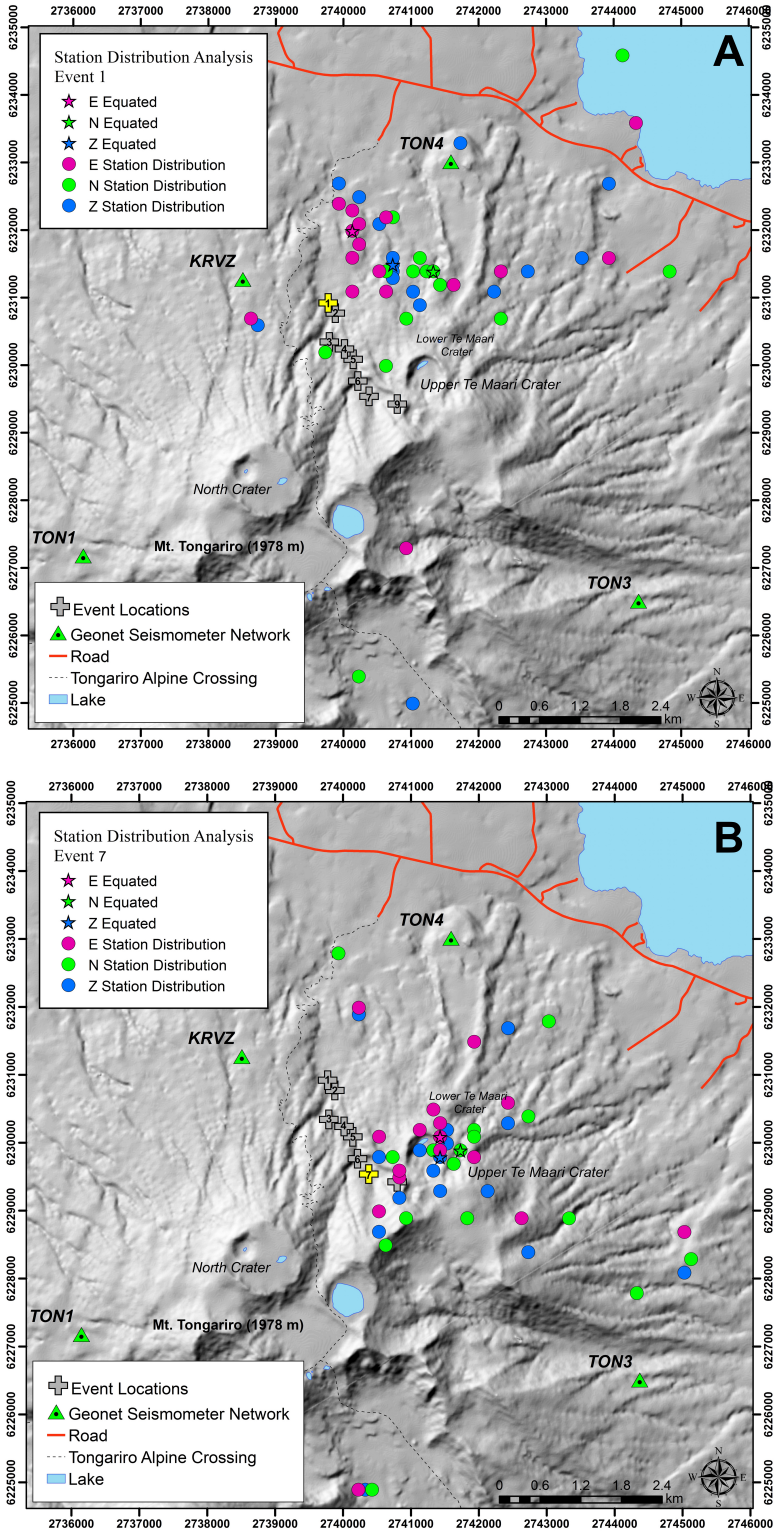


Figure 5.7 Analysis of the location effects for station distribution effects for comparing each of the seismic components for event 1 (A) and event 7 (B). Note the difference in spread between the two data sets as well as events.

AF analysis for individual components (Figure 5.8) shows the randomly generated 1000 AF locations for each component. From the 1000 ASL locations, errors of 1.58±0.85 km, 1.47±0.77 km and, 1.93±0.77 km for event 1 were produced. Event 7 had location errors of 1.34±0.76 km, 1.64±1.00 km, and 1.59±0.64 km respectively for Z, E, and N components.

Next we examined the location differences between the three components by conducting an F-test with multivariable analysis. Determining RMSE values for the event signals (Table 5.2), we calculated 1000 randomly distributed RMS amplitudes for ASL locations. F-test results for all three components for event 1 produced a p-value of 0.027, which indicates that all three components give statistically different results. Through multivariable analysis, we obtained p-values of 0.005 for Z-E, 0.531 for Z-N and 0.022 for E-N, showing that the Z- and N-components for event 1 are statistically the same. The 1000 RMSE ASL locations resulted in errors of 2.18±1.33 km, 2.03±1.06 km, and 2.15±1.20 km for Z, E, and N components respectively. Conducting the same tests, event 7 produced errors of 2.37±1.29 km, 2.33±1.24 km, and 2.35±1.26 km, with a p-value of 0.015. Computing component pairs separately, we acquire p-values of 0.020 for Z-E, 0.812 for Z-N, and 0.01 for E-N. As with event 1 the vertical and N-components for event 7 are statistically the same.

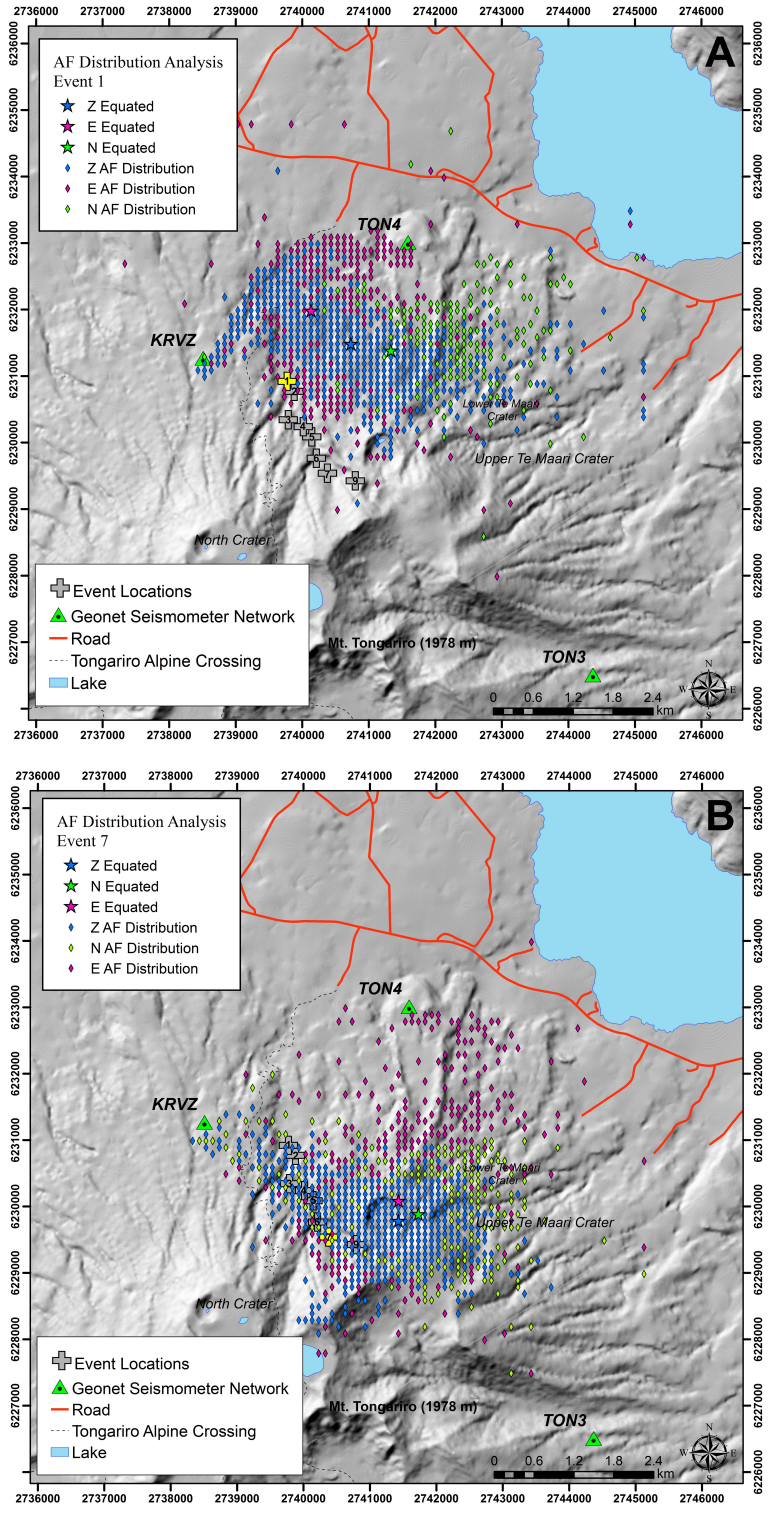


Figure 5.8 Analysis of the location effects for amplification factors for the distribution of standard errors for comparing each of the seismic components for event 1 (A) and event 7 (B). Note the difference in spread between the two data sets as well as events.

5.6 Discussion

Through examining the locations and distributions of the multiple tests conducted (AF distribution, station jackknife, RMSE distribution), the differences in results between using only the vertical component and using all three components is minimal. If we combine all the error tests, it becomes apparent that using three components for ASL results produces a tighter location pattern or higher precision.

To further confirm this, we conducted the AF and station distribution analysis again, but this time from the standard base locations instead of calculating the true error from the active source drop. This will give us a good representation of spatial distribution errors for both location methods. For the amplification factor distribution, we obtained standard distribution errors of ±0.88 km and ±0.68 km for event 1 for vertical and 3-component respectively. Furthermore, for event 7 distribution errors of ±0.89 km and ±0.72 km were produced. Conducting the same test on the station distribution Jackknifing technique, we obtain spatial errors of ±1.67 km for vertical and ±1.55 km for 3-component locations for event 1. Calculating spatial distributions for event 7 resulted in errors of ±1.37 km for the vertical component and ±1.41 km for the 3-component results.

Examination of true error distributions and spatial error distributions show that using a 3-component setup for the ASL method produces more precise location results, but not necessarily more accurate results. Many factors could be the cause of this phenomenon, but the most probable influence is that the averaging of the

three components smooths the data out, eliminating the extreme values and thus creates a tighter spread.

To further investigate this concept, we ran the same spatial distribution error assessment on each of the components. AF spatial distribution errors for event 1 were ±0.88 km, ±0.65 km, and ±0.64 km for Z, E, and N components. Event 7 resulted in errors of ±0.89 km for the vertical, ±0.80 km for the E-, and ±0.59 km for the N components. Station distribution errors for individual components produced spreads of ±1.70 km, ±1.58 km, and ±1.78 km for event 1 and ±1.37 km, ±1.41 km, and ±1.48 km for event7 for Z, E, N components respectively. The spatial distributions show that the vertical component is not always the most precise component. This further suggests that the 3-component analysis is most likely averaging the three components and producing results that are more precise than just the vertical component alone.

While using all three components yields more precise results, it is more important to have more accuracy in the results or minimal true distance errors from the source. In the case of our RMSE analysis, if we look just at true error distance, using all three components decreases the error in the results. The difference in error is more evident for event 1 due to the proximity to stations KRVZ and TON4 noted in Chapter 3, which can force the location estimates to increase laterally. If using three components yields more accurate location results than the vertical results, the east or north components must produce improved locations. The RMSE analysis for individual components shows that for event 1 the

E-component has the lowest true distance error results and for event 7 the N-component has the least true error distance. These findings of non-vertical components yielding less error distance "pulls" the 3-component results closer to the true locations of the active sources.

Considering that the horizontal components have stronger energies (Figure 5.2) than the vertical component, it is possible that just using one of the components will produce improved results. We noted in section 5.1 and 5.2 that others have shown in the past that many geological phenomena produce more seismic energy in non-vertical directions. Throughout the error analysis the E-component has produced improved accuracy and precision over the other two directions, but is not the case in every instance. Furthermore, the N-component has higher amplitudes than the vertical component, but has been shown to be statistically the same as the vertical component in the RMSE analysis. Using just a non-vertical component could also cause misleading or poor results, due to missed energies from other directions. Locating a mass flow just using the E-component might miss directional changes and energy within the flow, which would lead to large location errors.

While the active source events at Te Maari produced the best results in the E-component, this will not always be the case. We have also shown that conducting ASL with three components will increase the accuracy and precision of the results, but this is also not universal. Using all three components averages the results, but if the horizontal components were weaker than the vertical component, the results

would theoretically not be the same. To really understand if using all three components for the ASL method yields better results, synthetic tests (i.e. Kumagai et al., 2013) need to be conducted.

5.6.1 Estimating locations for 3-component ASL using H/V ratios to correct site response

Up until this point we have used the coda wave normalization (CWN) technique to estimate amplification factors for each seismic station. This may introduce problems when using all three components of the seismometer for ASL, due to the way the site corrections for the vertical components are processed in the same way as for the horizontal components. To check if this processing technique has any issues, we relocate each active source event by correcting site effects using the H/V method (i.e. Nakamura, 1989).

To determine site amplifications using the H/V method, we follow the steps laid out by Lermo and Chavez-Garcia, (1993) and Konno and Ohmachi, (1998). In estimating H/V ratios we use the same earthquake data as from the CWN method. The proceeding sequence follows along the lines of, slitting data into 10 s time windows overlapped by 5 s, create spectral amplitudes, smooth the data by the Konno and Ohmachi technique, averaging the horizontal components using quadratic means, computing H/V ratios for each time window, and then finally averaging all the time windows (Table 3). Furthermore, we applied an SNR limit for each signal/time window at SNR ≥ 2 using a 10 s pre-earthquake time window.

Table 5.3 H/V site corrections

	H/V	SD	H/Ve	SD	H/Vn	SD
KRVZ	1.1168	1.4407	1.0099	1.1646	1.1593	1.2037
WTVZ	0.8851	0.8532	0.7333	0.7072	0.9286	0.7462
TON1	1	NA	1	NA	1	NA
TON3	0.6888	0.7526	0.5690	0.5414	0.7906	0.8200
TON4	1.0183	0.6423	1.0452	0.6000	0.8952	0.5553

The estimated locations of the active source events with H/V site corrections are shown in figure 5.9 along with the estimated locations with the CWN AFs. The H/V estimated locations for the lower debris flow channel events are heavily influenced by stations KRVZ and TON4, whereas the upper channel events are slightly "pulled" down channel towards the two stations. Averaging all the active source events together the H/V method yields true location errors of 1.50 km for 3-component, 1.62 km for the vertical component, and 1.76 km, 1.57 km (not shown) for the East and North components respectively. In comparison with the CWN locations, the H/V locations do not follow the semi-linear pattern with the active source events. Additionally, the average true distance errors for the CWN method are, 1.01 km, 1.03 km, 0.94 km, and 1.22 km for 3-component, vertical, East, North components respectively.

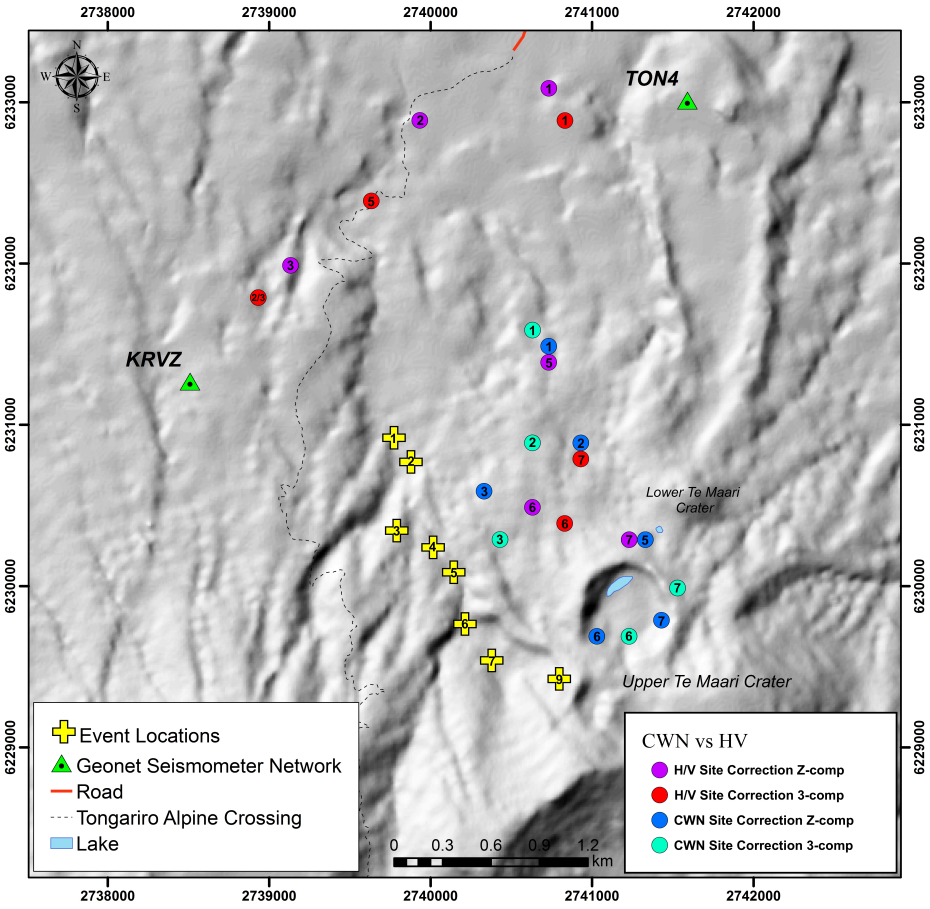


Figure 5.9 ASL minimal residual location results for the CWN vertical component (blue), and 3-component (teal), as well as, the H/V 3-componet (red) and vertical component (purple) results.

In order to get a full understanding of the differences between the H/V corrections and the CWN corrections, we conduct the same AF distribution tests as in the above sections where 1000 randomly distributed AFs are calculated from the standard deviations of the site corrections for the 3-component locations (Figure 5.10). Likewise, we will only describe results for events 1 and 7, as they are at opposite ends of the debris flow channel and show different site and spatial settings. AF distributions for event 1 (Figure 5.10A) show that the distributions for the H/V method tend to be more influenced by stations KRVZ and TON4 than for the CWN method. This can be seen in the average errors for each method. For event 1 the H/V method has true location errors of 2.13±0.83 km whereas, the CWN has errors of 1.60±0.74 km. While the spreads are similar, the accuracy of the H/V results are over 500 m more away from event 1 than the CWN results.

AF distributions for event 7 (Figure 5.10B) show similar trends when compared to event 1. Event 7 H/V distribution locations are also strongly effected by stations KRVZ and TON4. The event 7 H/V distributions also have locations that tend towards station TON1. Comparing the overall distributions between the CWN and H/V results, the true error distance or spread from event 7 is 1.59±0.84 km for the CWN method and 2.40±1.25 km for the H/V method. The 3-component results show that in both accuracy and precision the CWN method produces more reliable results.

While both of these methods are strongly influence by station distribution and the increased strength in the horizontal components of the active source events, the H/V method is more affected probably due to the way the AFs are calculated. Since the H/V method assumes that the vertical component is free of site response, the horizontal and vertical components should not have similar site responses (Bonilla et al., 1997). In the case of Te Maari, the site responses are similar in all three directions, making it difficult to estimate quality amplification factors. The differences between the two methods can be shown not only in the estimated true error distance from each active source event, but also from both the AF distributions from the events, as well as, the spread from the equated or "base" locations (Table 4).

Table 5.4 Summary of results

Errors in km	3-Component	Z-Component	E-Component	N-Component
Average True Error Distance (CWM)	1.01	1.03	0.94	1.22
Average True Error Distance (H/V)	1.50	1.62	1.76	1.57
Station Distribution Event 1 (CWN)	1.92±1.34	2.26±1.49	1.87±1.40	2.25±1.65
Station Distribution Event 7 (CWN)	1.96±1.34	1.88±1.36	1.81±1.33	2.35±1.44
Station Distribution Event 1 (CWM to base)	1.26±1.55	1.60±1.67	1.50±1.58	1.42±1.78
Station Distribution Event 7 (CWM to base)	1.51±1.41	1.50±1.37	1.42±1.41	1.79±1.48
AF Distribution Event 1 (CWM)	1.60±0.74	1.58±0.85	1.47±0.77	1.93±0.77
AF Distribution Event 7 (CWN)	1.59±0.84	1.34±0.76	1.64±1.00	1.59±0.64
AF Distribution Event 1 (CWM to base)	1.04±0.68	1.06±0.88	1.07±0.65	1.06±0.64
AF Distribution Event 7 (CWM to base)	1.04±0.72	0.92±0.89	1.18±0.80	0.88±0.59
AF Distribution Event 1 (H/V)	2.13±0.83	2.29±0.87	1.96±0.75	2.31±0.80
AF Distribution Event 7 (H/V)	2.40±1.25	2.30±1.28	2.52±1.10	2.25±1.26
AF Distribution Event 1 (H/V to base)	1.24±1.22	1.21±1.21	1.34±1.13	1.14±1.27
AF Distribution Event 7 (H/V to base)	2.95±1.65	2.07±1.40	1.84±1.36	2.06±1.33
RMSE Distribution Event 1	2.06±1.16	2.18±1.33	2.03±1.06	2.15±1.20
RMSE Distribution Event 7	2.33±1.24	2.37±1.29	2.51±1.43	2.35±1.26

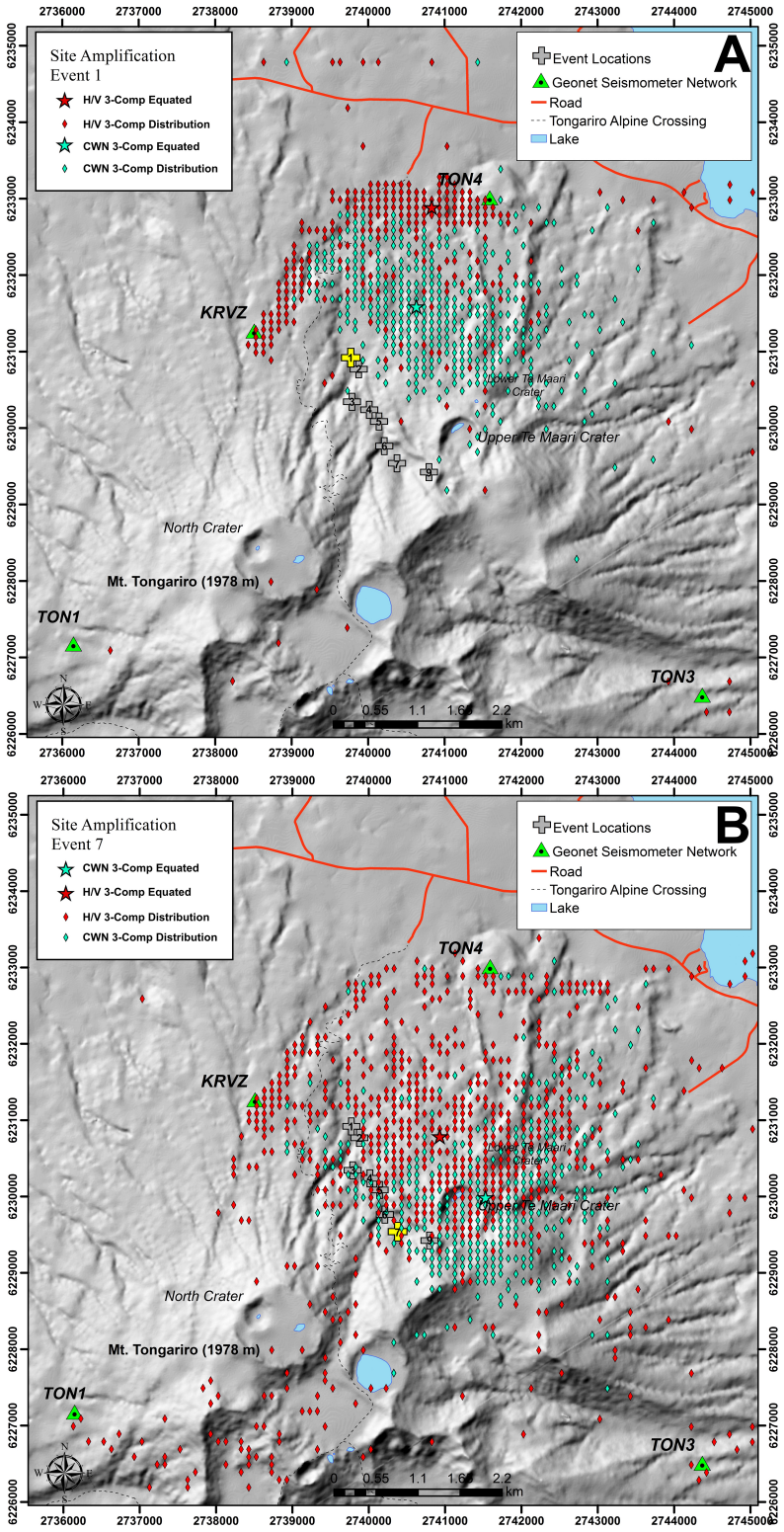


Figure 5.10 Analysis of the location effects for amplification factors of standard errors for comparing the CWN and H/V method 3-component distribution for event 1 (A) and event 7 (B).

5.7 Conclusions

The first test on using 3-component analysis for improving amplitude source location results has been conducted. Our results from active source events on Te Maari volcano, New Zealand show results from ASL using all three components yield a decrease in true distance error and an increase in location precision (Table 4). Average location errors for all the active source events differed between 1.03 km for the vertical component and 1.01 km for 3-components while using the CWN method and 1.62 km (vertical) and 1.50 (3-compontnet) using the H/V method. Conducting a RMSE analysis for the active source events, location results for event 1 and 7 produce errors of 2.18±1.33 km and 2.37±1.29 km for vertical results and 2.06±1.16 km and 2.33±1.24 km for 3-component results. We conclude that using all three components of the seismometer average the components eliminating the extreme values, thus producing more precise results. Furthermore, we note that in terms of more accurate results, the horizontal components had higher amplitudes than the vertical component, producing better results. The 3-component analysis may not always produce more accurate results if the north and east directions have weaker or different amplitudes than that of the active source events, and therefore synthetics must be calculated and used to determine if using all three components manufactures more accurate source locations.

CHAPTER 6: SYNTHESIS AND CONCLUSIONS

Chapter contents

6.1 Synthesis……186
6.2 Specific findings……198
6.2.1 Using active sources to determine dynamics and locations……198
6.2.2 Using active sources to calibrate the ASL method……199
6.2.3 Using multiple location techniques to understand volcanic eruptions……199
6.3 Conclusions……201
6.3.1 Evaluating the research objectives……201
6.4 Future recommandations……203

CHAPTER 6: SYNTHESIS AND CONCLUSIONS

6.1 Synthesis

Volcanic eruptions and accompanying phenomena are of major concern in risk management and hazard assessment. When a volcanic event occurs (i.e. eruption, or volcanic mass flow), the dynamics and location of the event are of great importance for hazard analysis. Calculating the dynamics of an event can determine many properties (i.e. velocity, size, energy, etc.) that help establish warning protocols. Along with these physical properties, knowing the location of an event (i.e. eruption vent, mass flow front location, etc.) can precisely determine when and where the greatest risk is. This research has looked deeper than ever before at methods to determine the location and dynamics of volcanic events, in order to improve warning systems, which may contribute to decreasing risk in volcanic areas.

There are many ways to estimate the locations and dynamics of volcanic events, but geophysical instruments (i.e. seismometers, acoustic sensors, accelerometers, etc.) have recently been shown to be the most effective. There are a variety of techniques to determine the dynamics and locations of volcanic events from geophysical instruments, each providing differing results and outcomes. Some more established method have been described in detail, here (Chapter 1) and by others, for instance phase arrival (i.e. Lahr, 1989), semblance (i.e. Neidell and Taner, 1971), and back projection (i.e. Ishii et al., 2005). However, the amplitude source location (ASL) and the active source (AS) methods are still emerging

techniques for hazard identification in volcanology. Chapter 6.1 explores these two methods, comparing and contrasting them, and finally listing some potential uses for these techniques in the future (Chapter 6.4).

ASL has become increasingly popular in recent years, due to its relative ease of use. The equations are straightforward and once implemented, only a simple grid search technique needs to be applied. The ease of the ASL method makes it an ideal candidate for implementation into seismic-based volcanic warning systems, which is discussed further in Chapter 6.4. Conversely, the AS method is not as straightforward. For this method, AS experiments need to be conducted in advance of an event taking place, in order to calculate the properties of the active sources. This means going out in the field and creating man made sources from explosions, hammer hits, vibration equipment, or in the case of Jolly et al. (2012,2014C) dropping large bags of sand. Once the experiment is complete, the data need to be processed, and locations and properties of each AS must be determined. Only after will the active sources be ready to use as proxies for a naturally occurring event.

ASL achieves reasonable results in locating events, as long as there are multiple seismometers in the area to record the event. ASL can also estimate a location for any resolution of grid size. AS on the other hand can only locate events in close proximity to where the AS experiment was conducted. Additionally, the resolution for the AS method is only as precise as the spacing and number of AS events.

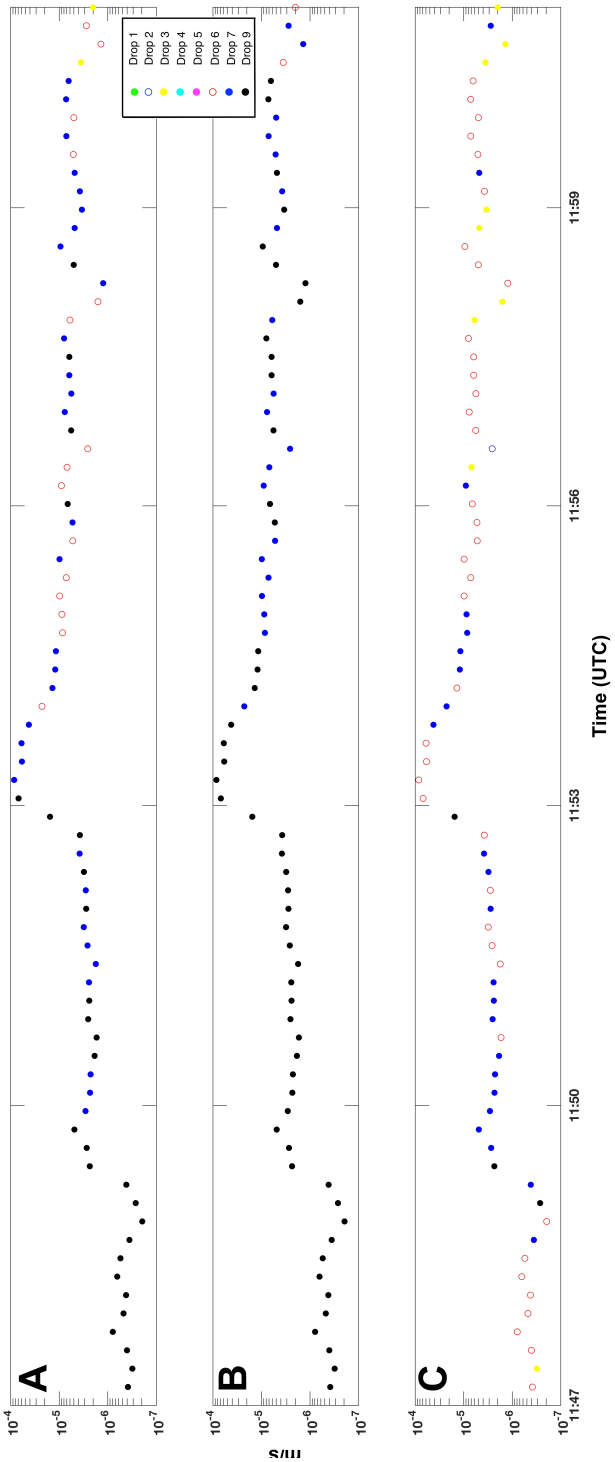


Figure 6.1 ASL and AS results of the seismic signal for the August 6th 2012 Te Maari, New Zealand eruption sequence. A) ASL results for surface waves, B) ASL results for body waves, C) Active source results. Color of dots represent the estimated nearest active source location (for drop locations refer to Figure 4.1).

Another advantage the ASL method has over the AS method is the ability to locate sources at depth easily. ASL results can be both determined with body and surface waves at depth using a 3-dimensional grid. In order for AS to locate an event at depth, the active sources would have to be at depth as well, with suitable coupling and encompassing the 3D space of the study area. Being able to locate sources at depth is important for tracking magma movement (Taisne et al., 2011), VT events (Kumagai et al., 2013), as well as LP (Battaglia and Aki, 2003), and VLP events (Kumagai et al., 2010). Likewise, if a volcanic eruption has many different events all occurring at once (i.e. Te Maari, 2012), being able to locate an event at depth is important in determining the timing of, for example, a debris flow during an eruption (Figure 6.1). On August 6th 2012, Te Maari volcano in Tongariro National Park, New Zealand erupted. During the eruption there was a debris flow, but the flow was obscured in the seismic signal by the continuing eruption and volcanic earthquakes. Figure 6.1 shows ASL results for surface waves (Figure 6.1A), body waves (Figure 6.1B), and AS results (Figure 6.1C) for the August 6th eruption sequence. Following the eruption through time, the ASL results (Figure 6.1A, B) show more of a correlation with upper channel drops, before the locations shift at ~11:54 UTC, to a mid-channel location, which could signify the start of the debris flow.

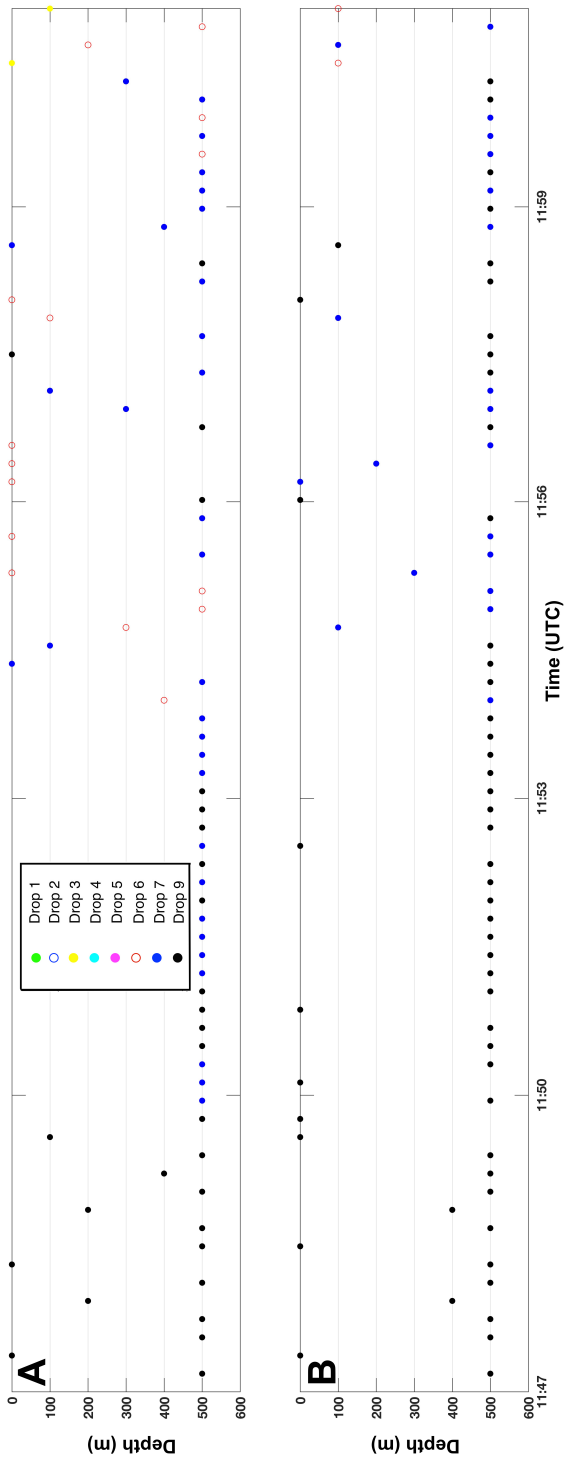


Figure 6.2 ASL depth location results for the August 6th 2012 Te Maari, New Zealand eruption sequence. A) ASL surface wave results, B) ASL body wave results. Dot colors represent the nearest AS drop from the estimated ASL results (for drop locations refer to figure 2.2).

Furthermore, if only the surface locations are known, it is not possible to know for certain that the estimated seismic locations changing to a lower channel position equates to the debris flow. Since ASL can determine locations at depth (Figure 6.2), looking at the depth of sources in the same time range as the shift to mid-channel locations will determine if this period actually coincides with the debris flow. Figures 6.2A and B both show a jump to the surface during the same time as the shift to the mid-channel location. Hence, it is clear that ASL has discovered the debris flow at ~11:54 UTC, which was the same time estimated by Procter et al. (2014) and Jolly et al. (2014B). Procter et al. (2014) revealed that the debris flow started as a debris avalanche from the crater rim and then flowed downslope, creating a dam at the drop 6 location, and producing the most energy during the flow. Afterwards the flow gained water and ran out down the channel as a debris flow.

In the instance of the Te Maari eruption sequence, along with other volcanic eruptions, unwanted noise could create many problems. ASL is based on locating the highest amplitude source in a pre-determined time window. In areas of increased noise, ASL does not always locate the source of interest. In volcanic areas, environmental factors, such as wind and rain, have as big of an effect as a secondary volcanic event. Being able to distinguish suitable sources in these conditions can prove to be difficult, and is a disadvantage for the ASL method. For example, volcanic mass flows are known to sometimes travel in pulses, which would force the ASL, as well as the AS, method to always locate up channel at the next pulse, instead of tracking the front of the flow (see Chapter 2 and Figure 2.3).

Likewise, in times of an eruption, blasts, multiple eruption related earthquakes, and even multiple flows can occur and create "random" source locations by ASL. In contrast, the AS method needs natural sources that have high correlation with the active sources in order for a natural source to be located properly.

One of the principal problems that plagues the ASL method is the reliance on geophysical assumptions. Since the decay and geometrical spreading of the seismic waves determine the ASL source location, assumptions about the source and path are needed. More specifically, input values for ground velocity and attenuation are required. In order to constrain the source and path effects, amplification factors are used (see Chapter 1.4.3.3.1, 3.2.2). As noted in the previous chapters, amplification factors do not always improve the ASL location results. Chapter 3 looks into the calibration of the ASL method by using active seismic sources as an alternative to amplification factors. Active sources are ideal for calibration, because, unlike ASL, the AS method does not require assumptions since all the site and path information is contained within each AS. Furthermore, using active sources to calibrate ASL has been shown to improve results (Chapter 3). At White Island, New Zealand (Figure 4.7), AS calibration improved the locations by ~400-500 m and placed the seismic excitations near the eruption vents. Additionally, at Te Maari (Figure 3.4C), AS calibrated results had true error distances reduced by over half when compared to locations using no corrections. Moreover, at Te Maari (Figures 6.3, 6.4), ASL was used to track the 2012 lahar, and the AS-calibrated ASL results locate in the channel, which was not the case for the non-calibrated locations. Furthermore, the calibrated ASL shows the flow bulking

around drop 6 and 5 more clearly (Figure 6.4), indicating the presence of multiple breakaways of the debris flow dam during the lahar.

Finally, to compare and contrast the ASL and AS methods, figures 6.1, 6.3,and 6.5 were created. Each figure depicts ASL results correlated to the nearest AS location for direct comparison. The August 6th Te Maari eruption (Figure 6.1) is an example of a volcanic eruption where multiple events are occurring. Comparing the AS results (Figure 6.1C) with the ASL results (Figure 6.1A and B), the ASL locations show pre-eruptive and eruptive activity higher up the debris flow channel around the crater rim. In contrast, the AS results tend to be clustered in the upper to mid-channel and at the peak eruption amplitude are highly correlated with drop 6. The difference between the two methods could be because the ASL method can locate at depth and is locating the tornillo earthquake (Jolly et al., 2014B) underneath the Upper Te Maari crater, instead of surface excitations with which the AS results are correlated. Furthermore, later in the signal the AS results show more excitations in the mid to lower channel; surface wave ASL (Figure 6.1A) shows similar results, but will "jump" periodically to higher energy excitations up channel that are located at depth.

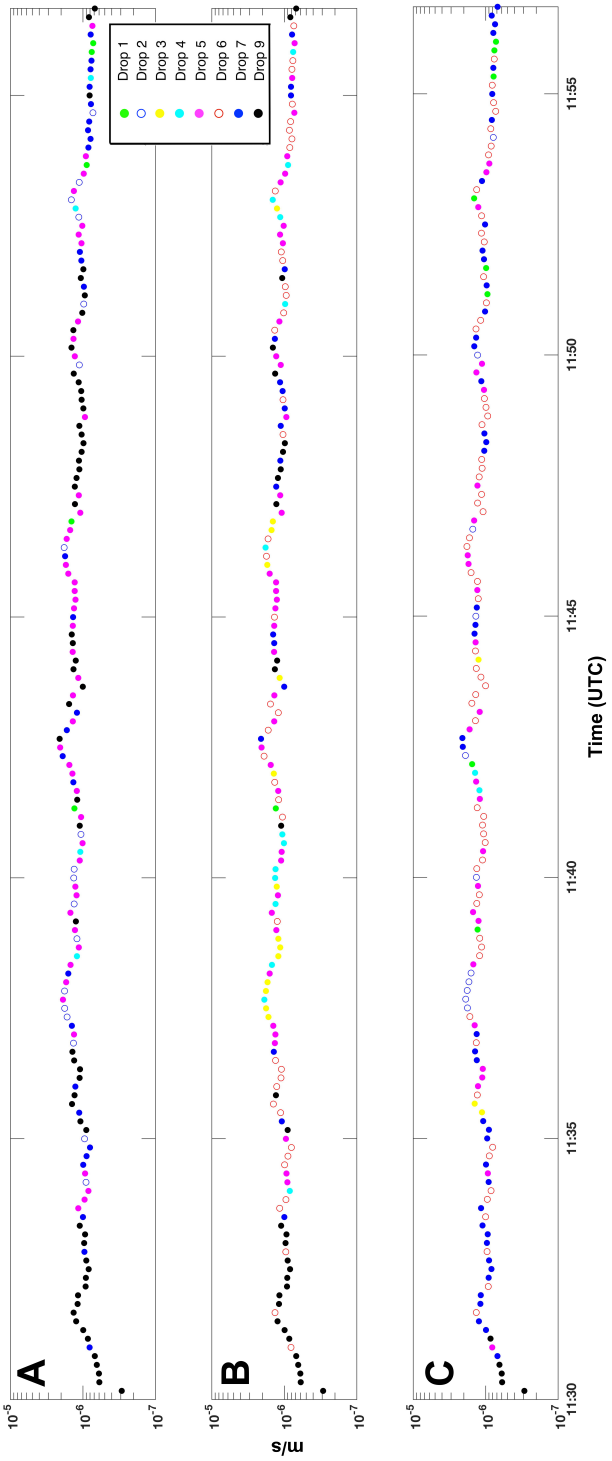


Figure 6.3 ASL and AS results of the seismic signal for the October 13th 2012 Te Maari, New Zealand lake breakout lahar. A) ASL results with no site and path effect corrections, B) Calibrated ASL results, C) Active source proxy results. Color of dots represents the estimated nearest active source location (for drop locations refer to figure 2.2).

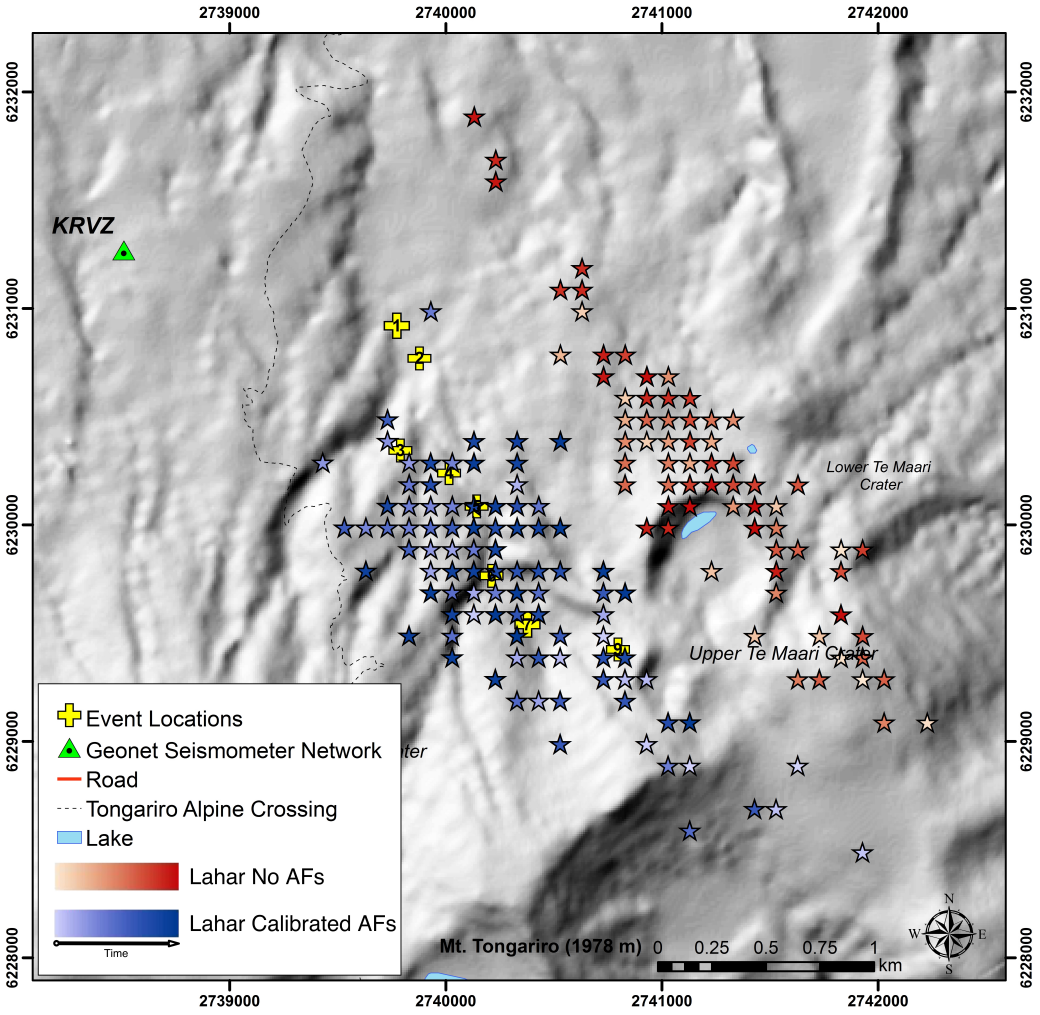


Figure 6.4 Map showing ASL results for the October 13th 2012 Te Maari, New Zealand lake breakout lahar. Red stars represent ASL locations with no site and path effect corrections and blue stars represent AS calibrated ASL locations. Color is coded to time, which represents early (lighter) to later in the lahar (darker). Each star represents a 10 sec non-overlapping time window.

When comparing ASL and AS results for the October 13th Te Maari lahar (Figure 6.3), the calibrated ASL results (Figure 6.3B) tend to display locations more up channel than the AS results (Figure 6.3C). Chapter 2 states that the lahar was caused by a lake breakout from a debris flow dam. The dam is theorized to have eroded and broken away in multiple stages (Procter et al., 2014). While both location methods show the back and forth location pattern in the results, the ASL locations tend to stay around the source of the lahar at drop 6. AS locations, on the other hand, especially those late in the lahar, are more located in the lower channel by drops 2 and 1. The difference in location results could be due to unwanted noise and poor seismic coupling. This is shown in figure 2.10A where most of the time windows are shaded grey due to the low signal-to-noise ratio. In addition, as noted before, ASL determines locations at where the peak energy is sourced, and with heavy wind and rain occurring at the same time as the lahar, unwanted source locations may be present.

For the April 27th 2016 eruption on White Island, active sources were used to calibrate the ASL method (Figure 4.7) in order to locate eruptive pulses. When compared directly to AS results (Figure 6.5) the locations for both methods for the pulses are very similar. AS results (Figure 6.5A) tend to correlate with drop 2 more than the ASL results (Figure 6.5B). Comparing this to figure 4.7 (ASL locations), each pulse should either be closer to drop 2 or 3; pulses 1, 4, and 5 should be closer to drop 3 and pulses 2, 3, and 6 to drop 2 from the results of Chapter 4. AS locations for the pulses show the same pattern as the ASL results for the location of each eruptive pulse. These results indicate the methods work well together.

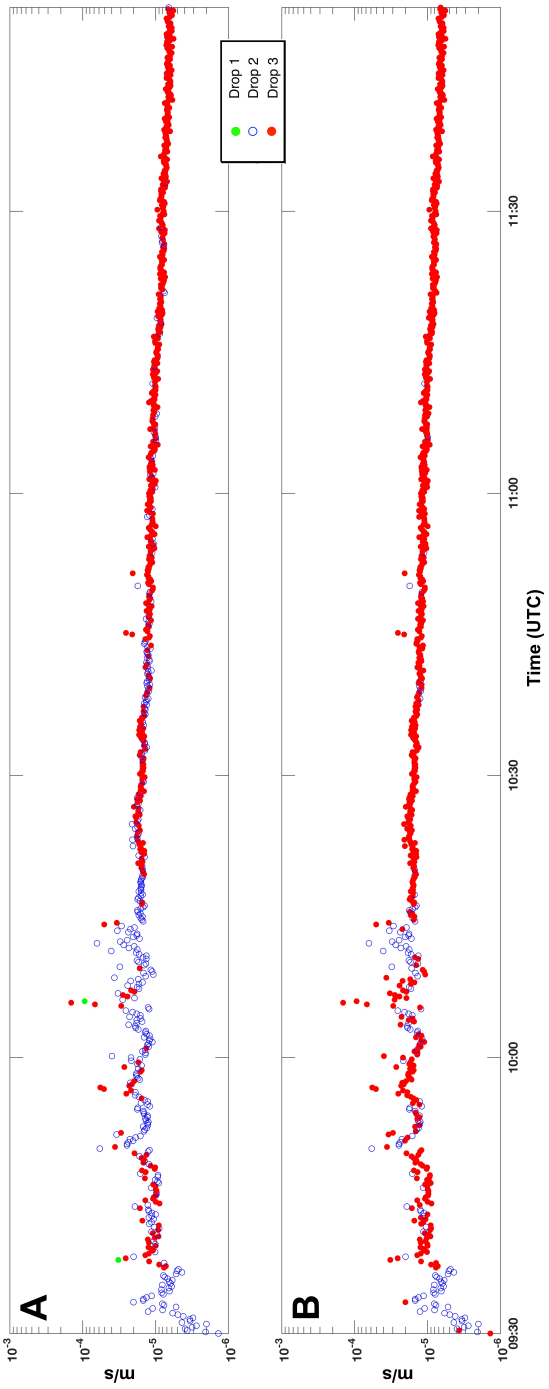


Figure 6.5 ASL and AS results of the seismic signal for the April 27th 2016 White Island, New Zealand eruption sequence. A) Active source results, B) Calibrated ASL results. Color of dots represents the estimated nearest active source location (for drop locations refer to figure 4.1).

6.2 Specific findings

6.2.1 Using active sources to determine dynamics and locations

Using active sources has many advantages when determining the dynamics and locations of volcanic events. Probably the most beneficial aspect of using active sources is that assumptions about the medium, and corrections of the source and path are not necessary. When an AS experiment has been conducted in an area of interest, and then a natural event occurs, only a correlation between the signals needs to be completed in order to estimate the dynamics of the event. Active sources are very useful for estimating the energy of an event, since the energies of the active sources are already known. An energy estimate for the natural event can be calculated by comparing the energy input of the natural event to the output from the AS data (equation 2.4). Information about energy release is very important for future development of warning systems. For volcanic mass flows, knowing the size and energy of a flow can help determine the potential hazards and area of destruction.

Using active sources as proxies has also been shown to be reliable in areas of increased unwanted noise. The ability for the AS method to flourish in times of increased noise is due to the active sources being emplaced in a single location rather than using a grid search to find the highest amplitude source as in the ASL method. Again, in terms of hazard assessment, especially for volcanic mass flows where in many cases they will be accompanied by heavy rainfall, the AS method can still locate and determine the energy output with reasonable accuracy.

6.2.2 Using active sources to calibrate the ASL method

Jolly et al. (2014C) noted that active sources encompass all the required site and path information. Not needing to make corrections or assumptions about site and path effects is what makes the active source method well-suited to calibrate the standard ASL technique. As mentioned in previous chapters, the ASL method needs to have amplification factors to better constrain location results, but they do not always work. Even when amplification factors produce more reliable results, true error distances can still be hundreds of meters. Using active sources to calibrate the ASL method has been shown to reduce the true location error by over half.

Reduction of the true error distances is vital for hazard assessment and could make the difference between a destructive and non-destructive scenario. The error reduction that calibrated ASL results produce could also make real time monitoring of volcanic mass flows more reliable and feasible.

6.2.3 Using multiple location techniques to understand volcanic eruptions

While using one geophysical technique can be appropriate and yield adequate results, it is always beneficial to produce results using multiple techniques for comparison and accuracy. Furthermore, knowing which methods are good for which type of events or situations is essential. The case of the April 27th, 2016 White Island eruption (for more detail see Chapter 4) is a perfect example of using multiple geophysical instruments and methods to provide more detail on vent locations and an eruption sequence on the island.

In order to understand the timing and dynamics of the eruption, multiple geophysical techniques were used because the eruption occurred overnight with no video or eyewitnesses. Exploiting acoustic sensors, the timing of each surface eruption was determined precisely. With the timing of the eruptions known, seismic methods could be used to determine how and where the eruption occurred. Knowing that an ASL method is reliable to locate sources in volcanic areas, the method was used to find vent locations. Through the ASL method calibrated by active sources, vent locations were determined with reasonable accuracy; the results positioned vent locations near or on top of crater depressions found after the eruption event. Knowing that waveform semblance is well equipped to locate sources with low frequency, the method was used to locate a VLP event that occurred before one of the eruptive pulses. The semblance technique located the VLP at ~1.0 km depth below the crater floor. Using all these geophysical devices and methods allows for the building of a story of how the eruption transpired. Through these techniques and results it has been theorized that at ~1.0 km depth a VLP occurred (found by semblance), which forced gas to ascend toward the surface as a slug through pre-existing cracks, eventually erupting at specific times (acoustics) and locations (AS-calibrated ASL).

Combining many geophysical methods allows for the accurate estimate of timing, location and probabilities of volcanic events. By utilizing as many methods as possible, the error reduces and hence warning systems improve. The better the warning systems are the more robust the hazard assessment and predictions can be.

6.3 Conclusions

The main aim of this research was to investigate multiple geophysical methods in order to better constrain volcanic mass flows and other volcanic phenomena. To conduct these investigations the research was separated into the following research objectives.

6.3.1 Evaluating the research objectives

- *Can active seismic sources be used to not only determine the dynamics of a lahar, but also give an estimation on flow location?*

  By using the October 13th 2012 Te Maari lahar in New Zealand, it was discovered that active sources were able to adequately locate the lahar. During the lahar sequence, the best correlated active source locations were at the mid channel location and lower, indicating the location of the debris flow dam breaking away in multiple stages. Furthermore, the active sources enabled an energy estimate to be made for the lahar of $\sim 1.93 \times 10^9$ Nm.

- *Can active seismic sources be used to calibrate the amplitude source location method?*

  The ASL method was calibrated using the active sources conducted on the Te Maari, New Zealand debris flow channel. In order to calibrate the ASL method, amplification factors were calculated from active source events to correct for source and path effects. When applying the active source corrections to the ASL method, true error distances decreased by over 50%

when compared to the results using no amplification factors (Figure 3.4C). This is because the active sources are single force excitations that yield the seismic impulse response and contain all the site and path effects within them.

Another example of the reduction of error when calibrating using active sources can be found in Chapter 4, where on White Island, ASL vent location estimations were reduced by ~300 m from no AFs, after being calibrated by active sources.

- *What are the eruption characteristics of the April 2016 White Island, New Zealand eruption?*

Through the use of multiple geophysical techniques, it was determined that the April 2016 White Island eruption occurred at ~09:30 UTC, and there were six distinct eruptive pulses. The six eruptive pulses were located using both the ASL method with seismic data and with waveform migration through acoustic data. ASL determined that there could be two to three different main vents, where pulses 1, 4, and 5, along with 2 and 6, erupted from the same vent. Using acoustic phase lag analysis (Figure 4.9), pulses 1, 4, and 5 were found to have larger phase lags when the signals are highly correlated, compared to pulses 2 and 6. This indicates that pulses 1, 4, and 5 are closer to station WIZ and pulses 2 and 6 are closer to station WSRZ. This observation fits well with the ASL results for the eruptive pulses.

By combining all the available data, it has been postulated that gas slugs rose up from depth through pre-existing cracks, and then erupted at the surface, creating the April 2016 eruption.

- *Does using all three components of a broadband seismometer improve location determinations for the amplitude source location method?*

Using the Te Maari, New Zealand debris flow channel active seismic sources, it was discovered that using all three components of a broadband seismometer yielded a decrease in the true error distance and an increase in the precision of the location.

Using all three components averages out the combined signals, eliminating the extreme values that one component could have. This produces the increased precision in the results. The increase in accuracy, however, could be from the location and type of source, and using all three components may not necessarily always decrease the true distance error to the real source location.

6.4 Future recommandations

This research looks at methods to understand volcanic events, with a goal to finding techniques that provide more accurate warnings. The research has explored a number of methods that could aid in the ability to identify volcanic events, but does not fully solve the problems in hazard prediction. The following

are suggestions of future work that may help or further the process of volcanic hazard monitoring.

- **Reducing error/3-components**

To obtain more reliable location results, one possibility is to use all three components of the broadband seismometer. This topic is studied in detail in Chapter 5. Chapter 5 notes that using three components reduces the amount of extreme error and increases the precision of the location results. When exploring the accuracy of the locations, further work focused on the creation of synthetics must be conducted to produce more reliable results.

- **Reducing error/methods and calibration**

Another way to reduce the location error of volcanic events is to use multiple techniques. This has shown to work well in Chapter 4, where active sources were used to calibrate ASL. Additionally, semblance was used to locate a VLP event at depth and all the methods combined created a theory of how and where the eruptions occurred. This concept can be used wherever multiple data types have been collected.

An additional idea would be to calibrate existing methods to reduce error. This is explored in Chapters 3 and 4. Furthermore, others such as Taisne et al. (2011) have used different approaches to traditional methods, for example exploiting amplitude ratios between seismic stations while using the ASL

method. Additional future work could be to better constrain path and site effects and add more detail to compensate for local geology changes.

- **Reducing error/instrumentation**

The best way to reduce error is by deploying more instruments to increase signal density and resolution. This can be in the form of more seismic stations, or using a combination of different types of geophysical instruments. Using acoustic sensors, along with seismometers, can greatly reduce the error, by combining the data from both. Also using accelerometers can reduce noise effects from events because they only measure the force of the mass moving by them and not distance external sources of noise like weather and smaller natural/human activity seismometers record.

- **Warning systems**

One of the most important future goals is to incorporate and automate these techniques for the creation of new and improved warning systems. In terms of volcanic mass flows, real-time tracking could eventually be implemented into already existing warning networks. The seismic techniques used in this thesis could be used to 1) detect a flow, 2) locate and estimate dynamics in real time, and 3) send out a report or instantaneous warning to people in the surrounding area.

APPENDIX A

Appendix contents

A.1 Back projection……208

Appendix A

A.1 Back projection

Back projection is a very practical and easy method to use for determining the locations of event sources. The advantage of back projection comes from not needing any input parameters about the event or assumptions on wave propagation (Ishii et al., 2007). Back projection was first popularized by Ishii et al. (2005) in seismology to track the rupture sequence of the Sumatra-Andaman earthquake and was later introduced into acoustic source location by Jolly et al. (2014). The acoustic version of the back projection method in 2-dimentional stacked time (t) can be described as:

$$S_j(t) = \sum_i^{i=1} A_i\left(t - \tau_{ji} + \Delta t_i\right) \quad \text{(A.1)}$$

where A is the normalized acoustic amplitude, τ is the theoretical acoustic travel time and Δt is the time correction used to maximize coherence, and is calculated by cross-correlating the initial few moments of the signal. Back projection works by taking advantage of waveform similarities across multiple stations by normalizing and stacking the data (Ishii et al., 2005). Using a grid search technique along with back projection the location of the source may be found. Equation (A.1) time shifts the waveforms and stacks the data for each grid point, thus the location with the maximum value becomes the estimated source (Ishii et al., 2007).

With only two sets of acoustic sensors on White Island, accurate locations are improbable, but with a three sensor alignment at each of the two stations,

probable location zones can be calculated. Figure A.1 shows back projection results for the six eruptive pulses during the April 27th 2016 eruption. Red colors show areas of higher stack values and more blue colors show regions of lower stack values. Only having two stations, generally the true error distance (~300-500 m) is going to be very significant, but by comparing the regions of high stack values, we can look at possible changes in vent position. The "band" of highly staked grid points shifts when comparing it to other pulses. From this shift we can confer that the vent at which the eruption is coming from must indeed change.

To summarize, back projection is an easy way to determine the location of many different volcanic events. The method can be used with acoustics as shown here, but also with seismic data as well. Others (i.e. Ishii et al., 2005 and Jolly et al., 2014B) have shown that back projection can produce reliable location results and also be able to track moving sources with great precision. In the case of White Island only having two sets of stations diminishes the quality and accuracy of a location estimate, and also we surmise the individual sensors at each station are too close to each other to find significant time differences and thus are now moved.

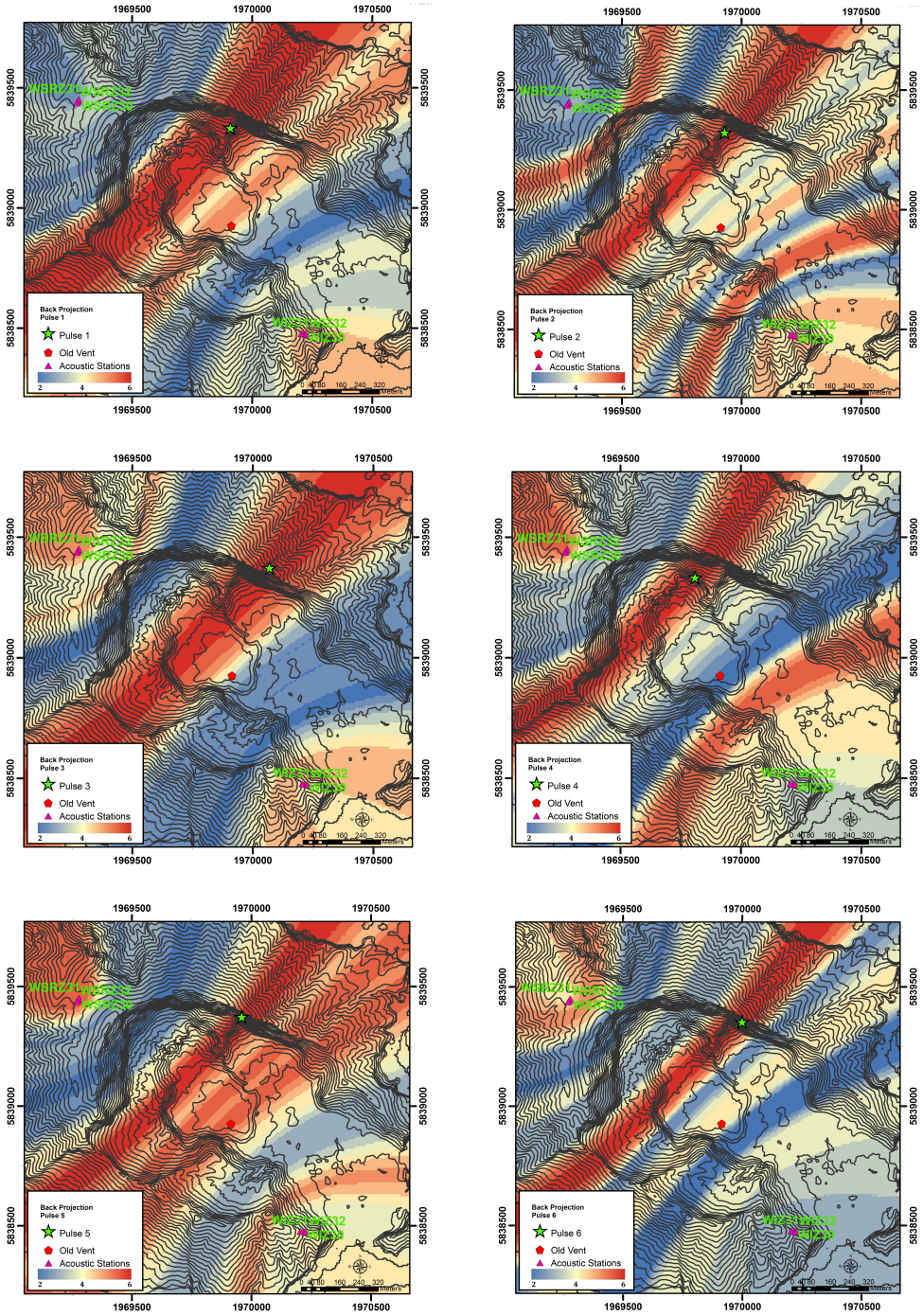


Figure A.1 Back projection results for the six eruptive pulses on White Island. Grid colors represent stack values from blue (2) to red (6). Stars represent the location of the highest stack value.

APPENDIX B: SUPPLEMENTARY MATERIAL

Appendix contents

B.1 Chapter 2 supplementary material……212
B.1.1 Programs……212
B.2 Chapter 3 supplementary material……213
B.2.1 Programs……213
B.3 Chapter 4 supplementary material……214
B.3.1 Programs……214
B.4 Chapter 5 supplementary material……215
B.4.1 Programs……215
B.5 Additional programs……215

Appendix B: Supplementary material

Appendix B contains all the Matlab codes and data used for the completion of this thesis. Summarized details of each code and data file are organized by thesis chapters.

B.1 Chapter 2 supplementary material

B.1.1 Programs

- DF_test.m

  Program to simultaneously calculate RMS amplitudes at a specific frequency range for natural and active source signals recorded on Te Maari, New Zealand.

- matcreatDF_test.m

  Program that uses the function DF_test to create large data matrices for multiple stations for natural and active source data.

- Corr_test.m

  Program to find the correlation coefficient between two matrices. This was used along with matcreatDF_test.mat to find the correlation between natural data and proxy data.

- DROP_Energy.m

  Program that calculates the energy of volcanic flows that flow down the Te Maari debris flow channel.

- Drop_find.m

Program that calculates matrices for plotting energy and correlation plots used for making the plots to be able to plot each drop a different color.

B.2 Chapter 3 supplementary material

B.2.1 Programs

- DROPrms.m

Program that calculates RMS amplitudes at specific frequency ranges for active source data.

- AMP_coda.m

Program that calculates RMS amplitudes at specific frequency ranges for coda waves.

- coda_amp_mat.m

Program that creates a matrix from multiple coda wave vectors of RMS amplitudes.

- coda.m

Program that calculates amplification factors from coda waves.

- grid3d.m

Program that finds locations of sources on a 3D grid with the ASL method.

B.3 Chapter 4 supplementary material

B.3.1 Programs

- white_amp.m

  Program that calculates RMS amplitudes at specific frequency ranges for events at White Island.

- grid_3dm.m

  Program that calculates source locations using the ASL method and by locations on the NZTM datum.

- cutdelayfind.m

  Program that finds lag times between signals. This program was used for acoustic signals.

- freq_WIplots.m

  Program to find peak amplitude and frequency of each lag time window as well as the correlation coefficients then plot them in four subplots.

- Seis_acc_energy.m

  This program finds the seismic and acoustic energy of recorded signals for the use of calculating a VASR.

B.4 Chapter 5 Supplementary material

B.4.1 Programs

- RMSsd.m

  Program to calculate root mean squared errors of seismic signals.

- RMSsd_asl.m

  Program that uses ASL to find locations of a X randomly sourced RMSE locations.

B.5 Additional programs

- bptest.m

  Program that calculates source location through the back projection method used in Appendix A.

- distance.m

  Program that calculates the distance between points.

- mat2shape.m

  Program that converts Matlab x,y,z data into shape files.

Appendix C: Statement of Contribution

Appendix C contains all the DRC 16 form for the 3 chapters in this thesis, which have been submitted for publication. The forms are in the attached CD in the directory named *Appendix C*.

Bibliography

Aki, K. (1980), Scattering and attenuation of shear waves in the lithosphere, *Journal of Geophysical Research, 85, 6496-6504.*

Aki, K., Chouet, B. (1975), Origin of coda waves: Source, attenuation, and scattering effects, *Journal of Geophysical Research, 80, 3322-3342.*

Aki, K., Ferrazzini, V, (2000), Seismic monitoring and modeling of an active volcano for prediction, *Journal of Geophysical Research, 105, 16617-16640.*

Almendros, J., Chouet, B, (2003), Performance of the radial semblance method for the location of very long period volcanic signals, *Bulletin of the Seismological Society of America, 93, 1890-1903.*

Angeli, M., Pasuto, A., Silvano, S, (2000), A critical review of landslide monitoring experiences, *Engineering Geology, 55, 133-147.*

Arattano, M, (1999), On the use of seismic detectors as monitoring and warning systems for debris flows, *Natural Hazards, 20, 197-213.*

Arattano, M., Marchi, L, (2005), Measurements of debris flow velocity through cross-correlation of instrumentation data, *Nat. Hazards Earth Syst. Sci., 5, 137-142.*

Arattano, M., Marchi, L., Cavalli, M, (2012), Analysis of debris-flow recordings in an instrumented basin: confirmations and new findings, *Nat. Hazards Earth Syst. Sci., 12, 679-686.*

Arattano, M., Moia, F, (1999), Monitoring the propagation of a debris flow along a torrent, *Hydrological Sciences, 44(5), 811-823.*

Aspinall, W., Miller, A., Lynch, L., Latchman, J., Stewart, R., White, R., Power, J, (1998), Soufriere Hills eruption, Montserrat, 1995-1997: Volcanic earthquake locations and fault plane solutions, *GRL, 25, 3397-3400.*

Battaglia, J., Aki, K, (2003), Location of seismic events and eruptive fissures on the Piton de la Fournaise volcano using seismic amplitudes, *Journal of Geophysical Research, 108.*

Bessason, B., Eiriksson, G., Thorarinsson, O., Thorarinsson, A., Einarsson, S, (2007), Automatic detection of avalanches and debris flows by seismic methods, *Journal of Glaciology, 53, 461-472.*

Boatwright, J, (1980), A spectral theory for circular seismic sources; Simple estimations of source dimension, dynamic stress drop, and radiated seismic energy, *BSSA, 70, 1-27.*

Burtin, A., Bollinger, L., Cattin, R., Vergne, J., Nabelek, L, (2009), Spatiotemporal sequence of Himalayan debris flow from analysis of high-frequency seismic noise, *Journal of Geophysical Research, 114.*

Burtin, A., Bollinger, L., Vergne, J., Cattin, R., Nabelek, L, (2008), Spectral analysis of seismic noise induced by rivers: A new tool to monitor spatiotemporal changes in stream hydrodynamics, *Journal of Geophysical Research, 113.*

Calvari, S., Tanner, L., Groppelli, G, (1998), Debris-avalanche depostis of the Milo Lahar sequence and the opening of the Valle del Bove on Etna volcano (Italy), *J. Volcanol. Geotherm. Res., 87, 193-209.*

Caplan-Auerbach, J., Prejean, S., Power, J, (2004), Seismic recordings of ice and debris avalanches of Iliamna volcano, Alaska, *Acta Vulcanologica, 16(1-2).*

Capra, L., Borselli, L., Barley, N., Ruiz, J., Norini, G., Sarocchi, D., Caballero, L., Cortes, A, (2010), Rainfall-triggered lahars at Volcan de Colima, Mexico: Surface hydro-repellency as initiation process, *Journal of Volcanology and Geothermal Research,198, 105-117.*

Capra, L., Macias, J., Scott, K., Abrams, M., Garduno-Monroy, V, (2002), Debris avalanches and debris flows transformed from collapses in the Trans-Mexican Volcanic Belt, Mexico – behavior, and implications for hazard assessment, *Journal of Volcanology and Geothermal Research, 113, 81-110.*

Cashman, K., Sparks, S, (2013), How volcanoes work: A 25 year perspective, *Bulletin of the Geological Society of America, 125, 664-690.*

Celebi, M. (1991), Topographical and geological amplification: Case studies and engineering implications, *Structural Safety, 10, 199-217.*

Chouet, B., Saccorotti, G., Dawson, P., Martini, M., Scarpa, R., Luca, G., Milana, G., Cattaneo, M, (1999), Broadband measurments of the sources of explosions at Stromboli Volcano, Italy, *Geophys. Res. Lett., 26, 1937-1940.*

Christenson, B., White, S., Britten, K., Scott, B, (2017), Hydrological evolution and chemical structure of a hyper-acidic spring-lake system on White Island, NZ, *Journal of Volcanology and Geothermal Research, DOI:10.1016/j.jvolgeores.2017.06.017.*

Cole, S., Cronin, S., Sherburn, S., Manville, V, (2009), Seismic signals of snow-slurry lahars in motion: 25 September 2007, Mt Ruapehu, New Zealand, *Geophys. Res. Lett., 36, L09405.*

Cole, J., Thordarson, T., Burt, R, (2000), Magma origin and evolution of White Island (Whakaari) Volcano, Bay of Plenty, New Zealand, *Journal of Petrology, 41, 867-895.*

Comiti, F., Macconi, P., Marchi, L., Arattano, M., Borga, M., Brardinoni, F., Cavalli, M., D'Agostino, V., Hellweger, S., Trevisani, S., Vischi, M, (2010), Debris flow monitoring and warning systems: A new study site in the Alps, *European Commission-EFD Common Implementation Strategy, Flash Floods and Pluvial Flooding.*

Coviello, V., Capra, L., Vazquez, R., Marquez-Ramirez, V, (2017), Seismic characterization of hyperconcentrated flows in a volcanic environment, *Earth Surf. Process. Landforms, DOI: 10.1002/esp.4387.*

Cronin, S., Neall, V., Lecointre, J., Palmer, A, (1996), Unusual "snow slurry" lahars from Ruapeh Volcano, New Zealand, September 1995, *Geology, 24, 1107-1110.*

Davies, T. (1990), Debris-flow surges-Experimental simulation, *Journal of Hydrology (N.Z.) 29, 1.*

Davies, T. (1982), Spreading of rock avalanche debris by mechanical fluidization, *Rock Mechanics, 15, 9-24.*

Deparis, J., Jongmans, D., Cotton, F., Baillet, L., Thouvenot, F., Hantz, D, (2008), Analysis of rock-fall and rock-fall avalanche seismograms in the French Alps, *BSSA, 98, 1781-1796.*

Doyle, E., Cronin, S., Cole, S., Thouret, J, (2010), The coalescence and organization of lahars at Semeru volcano, Indonesia, *Bull. Volcanol., 72, 961-970.*

Galgaro, A., Tecca, P., Genevios, R., Deganutti, A, (2005), Acoustic module of the Acquabona (Italy) debris flow monitoring system, *Natural Hazards and Earth System Sciences, 5, 211-215.*

Goto, A., Ripepe, M., Lacanna, G, (2014), Wideband acoustic records of explosive volcanic eruptions at Stromboli: New insights on the explosive process and the acoustic source, *Geophys. Res. Lett., 41, 3851-3857.*

Garces, M., Harris, A., Hetzer, C., Johnson, J., Rowland, S., Marchetti, E., Okubo, P, (2003), Infrasonic tremor observed at Kilauea Volcano, Hawai'I, *GRL, 30, 20, 2023.*

Garcés, M., McNutt, S, (1997), Theory of the airborne sound field generated in a resonant magma conduit, *J. Volcanol. Geotherm. Res., 78, 155-178.*

Hadley, K., LaHusen, R. (1995), Technical manual for experimental acoustic flow monitor, *USGS Open-file Report, 95-114.*

Hamling, I, (2017), Crater lake controls on volcano stability: Insights from White Island, New Zeland, *Geophysical Research Letters, 44.*

Harper, J, (1984), Peritz' F-Test: Basic program of robust multiple comparison test for statistical analysis of all differences among group means, *Comput. Biol. Med., 14, 4, 437-445.*

Heap, M., Kennedy, B., Pernin, N., Jacquemard, L., Baud, P., Farquharson, J., Scheu, B., Lavallee, Y., Gilg, A., Brake, M., Mayer, K., Jolly, A., Reuschle, T., Dingwell, D, (2015), Mechanical behavior and failure modes in the Whakaari (White Island Volcano) hydrothermal system, New Zealand, *J. Volcanol. Geotherm. Res., 295, 26-42.*

Hodgson, K., Manville, V, (1999), Sedimentology and flow behavior of a rain-triggered lahar, Mangatoetoenui Stream, Ruapehu Volcano, New Zealand, *GSA Bulletin, 111, 743-754.*

Hobden, B.J. (1997), Modelling magmatic trends in time and space: Eruptive and magmatic history of Tongariro volcanic complex, New Zealand, *Thesis, University of Canterbury, New Zealand.*

Houghton, B., Nairn, I, (1991), The 1976-1982 Strombolian and phreatomagmatic eruptions of White Island, New Zealand: Eruptive and depositional mechanisms at a "wet" volcano, *Bull. Volcanol. 54, 25-49.*

Huang, C., Yin, H., Chen, C., Yeh, C., Wang, C, (2007), Ground vibrations produced by rock motions and debris flows, *Journal of Geophysical Research Letters, 112.*

Ide, S., (2010), Striations, duration, migration and tidal response in deep tremor, *Nature, 466, 356-359.*

Ishii, M. (2011), High-frequency rupture properties of the M_w 9.0 off the Pacific coast of Tohoku Earthquake, *Earth Planets Space, 63, 609-614.*

Ishii, M., Shearer, P., Houston, H., Vidale, J, (2005), Extend, duration and speed of the 2004 Sumatra-Andaman earthquake imaged by the Hi-Net array, *Nature, 435, 16.*

Ishii, M., Shearer, P., Houston, H., Vidale, J, (2007), Teleseismic P-wave imaging of the 26 December 2004 Sumatra-Andaman and 28 March 2005 Sumatra earthquake ruptures using the Hi-Net array, *J. Geophys. Res., 112, B11307.*

Iverson, R., Logan, M., LaHusen, R., Berti, M, (2010), The perfect debris flow? Aggregated results from 28 large-scale experiments, *Journal of Geophysical Research, 115, F03005.*

Johnson, J.B, (2003), Generation and propagation of infrasonic airwaves from volcanic explosions, *J. Volcanol. Geotherm. Res., 121, 1-14.*

Johnson, J.B, (2005), Source location variability and volcanic vent mapping with a small-aperture infrasound array at Stromboli Volcano, Italy, *Bull. Volcanol. 67, 1-14*

Johnson, J., Aster, R. (2005), Relative partitioning of acoustic and seismic energy during Strombolian eruptions, *Journal of Volcanology and Geothermal Research, 148, 334-354. J. Volcanol. Geotherm. Res., 199, 1-24.*

Johnson, J.B., Lees, J., Varley, N, (2011), Characterizing complex eruptive activity at Santiaguito, Guatemala using infrasound semblance in networked arrays,

Johnson, J.B., Lees, J., Yepes, H, (2006), Volcanic eruptions, lightning, and a waterfall: Differentiating the menagerie of infrasound in the Ecuadorian jungle, *Geophysical Research Letters, 33.*

Johnson, J., and Savage, M., (2012), Tracking volcanic and geothermal activity in the Tongariro Volcanic Center, New Zealand, with shear wave splitting tomography, *J. Volcanol. Geotherm. Res., 223-224, 1-10.*

Jolly, A., Thompson, G., Norton, G, (2002), Locating pyroclastic flows on Soufriere Hills Volcano, Montserrat, West Indies, using amplitude signals from high dynamic range instruments, *Journal of Volcanology and Geothermal Research, 118, 299-317.*

Jolly, A., Chardot, L., Neuberg, J., Fournier, N., Scott, B., Sherburn, S. (2012), High impact mass drops from helicopter: A new active seismic source method applied in an active volcanic setting, *Geophysical Research Letters*, *39, L12306; doi: 10.1029/2012GL051880*

Jolly, A., Jousset, P., Lyons, J., Carniel, R., Fournier, N., Fry, B., Miller, C. (2014B), Seismo-acoustic evidence for an avalanche driven phreatic eruption through a beheaded hydrothermal system: An example from the 2012 Tongariro eruption, *Journal of Volcanology and Geothermal Research, 286, 331-347.*

Jolly, G., Keys, H., Procter, J., Deligne, N. (2014A), Overview of the co-ordinated risk-based approach to science and management response and recovery for the 2012

eruptions of Tongariro volcano, New Zealand, *Journal of Volcanology and Geothermal Research, 286, 184-207.*

Jolly, A., Lokmer, I., Kennedy, B., Key, H., Procter, J., Lyons, J., Jolly, G, (2014C), Active seismic sources as a proxy for seismic surface processes: An example from the 2012 Tongariro volcanic eruptions, New Zealand, *Journal of Volcanology and Geothermal Research 286, 317-330.*

Jolly, A., Lokmer, I., Thun, J., Salichon, J., Fry, B., Chardot, L, (2017), Insights into fluid transport mechanisms at White Island from analysis of coupled very long-period (VLP), long-period (LP) and high-frequency (HF) earthquakes, *J. Volcanol. Geotherm. Res., 343, 75-94.*

Jones, K., Johnson, J., Aster, R., Kyle, P., McIntosh, W, (2008), Infrasonic tracking of large bubble bursts and ash venting at Erebus Volcano, Antarctica, *J. Volcanol. Geotherm. Res., 177, 661-672.*

Kanamori, H., (1993), Locating earthquakes with Amplitude: Application to real-time seismology, *Bull. Seis. Soc. Amer*., *83,1,264-268.*

Kao, H., Shan, S, (2004), The Source-Scanning Algorithm: Mapping the distribution of seismic sources in time and space, *Geophys. J. Int. 157, 589-594.*

Kawakatsu, H., Kaneshima, S., Matsubayashi, H., Ohminato, T., Sudo, Y., Tsutsui, T., Uhira, K., Yamasato, H., Ito, H., Legrand, D, (2000), Aso94: Aso seismic observation with broadband instruments, *J. Volcanol. Geotherm. Res., 101, 129-145.*

Kazakov, N., Minervin, I, (2000), Mechanism of wave formation in coherent debris-flows generated by rain, *Debris-Flow Hazards Migration: Mechanics, Prediction, and Assessment, 397-402.*

Keys, H., Green, P, (2008), Ruapehu lahar New Zealand 18 March 2007: Lessons for hazard assessment and risk mitigation 1995-2007, *Journal of Disaster Research, 3.*

Kilgour, J., Kennedy, B., Gates, S, (2018), Phreatic eruption dynamics derived from deposit analysis: A case study from a small, phreatic eruption from Whakaari/White Island, New Zealand, *EPS, In Review.*

Kiser, E., Ishii, M, (2011), The 2010 M_w 8.8 Chile earthquake: Triggering on multiple segment and frequency-dependent rupture behavior, *Geophys. Res. Lett.,38, L07301.*

Kishimura, K., Izumi, K, (1997), Seismic signals induced by snow avalanche flow, *Natural Hazards, 15, 89-100.*

Kogelnig, A., Surinach, E., Vilajosana, I., Hubl, J., Sovilla, B., Hiller, M., Dufour, F, (2011), On the complementariness of infrasound and seismic sensors for monitoring snow avalanches, *Nat. Hazards Earth Syst. Sci., 11, 2355-2370.*

Konno, K., Ohmachi, T, (1998), Ground-motion characteristics estimated from spectral ratio between horizontal and vertical components on micotremor, *BSSA, 88, 228-241.*

Kumagai, H., Lacson, R., Maeda, Y., Figueroa, M., Yamahina, T., (2014), Shallow S wave attenuation and actively degassing magma beneath Taal Volcano, Philippines, *Geophys. Res. Lett., 41, 6681-6688.*

Kumagai, K., Lacson, R., Maeda, Y., Figueroa, M., Yanashina, T., Ruiz, M., Palacios, P., Ortiz, H., Yeps, H., (2013), Source amplitudes of volcano-seismic signals determined by the amplitude source location method as a quantitative measure of event size, *J. Volcanol. Geotherm. Res., 257, 57-71.*

Kumagai, H., Mothes, P., Ruiz, M., Maeda, Y., (2015), An approach to source characterization of tremor signals associated with eruptions and lahars, *Earth, Planets and Space, 67, 178.*

Kumagai, H., Nakano, M., Maeda, T., Yepes, H., Palacios, P., Ruiz, M., Arrais, S., Vaca, M., Molina, I., Yamashima, T, (2010), Broadband seismic monitoring of active volcanoes using deterministic and stochastic approaches, *Journal of Geophysical Research, 115.*

Kumagai, H., Palacios, P., Maeda, T., Castillo, D., Nakano, M, (2009), Seismic tracking of lahars using tremor signals, *J. Volcanol. Geotherm. Res., 183, 112-121.*

Kumagai, H., Palacio, P., Ruiz, M., Yepes, H., Kozono, T., (2011), Ascending seismic source during an explosive eruption at Tungurahua volcano, Ecuador, *Geophys. Res. Lett., 38, L01306.*

Lahr, J., (1989), HYPOELLIPSE/Version 2.0: A computer program for determining local earthquake hypocentral parameters, magnitudes, and first motion pattern. *U.S. Geological Survey, Open-File. 89-116, 92pp.*

Lahr, J., Chouet, B., Stephens, C., Power, J., Page, R., (1994), Earthquake classification, location, and error analysis in a volcanic environment: implications

for the magmatic system of the 1989-1990 eruptions at Redoubt Volcano, Alaska. *Journal of Volcanology and Geothermal Research, 62, 137-151.*

Lavigne, F., Suwa, H, (2004), Contrasts between debris flows, hyperconcentrated flows and stream flows at a channel of Mount Semeru, East Java, Indonesia, *Geomorphology, 61, 41-58.*

Lavigne, F., Thouret, J., Voight, B., Suwa, H., Sumaryono, A, (2000), Lahars at Merapi volcano, Central Java: an overview, *Journal of Volcanology and Geothermal Research, 100, 423-456.*

Lawrence, W., Williams, T, (1976), Seismic signals associated with avalanches, *Journal of Glaciology, 17, 521-526.*

Lecointre, J., Hodgson, K., Neall, V., Cronin, S, (2004), Lahar-triggering mechanisms and hazard at Ruapehu Volcano, New Zealand, *Natural Hazards, 31, 85-109.*

Lee, W. H. K., Bennett, R. E., and Meagher, L. (1972), A method for estimating magnitude of local earthquakes from signal duration, *Open file report, USGS*

Leprettre, B., Navarre, J., Taillefer, A., Danielou, Y., Panel, J., Touvier, P, (1996), Reliable estimation of avalanche activity using seismic methods, *Proceedings of the International Snow Science Workshop in Banff, Alberta, 184-189.*

Lermo, J., Chavez-Garcia, F, (1993), Site effect evaluation using spectral ratios with only one station, *BSSA, 83, 1574-1594.*

Levy, C., Mangeney, A., Bonilla, F., Hilbert, C., Calder, E., Smith, P, (2015), Friction weakening in granular flows deduced from seismic records at the Soufriere Hills Volcano, Montserrat, *J. Geophys. Res. Solid Earth, 120, 7536-7557.*

Lowe, D. (1979), Sediment gravity flows: Their classification and some problems of application to natural flows and deposits, *SEPM Special Publication, 27, 75-82.*

Lube, G., Cronin, S., Manville, V., Procter, J., Cole, S., Freundt, A. (2012), Energy growth in laharic mass flows, *Geology, 40, 475-478.*

Matoza, R., Fee, D., Neilsen, T., Gee, K., Ogden, D, (2013), Aeroacoustics of volcanic jets: Acoustic power estimation and jet velocity dependence, *J. Geophys. Res. 118, 1-16.*

Matoza, R., Hedlin, M., Garces, M, (2007), An infrasound array study of Mount St. Helens, *J. Volcanol. Geotherm. Res., 160, 249-262.*

Mayeda, K., Koyanagi, S., Aki, K, (1991), Site amplification from S-wave coda in the long valley caldera region, California, *BSSA, 81, 2194-2213.*

Mayer, K., Scheu, B., Gilg, A., Heap, M., Kennedy, B., Lavallee, Y., Brake, M., Dingwell, D, (2015), Experimental constraints on phreatic eruption processes at Whakaari (White Island volcano), *J. Volcanol. Geotherm. Res., 302, 150-162.*

McNutt, S., Thompson, G., West, M., Fee, D., Stihler, S., Clark, E, (2013), Local seismic and infrasound observations of the 2009 explosive eruptions of Redoubt Volcano, Alaska, *J. Volcanol. Geotherm. Res.,296, 63-76.*

Nakamura, Y, (1989), A method for dynamic characteristics estimation of subsurface using microtremor on the ground surface, *QR Railway Tech. Res. Inst. 30, 25-33.*

Navratil, O., Liebault, F., Bellot, H., Travaglini, E., Theule, J., Chambon, G., Laigle, D, (2013), High-frequency monitoring of debris-flow propagation along the Real Torrent, Southern French Prealps, *Geomorphology, 201, 157-171.*

Neidel, N., Tarner, M.T., (1971), Semblance and other coherency measure for multichannel data. *Geophys . 36, 483–497.*

Nishi, Y., Sherburn, S., Scott, B., Sugihara, M, (1996), High-frequency earthquakes at White Island Volcano, New Zealand: Insights into the shallow structure of a volcano-hydrothermal system, *J. Volcanol. Geotherm. Res., 72, 183-197.*

Nishimura, T., Nakamichi, H., Tanaka, S., Sato, M., Kobayashi, T., Ueki, S., Hamaguchi, H., Ohtake, M., Sato, H, (2000), Source process of very long period seismic events associated with the 1998 activity of Iwate Volcano, northeastern Japan, *GRL, 105, 19135-19147.*

Norris, R. (1994), Seismicity of rockfalls and avalanches at three Cascade Range volcanoes: Implications for seismic detection of hazardous mass movements, *BSSA, 84, 1925-1939.*

Ogiso, M., Yomogida, K. (2012), Migration of tremor locations before the 2008 eruption of Meakandake Volcano, Hokkaido, Japan, *Journal of Volcanology and Geothermal Research, 217-218, 8-20.*

Ogiso, M., Yomogida, K. (2015), Estimation of locations and migration of debris flows on Izu-Oshima Island, Japan, on 16 October 2013 by the distribution of high frequency seismic amplitudes, *J. Volcanol. Geotherm. Res., 298, 15-26.*

Ogiso, M., Matsubayashi, H., Yamamoto T., (2015), Descent of tremor source locations before the 2014 phreatic eruption of Ontake volcano, Japan Earth, Planets and Space (2015) *67:206 DOI 10.1186/s40623-015-0376-y*

Phillips, S., and Aki, K., (1986), Site amplification of coda wave from local earthquakes in central California, *BSSA, 76(3), 627-648.*

Pierson, T. (1985), Initiation and flow behavior of the 1980 Pine Creek and Muddy River lahars, Mount St. Helens, Washington, *Geological Society of America Bulletin, 96, 1056-1069.*

Pierson, T. (1995), Flow characteristics of large eruption-triggered debris flows at snow-clad volcanoes: Constraints for debris-flow models, *J. Volcanol. Geotherm. Res., 66, 283-294.*

Pierson, T. (2005), Hyperconcentrated flow transition process between water flow and debris flow, *In: Jakob M, Hungr O (eds.) Debris flow hazards and related phenomena, Springer-Verlag, New York, New York, 159-196.*

Pierson, T., and Scott, K. (1985), Downstream dilution of a lahar: Transition from debris flow to hyperconcentrated streamflow, *Water Resources Research, 21, 1511-1524.*

Palacios, P., Diez, M., Kendall, J., Mader, H, (2016), Seismic-acoustic energy partitioning during a parozysmal eruptive phase of Tungurahua volcano, Ecuador, *Geophys. J. Int. 205, 1900-1915.*

Procter, J., Cronin, S., Fuller, I., Lube, G., Manville, V, (2010), Quantifying the geomorphic impacts of a lake-breakout lahar, Mount Ruapehu, New Zealand, *Geology, 38, 67-70.*

Procter, J., Cronin, S., Zernack, A., Lube, G., Stewart, R., Nemeth, K., Keys, H. (2014), Debris flow evolution and the activation of an explosive hydrothermal system; Te Maari, Tongariro, New Zealand, *Journal of Volcanology and Geothermal Research, 286, 303-316.*

Quenouille, M. H., 1949. Approximate tests of correlation in time-series. *J. R. Statist. Soc. B 11: 68-84.*

Ripepe, M., Rossi, M., Saccorotti, G, (1993), Image processing of explosive activity at Stromboli, *Journal of Volcanology and Geothermal Research, 54, 335-351.*

Ripepe, M., Marchetti, E. (2002), Array tracking of infrasonic sources at Stromboli Volcano, *GRL, 29, 22, 2076.*

Rogers, J., Niewander, A. (1988), Thirteen ways to look at the correlation coefficient, *The American Statistician, 42, 59-66.*

Rowell, C., Fee, D., Szuberla, C., Arnoult, K., Matoza, R., Firstov., Kim, Makhmudov, E, (2014), Three-dimensional volcano-acoustic source localization at Karymsky Volcano, Kamchatka, Russia, *J. Volcanol. Geotherm. Res., 283, 101-115.*

Shearer, P.M., (1999), Introduction to Seismology, Cambridge University Press.

Sherburn, S., Scott, B, (1993), B-type volcanic earthquakes at White Island volcano, New Zealand, *Journal of Volcanology and Geothermal Research, 56, 351-355.*

Sherburn, S., Scott, B., Hurst, A, (1991), Volcanic tremor and activity at White Island, New Zealand, July-September 1991, *NZ Journal of Geology and Geophysics, 39, 2:329-332.*

Sherburn, S., Scott, B., Nishi, Y., Sugihara, M, (1998), Seismicity at White Island volcano, New Zealand: A revised classification and inferences about source mechanism, *J. Volcanol. Geotherm. Res., 83, 387-312.*

Smith, G. (1986), Coarse-grained nonmarine volcaniclastic sediment: Terminology and depositional process, *Geological Society of America Bulletin, 97, 1-10.*

Spudich, P., Hellweg, M., Lee, W, (1996), Directional topographic site response at Tarzana observed in aftershocks of the 1994 Northridge, California, earthquake: Implications for mainshock motions, *BSSA, 86, S193-S208.*

Surinach, E., Sabot, F., Furdada, G., Vilaplana, J, (2000), Study of seismic signals of artificially released snow avalanche for monitoring purposes, *Phys. Chem. Earth (B), 25, 721-727.*

Surinach, E., Vilajosana, I., Khazaradze, G., Biescas, B., Furdada, G., Vilaplana, J, (2005), Seismic detection and characterization of landslides and other mass movements, *Natural Hazards and Earth System Sciences, 5, 791-798.*

Suwa, H., Akamatsu, J., Nagai, Y, (2003), Energy radiation by elastic waves from debris flows, *Debris-Flow Hazards Migration: Mechanics, Prediction, and Assessment, 895-904.*

Suwa, H., Yamakoshi, T., Sato, K, (2000), Relationship between debris-flow discharge and ground vibration, *Debris-Flow Hazards Migration: Mechanics, Prediction, and Assessment, 311-318.*

Taddeucci, J., Alatorre, M., Moroni, M., Tornetta, L., Capponi, A., Scarlato, P., Dingwell, D., De Rita, D, (2012), *GRL, 39, L16306.*

Takemura, S., Furumura, T., Saito, T., (2009), Distortion of the apparent S-wave radiation pattern in the high-frequency wavefield: Tottori-Ken Seibu, Japan, earthquake of 2000, *Geophysical Journal International, 178, 950-961.*

Taisne, B., Brenguier, F., Shapiro, N., Ferrazzini, V., (2011), Imaging the dynamics of magma propagation using radiated seismic intensity, *Geophys. Res. Lett., 38, L04304.*

Taner, M., Koehler, F, (1969), Velocity spectra –digital computer derivation and applications of velocity functions, *Geophysics, 34, 859-881.*

Titzschkau, T., Savage, M., Hurst, T., (2010), Changes in attenuation related to eruptions of Mt. Ruapehu Volcano, New Zealand, *J. Volcanol. Geotherm. Res., 190, 168-178.*

Topping, W.W., (1974), Some aspects of quaternary history of Tongariro volcanic center, *Thesis, Victoria University of Wellington, New Zealand.*

Tsuruga, K., Yomogida, K., Honda, S., Ito, H., Ohminato, T., Kawakatsu, H, (1997), Spatial and temporal variations of volcanic earthquakes at Sakurajima Volcano, Japan, *J. Volcanol. Geotherm. Res., 75, 337-358.*

Tukey, J. W., 1958. Bias and confidence in not-quite large samples (Abstract). *Ann. Math. Statist. , 29, 614.*

Tungol, N., Regalado, T. (1996), Rainfall, acoustic flow monitor records, and observed lahars of the Sacobia River in 1992, Newhall, C., & Punongbayan, R. (eds.) *Fire and Mud: Eruptions and lahars of Mount Pinatubo, Philippines, Seattle, University of Washington.*

Uhira, K., Yamasato, H., Takeo, M, (1994), Source mechanism of seismic waves excited by pyroclastic flows observed at Unzen Volcano, Japan, *J. Geophys. Res., 99, 17757-17773.*

Van Bemmelen, R. (1949), Report on the volcanic activity and volcanological research in Indonesia during the period 1936-1948, *Bulletin Volcanologique, 9, 3-19.*

Vazquez, R., Capra, L., Caballero, L., Arambula-Mendoza, R., Reyes-Davila, G, (2013), The anatomy of a lahar: Deciphering the 15th September 2012 lahar at Volcan de Colima, Mexico, *Journal of Volcanology and Geothermal Research, 272, 126-136.*

Vazquez, R., Surinach, E., Capra, L., Arambula-Mendoza, R., Reyes-Davila, G. (2016), Seismic characterization of lahars at Volcan de Colima, Mexico, *Bull Volcanol, 78.*

Vergniolle, S., Brandeis, G, (1994), Origin of the sound generated by Strombolian explosions, *Geophysical Research Letters, 21, 1959-1962.*

Vilajosana, I., Surinach, E., Abellan, A., Khazaradze, G., Garcia, D., Llosa, J, (2008), Rockfall induced seismic signals: case study in Montserrat, Catalonia, *Natural Hazards Earth Systems Science, 8, 805-812.*

Waldhauser, F, and Ellsworth, W, (2000), A Double-difference earthquake location algorithm: Method and application to the Northern Hayward Fault, California, *BSSA, 90(6), 1353-1368.*

Walker, K., Ishii, M., Shearer, P, (2005), Rupture detatils of the 28 March 2005 Sumatra M_w 8.6 earthquake imaged with teleseismic P-waves, *Geophys. Res. Lett.,32, L24303.*

Walsh, B., Jolly, A., Procter, J., (2016), Seismic analysis of the 13 October 2012 Te Maari, New Zealand, lake breakout lahar: Insights into flow dynamics and the implications on mass flow monitoring, *J. Volcanol. Geotherm. Res., 324, 144-155.*

Walsh, B., Jolly, A., Procter, J, (2017), Calibrating the amplitude source location (ASL) method by using active seismic sources: An example from Te Maari volcano, Tongariro National Park, New Zealand, *Geophys. Res. Lett., 44: doi:10.1002/2017GL073000.*

Walter, F., Burtin, A., McArdell, B., Hovius, N., Weder, B., Turowski, J, (2017), Testing seismic amplitude source location for fast debris-flow detection at Illgraben, Switzerland, *Nat. Hazards Earth Syst. Sci., 17, 939-955.*

Werner, C., Hurst, T., Scott, B., Sherburn, S., Christenson, B., Britten, K., Baker, J., Mullan, B, (2008), Variability of passive gas emissions, seismicity, and deformation during crater lake growth at White Island Volcano, New Zealand 2002-2006, *J. Geophys. Res., 113, B01204.*

Willmott, C. (1981), On the validation of models, Physical *Geography, 2, 184-194.*

Woulff, G., McGetchin, T, (1976), Acoustic noise from volcanoes: Theory and experiment, *Geophys. J.R. astr. Soc. 45, 601-616.*

Yamada, M., Kumagai, H., Matsushi, Y., Matsuzawa, T. (2013), Dynamic landslide processes revealed by broadband seismic records, *Geophysical Research Letters 40, 2998-3002*

Yamasato, H. (1997), Quantitative analysis of pyroclastic flows using infrasonic and seismic data at Unzen Volcano, Japan, *Journal of Physics of the Earth, 45, 397-416.*

Yamasato, H. (1998), Nature of infrasonic pulse accompanying low frequency earthquake at Unzen Volcano, Japan, *Bull. Volcanol. Soc. Japan, 43, 1-13.*

Zobin, V., Plascencia, I., Reyes, G., Navarro, C, (2009), The characteristics of seismic signals produced by lahars and pyroclastic flows: Volacan de Colima, Mexico, *Journal of Volcanology and Geothermal Research, 179, 157-167.*

VITA AUCTORIS

Braden Walsh was born on a beautiful sunny summer June day in the year 1989 in Minot, North Dakota, USA to Mike and Gail Walsh. While growing up in North Dakota, Mr. Walsh lived a simple prairie life of outdoor activities, getting picked on by older siblings, and schoolwork. Mr. Walsh's education in North Dakota consisted of Lincoln Elementary School, Ramstad Middle School, and Minot High School; the first two of which do not exist anymore, and also received perfect attendance at. In 2007 Braden Walsh graduated from Minot High School, and then proceeded to study his undergraduate education in geology at Oregon State University. In 2008 Mr. Walsh transferred to the University of Nevada, Reno where he graduated with his Bachelors of Science in Geophysics in the spring of 2011. In the fall of 2011 Mr. Walsh continued his education at Saint Louis University in St. Louis Missouri to pursue a Masters degree. At Saint Louis University, Mr. Walsh became Master Walsh by obtaining his Masters of Science Research in Geophysics/Seismology in the spring of 2013. After some time of contemplating, Master Walsh traveled to Middle Earth in early 2014 to conquer a PhD in Volcanology, where he will hopefully soon evolve into Mr. Master Dr. Walsh.



Photograph from Braden's fieldwork campaign during his PhD in Colima, Mexico.